Doctoral Thesis

Exploring exciton recombination, migration, and transfer in halide perovskite systems

（ハロゲン化物ペロブスカイト系における励起子の再結合、移動、および転移の探求）

Graduate School of Environmental Science
Hokkaido University

Most Farida Khatun

March 2025

Acknowledgment

I am grateful to Almighty Allah for granting me the wisdom, strength, and perseverance to complete my doctoral thesis.

I would like to express my deepest gratitude to my supervisor, Professor Vasudevan Pillai Biju, for his guidance, support, and encouragement throughout my Ph.D. journey. I am thankful to Associate Professor Yuta Takano for his support during my research. I am deeply grateful to Assistant Professor Takuya Okamoto for his guidance and support in understanding the fundamentals of laboratory work and perovskite research. To my labmates, thank you for fostering such a collaborative and inspiring environment. I am also grateful to Ms. Atsuko Fujii for her support in administrative matters.

I am deeply grateful to my parents for their unconditional love and support throughout my life. My heartfelt appreciation also goes to my beloved husband and children for their unwavering support and sacrifices during my doctoral journey.

I acknowledge the Hokkaido University EXEX doctoral fellowship for funding this research. I also thank the Hokkaido University Nanotechnology PLATFORM and the Dynamic Alliance for Open Innovation Bridging Human, Environment, and Materials. Thanks to Professor Akihiro Furube and Professor Tetsuro Katayama for the transient absorption measurements. Finally, I am grateful to everyone who has contributed, directly or indirectly, to this research and my personal growth. Thank you.

Abstract

Lead halide perovskites have emerged as promising semiconductors for a broad spectrum of applications, such as solar cells, lasers, light-emitting diodes, and photodetectors. Their prominence stems from their outstanding characteristics, including facile synthesis, strong light absorption capabilities, tunable bandgaps, and exceptional charge carrier mobility. Bulk perovskite has a high carrier diffusion length, making it promising for optoelectronic applications. However, it is difficult to fabricate into a thin film which is necessary for increasing device performance. In contrast, a perovskite nanocrystal (PNC) film can be easily fabricated with a desired thickness. However, these PNCs often face instability due to defects, low carrier diffusion due to high quantum confinement, and reduced carrier extraction at the interface, hindering their overall efficiency. The basic aim of this thesis is to improve the stability of PNCs through defect passivation, enhance carrier diffusion via assembly formation, and increase carrier extraction into the transport layers using multiwall carbon nanotubes (MWCNTs) as acceptors. The thesis is structured into five chapters. Chapter 1 provides an introduction to perovskites, focusing on their structures, photoluminescence (PL) behavior, and carrier diffusion dynamics across different perovskite sample types. Special emphasis is placed on the use of PNC films with an optimal thickness to maximize carrier diffusion. This chapter also explores various carrier extraction strategies and potential applications of perovskites. Chapter 2 details the synthesis methodologies for PNCs and perovskite quantum dots (PQDs) using the hot-injection method. The functionalization process of MWCNTs is also detailed here. It also includes microscopic and spectroscopic tools, such as steady-state absorption spectroscopy, steady-state fluorescence spectroscopy, time-resolved single-photon counting, transient absorption spectroscopy, Raman spectroscopy, X-ray photoelectron spectroscopy, Fourier-transform infrared spectroscopy, scanning transmission electron microscopy, and single-particle microscopy. Chapter 3 focuses on the defect passivation of $CsPbBr_3$ PNCs, which is mainly responsible for the nonradiative recombination and instability. STEM-EDX analysis of $CsPbBr_3$ PNCs synthesized using the hot injection method reveals the presence of Br^- vacancies, leading to a low PL quantum yield (QY) and a short PL lifetime. The PNCs were post-treated with various inorganic halide sources including CsBr, NaBr, and KBr. PLQY, PL lifetime, and intensity trajectories after

vacancy filling were measured. Among various halide salts I tested for defect passivation, NaBr was identified as the most effective, increasing the PLQY from 58% to 98%. The PL lifetime also increases from 11.6 ns to 13.8 ns. Single-particle blinking studies show that suppressed blinking supports the vacancy filling in $CsPbBr_3$ PNCs. Defect passivation significantly reduces nonradiative recombination, improving the photophysical properties of the PNCs. For a longer carrier diffusion length, assembly formation of low dimensional perovskite is necessary. In Chapter 4, I demonstrated the polymer-induced assembly formation of $FAPbBr_3$ PQDs. The solvent evaporation and polybutadiene polymer shrinkage during drying help to assemble the PQDs within a polymer, resulting in a redshifted PL spectral maximum and a longer PL lifetime. This can be attributed to the wave function overlap of the PQDs and miniband formation. Temperature-controlled carrier diffusion was also demonstrated in this chapter. An increase in the temperature of the assembly resulted in a PL spectral blueshift and lifetime decrease, both indicating thermal dissociation of the assembly. Cooling the assembly to room temperature partially restored the optoelectronic properties. These findings underscore the potential of such assemblies for use in optoelectronic devices responsive to external stimuli. Although increased carrier diffusion helps the carrier to reach the charge transport layer, interfacial electronic coupling, and carrier transportation to the electron and hole transport layers are critical for accomplishing efficient carrier extraction. In Chapter 5, I focus on the rapid extraction of charge carriers from $CsPbBr_3$ PNCs using MWCNTs as the electron acceptor layer. The MWCNTs were first functionalized with terminal phenylamine groups to facilitate binding with the PNCs. PNC-MWCNT interface samples were prepared using both post-mixing and in situ hot-injection methods. The resulting PNC-MWCNT conjugates exhibit hot-carrier transfer from the PNCs to the MWCNTs, a reduction in biexciton-mediated nonradiative Auger recombination, and reduced radiative recombination at the band edge. Overall, this thesis outlines methods to enhance PNC quality through halide vacancy filling, enhance the diffusion or transportation of photogenerated charge carriers through assemblies, and extract the carriers across PNC-MWCNT interfaces by hot-electron transfer. These improvements are beneficial for developing more efficient and durable optoelectronic devices.

Abbreviations and Symbols

1-HDC	1-hexadecene
2D	2-dimensional
3D	3-dimensional
A	Absorbance
a	Amplitude
AR	Auger recombination
ASE	Amplified spontaneous emission
c	Concentration
CBM	Conduction band minimum
CCD	Charge-coupled device
CdSe	Cadmium selenide
CsBr	Cesium bromide
CW	Continuous wave
d	Distance between crystal plane
DMF	Dimethylformamide
DMSO	Dimethyl sulfoxide
e	Electron
E_b	Exciton binding energy
EDX	Energy-dispersive X-ray spectroscopy
EMCCD	Electron multiplying charge-coupled device
ETL	Electron transport layer
Eg	Bandgap
eV	Electron volt
FABr	Formamidinium bromide
fs	Femtosecond
FTIR	Fourier transform infrared spectroscopy
GB	Grain boundaries
GBL	Gamma-butyrolactone
GSB	Ground state bleach

h	Hole
HBr	Hydrogen bromide
HC	Hot carrier
HCl	Hydrochloric acid
HTL	Hole transport layer
K	Kelvin
k_1	Monomolecular recombination rate constant
k_2	Bimolecular recombination rate constant
k_3	Auger recombination rate constant
k_B	Boltzmann constant
k_r	Radiative recombination rate constant
k_{nr}	Non-radiative recombination rate constant
l	Optical path
L_D	Charge carrier diffusion length
LARP	Ligand-assisted reprecipitation
LED	Light emitting diode
M	Mirror
MEG	Multiple exciton generation
mg	Milligram
MHP	Metal halide perovskite
MHz	Megahertz
min	Minute
mL	Milliliter
mm	Millimeter
mmol	Millimole
MWCNT	Multiwall carbon nanotube
$NaBH_4$	Sodium borohydride
NaBr	Sodium bromide
NBDTFB	4-Nitrobenzediazonium tetrafluoroborate
ND	Neutral density
NIR	Near infra-red

nm	Nanometer
OA	Oleic acid
OAm	Oleylamine
OPA	Optical parameter amplifier
$PbBr_2$	Lead bromide
PBD	Polybutadiene
PCE	Power conversion efficiency
PeLEDs	perovskite-based LEDs
PIA	Photoinduced absorption
PL	Photoluminescence
PLQE	Photoluminescence quantum efficiency
PLQY	Photoluminescence quantum yield
PNC	Perovskite nanocrystal
PQD	Perovskite quantum dot
ps	Picosecond
PSC	Perovskite solar cell
r	Particle radius
r_A	A-site cation's ionic radius
r_B	B-site cation's ionic radius
r_X	X-site anion's ionic radius
RP	Ruddlesden-Popper
rpm	Rotation per minute
SAXS	Small-angle X-ray scattering
SCLC	Space-charge-limited current model
SE	Stimulated emission
SHG	Second harmonic generation
SOC	Spin-orbit coupling
STEM	Scanning transmission electron microscopy
T	Temperature
TA	Transient absorption
TCSPC	Time-correlated single photon counting

Tg	Glass transition temperature
THF	Tetrahydrofuran
TRPL	Time-resolved photoluminescence
UV	Ultraviolet
UV-vis	Ultraviolet-visible
V	Voltage
VBM	Valance band maximum
v/v	Volume/volume
XPS	X-ray photoelectron spectroscopy
XRD	X-ray diffraction
λ	Wavelength
μL	Microliter
μm	Micrometer
ε	Molar absorptivity
τ	Photoluminescence lifetime
φ	Work function
m*	Reduced mass
$\hbar$	Planck constant
$\in_0$	Vacuum permittivity
μ	Charge carrier mobility
q	Elementary charge
°C	Degree Celsius

Table of Contents

Chapter 1

Introduction

Abstract

Lead halide perovskites (LHPs) have gained immense popularity in optoelectronic and energy applications. HP solar cells have reached efficiencies comparable to silicon photovoltaic devices within a decade. These materials have attractive, tunable optical and electronic properties. Here, I discuss the historical evolution and structural features of LHPs with a focus on their use in photovoltaics. The characteristic ABX_3 crystal structure of HPs allows for the incorporation of a diverse array of chemical species, imparting a high degree of structural and compositional versatility. This chapter also focuses on the structural parameters governing their stability, including the Goldschmidt tolerance factor and octahedral factor. Additionally, the electronic band structure of HPs, shaped by the $[BX_6]^{4-}$ octahedral units and spin-orbit coupling effects, are discussed to highlight their defect tolerance. However, challenges such as structural instability, defect formation, and toxicity impede their commercialization. I also discuss how defects insert shallow and deep traps inside the band structure, making carriers recombine non-radiatively. In the next section, I discuss the photoluminescence (PL) and exciton dynamics of the different types of LHP samples including polycrystalline films, single crystals, and nanocrystals (PNCs). I explain how grain defects in polycrystalline film hinder carrier diffusion while superior diffusion properties are observed in single crystals. For PNCs, insulating ligands and solvents confine the carriers. Long exciton diffusion is necessary for efficient carrier extraction. I also discuss different strategies to enhance the extraction of carriers, which are key parameters for interfacial electron transfer and optimized solar-to-current conversion efficiencies of LHP solar cells (PSCs).

1.1 General introduction

1.1.1 History of halide perovskites

Perovskite was first identified in 1839 by German mineralogist Gustav Rose in the Ural Mountains of Russia, as $CaTiO_3$ (calcium titanate), a naturally occurring mineral.[1, 2] He named it "perovskite" to the honor of Russian mineralogist Lev Perovski. This mineral contains a unique crystal arrangement, now termed as the “perovskite structure”. In the mid-20th century, researchers began synthesizing perovskite-like structures, extending the formula beyond $CaTiO_3$.[3-5] The perovskite structure, which includes diverse cations and anions, allows the replacement of calcium and titanium with various elements, yielding materials with unique properties. Today, the term “perovskite” refers to different compounds depending on the scientific field. For example, in ferroelectric research, common perovskites include barium titanate ($BaTiO_3$)[6] and lead zirconate titanate ($Pb(Zr,Ti)O_3$)[7]. High-temperature superconductor copper oxide perovskites such as $YBa_2Cu_3O_7$,[8] are particularly notable in superconductivity research. Spintronics utilizes perovskites like $(La,Sr)MnO_3$,[9] while geoscientists recognize perovskite as $(Mg,Fe)SiO_3$,[10] which is a major component of earth’s lower mantle and likely its most abundant mineral.

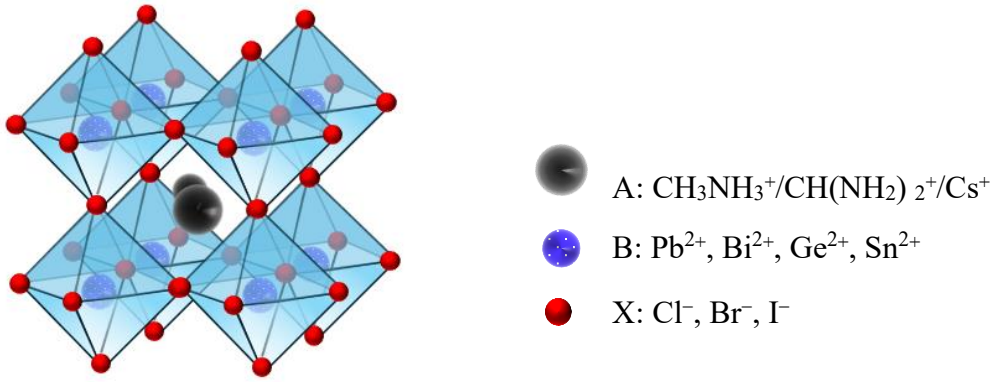

Figure 1.1. A typical crystal structure of LHPs.

Recently, HPs have become highly popular in energy research because of their simple synthesis and exceptional photon-to-current or power conversion efficiency (PCE). HPs have high absorption coefficients, long-range diffusion of charge-carriers, low exciton binding energy, board absorption spectrum, tunable bandgap, and high defect tolerance capability. These exceptional optoelectronic and photophysical properties make

them highly valuable for the use in solar cells, photodetectors, LEDs, and lasers. It was first synthesized in the late 19th century by H. L. Wells.[11] Møller synthesized and studied all inorganic LHP cesium lead halides ($CsPbX_3$) and documented their crystal structure and photoconductive properties in 1958.[12] On the other hand, Weber first synthesized organic-inorganic LHPs in 1978.[13] The groundbreaking moment came in 2009, when Miyasaka and colleagues successfully incorporated these hybrid HPs into solar cells. They achieved an efficiency of 3.8% using $CH_3NH_3PbI_3$ as the light-absorbing material.[14] Since then, PSCs have gained dramatic increase in efficiency, making HPs one of the most studied materials in modern materials science. Over time, the PCE reached 26.54%[15] making them competitive with the conventional silicon cells with PCE of 26.81%[16].

1.1.2 Crystal structures

HPs typically have a crystalline structure based on the general formula ABX_3. A is a large cation, often organic (methylammonium $CH_3NH_3^+$ or formamidinium $CH(NH_2)_2^+$) or inorganic (Cs^+). B is a divalent metal cation, commonly Pb^{2+}, Sn^{2+}, or Ge^{2+}. X denotes a

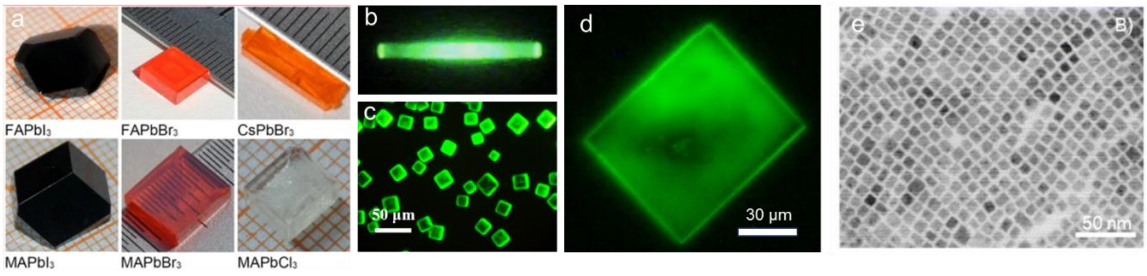

Figure 1.2. Different sizes and shapes of HPs. (a) Photograph of large single crystals,[17] (b-d) fluorescence image of microrod,[18] (c) cubes,[19] and (d) microplate, and (e) a transmission electron microscope image of PNCs[20].

halide anion, such as Cl^-, Br^-, or I^-. The structure is similar to oxide perovskites but incorporates halide ions instead of oxygen, affecting their stability, optoelectronic properties, and bandgap tunability. In the ideal LHP structure, one B-site metal cation is coordinated with six X-site anions to form a BX_6 octahedral geometry. Such octahedra connect by sharing their corners, meaning each X anion is positioned at the corners of the unit cell and shared among adjacent octahedra (Figure 1.1).

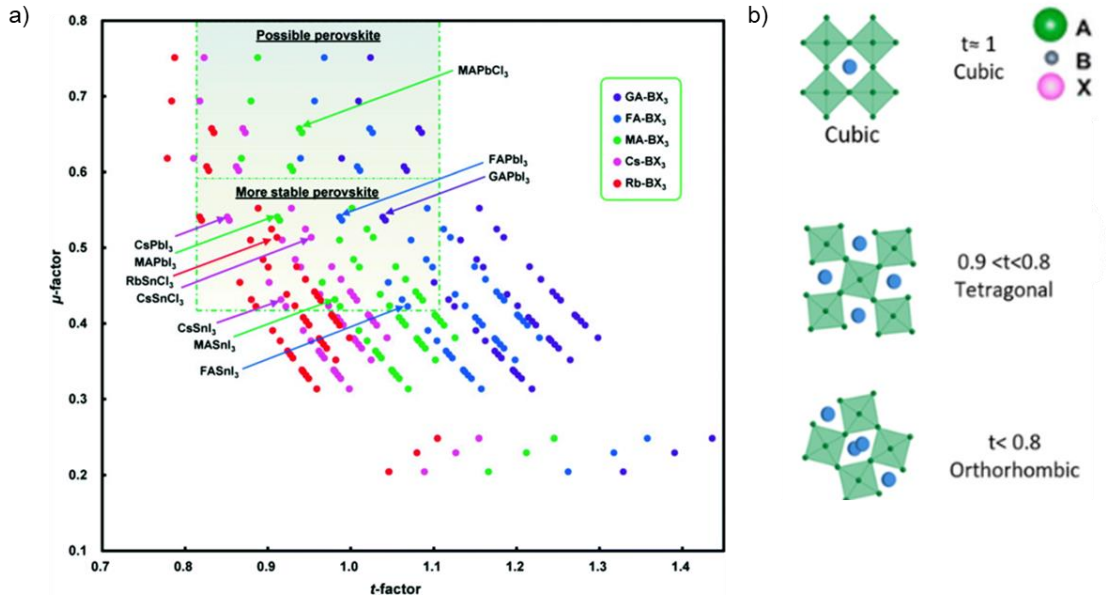

Figure 1.3. (a) A graph illustrating the possible HP structure based on the ABX_3 structure considering the Goldschmidt tolerance factor and octahedral factor. Reproduced from Sarangi, *et al*.[21] (b) Tolerance factors along with lattice distortion.[22]

HPs are highly versatile and can be easily synthesized into various sizes and shapes (Figure 1.2) with relative ease due to their unique crystallization behavior and solution-based synthesis processes. Goldschmidt tolerance factor (t) and octahedral factor (μ) have been used to assess the stability of HP structures (Figure 1.3a). It can predict whether a given set of cations and anions will form a stable 3D crystal structure. The following formula defines the Goldschmidt tolerance factor t:

$$t = \frac{r_A + r_x}{\sqrt{2}(r_B + r_x)}$$

In the above equation, r_A , r_B, and r_x are the ionic radius of the A-site cation, B-site cation, and X-site anion, respectively. The value of t ranges from 0.8 to 1.0 typically suggesting a stable 3D HP structure. A value close to 1 indicates an ideal cubic HP structure. When the value of t is less than 1, it suggests distorted structures including tetragonal or orthorhombic, due to tilting of the BX_6 octahedra (Figure 1.3b). The octahedral Factor μ is defined as follows.

$$\mu = \frac{r_B}{r_X}$$

Here r_B and r_x are the ionic radius of the B-site and halide ions, the parameters defining the stability of the BX_6 octahedral network. μ is between 0.4 and 0.9, which is standard for a stable structure.

LHPs have achieved the highest PCE compared to other B-site cations, making them the benchmark. However, LHPs have less stability and high toxicity. Tin perovskites are the most promising lead-free alternative, reaching PCE up to 12%.[23] However, they are very much prone to oxidation, which can quickly degrade their performance. Other elements like bismuth and antimony are more stable but show poor PCEs. Some B-site cations such as Ruthenium and Rhodium are not discussed here because of their rare and expensive nature.

1.1.3 Electronic structure

The remarkable optical and charge carrier characteristics of LHPs arise from their distinctive energy state distribution at the band edge. Therefore, understanding the band structure of LHPs is necessary. LHPs are considered direct bandgap semiconductors.[24] The conduction band minima (CBM) and valance band maxima (VBM) are typically positioned at the same momentum (k-point), facilitating fast and efficient transitions of charge carriers directly without requiring phonon involvement. DFT calculation revealed that the electronic structure of HPs near the band edges is formed by the interactions within the $[BX_6]^{4-}$ octahedral building blocks.[25-28] The band structure of the LHP is presented in Figure 1.4a. The CB is primarily formed through the hybridization of Pb 6p orbitals and the s and p orbitals of the halide anions. The VB is formed by hybridizing the Pb 6s and 6p orbitals and the s and p orbitals of the halide anion. Therefore, by changing the composition, band gap tuning is possible.

For example, Iodine atoms are larger than bromine atoms, with more diffuse 5p orbitals compared to the 4p orbitals of bromine. This larger and more diffuse electron cloud of iodine allows for greater overlap with the Pb orbitals in the $[PbX_6]^{4-}$ octahedral structure. This stronger overlap reduces the energy difference between the CB and VB, thus narrowing the bandgap in iodide-based perovskites.

Lead and tin atoms have high atomic numbers and are heavy elements that contain an inherent tendency of stronger spin-orbit coupling (SOC). The strength of SOC is

approximately the fourth power of the atomic number (Z^4). Moreover, many HPs exhibit non-centrosymmetric crystal structures. This asymmetry enhances SOC effects

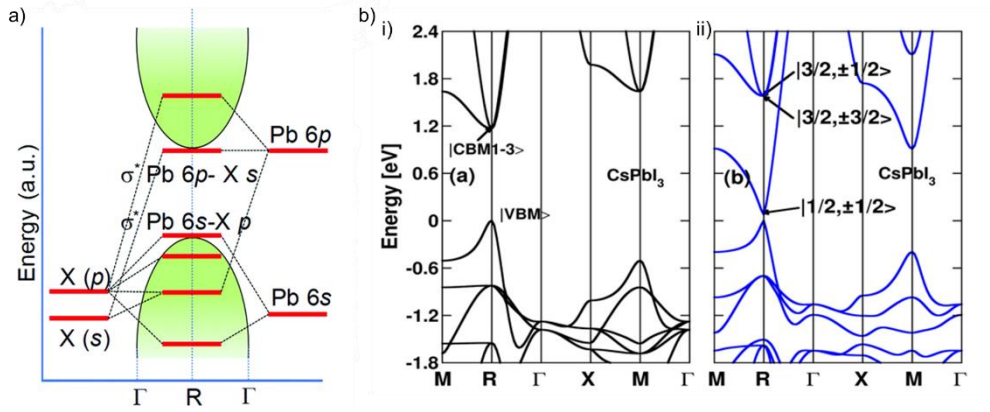

Figure 1.4. a) A typical band structure of LHP without considering spin-orbital coupling.[29] b) Electronic band structure of cubic $CsPbI_3$ (i) without and (ii) with considering SOC corrections.[30]

through mechanisms like the Rashba effect[31] and Dresselhaus splitting.[32, 33] With SOC, VBM, and CBM no longer aligned at the same momentum in k-space. Instead, they shift to different positions in momentum space, which creates an indirect bandgap, where the transition of an electron from the CBM to the VBM needs a change in momentum. SOC in LHP arises from combining two distinct types of electron angular momentum: (i) the electron's orbital angular momentum, and (ii) the electron spin angular momentum. The latter is the clockwise or counterclockwise rotation of an electron around its axis, with a spin quantum number of $m_s = \pm\frac{1}{2}$.[34] This interaction leads to partial constructive or destructive alignment between the orbital and spin angular momentum,[35] which affects the overall energy levels of the system. The notable effect of SOC in LHPs is the splitting and loss of degeneracy in the states close to CBM, which results in the narrowing of the band gap. Figure 1.4b compares the electronic band structure of cubic $CsPbI_3$ without SOC (left, i) and with SOC (right, ii), illustrating these changes.[30] Moreover, some literature shows that the organic-inorganic HPs have some inherent indirect bandgap nature.[36] Carlo Motta *et al.* reported the band gap of the $CH_3NH_3PbI_3$ is affected by the orientation of the CH_3NH_3 molecule along a (011)-like direction. This orientation induces a distortion in the PbI_6 octahedral cage, which makes the bandgap indirect.[37]

1.1.4. Structural and electronic defects

Defects are naturally present in almost all semiconductors at room temperature.[38-40] These exist as atomic-scale defects (such as vacancies) to large-scale forms such as voids or wrinkles. [38, 41-43] These imperfections are responsible for altering semiconductors' optical, electronic, and structural characteristics. Materials science mainly focuses on synthesizing highly pure, crystalline semiconductors with controlled doping to achieve desired optoelectronic properties. However, even a trace number of defects can

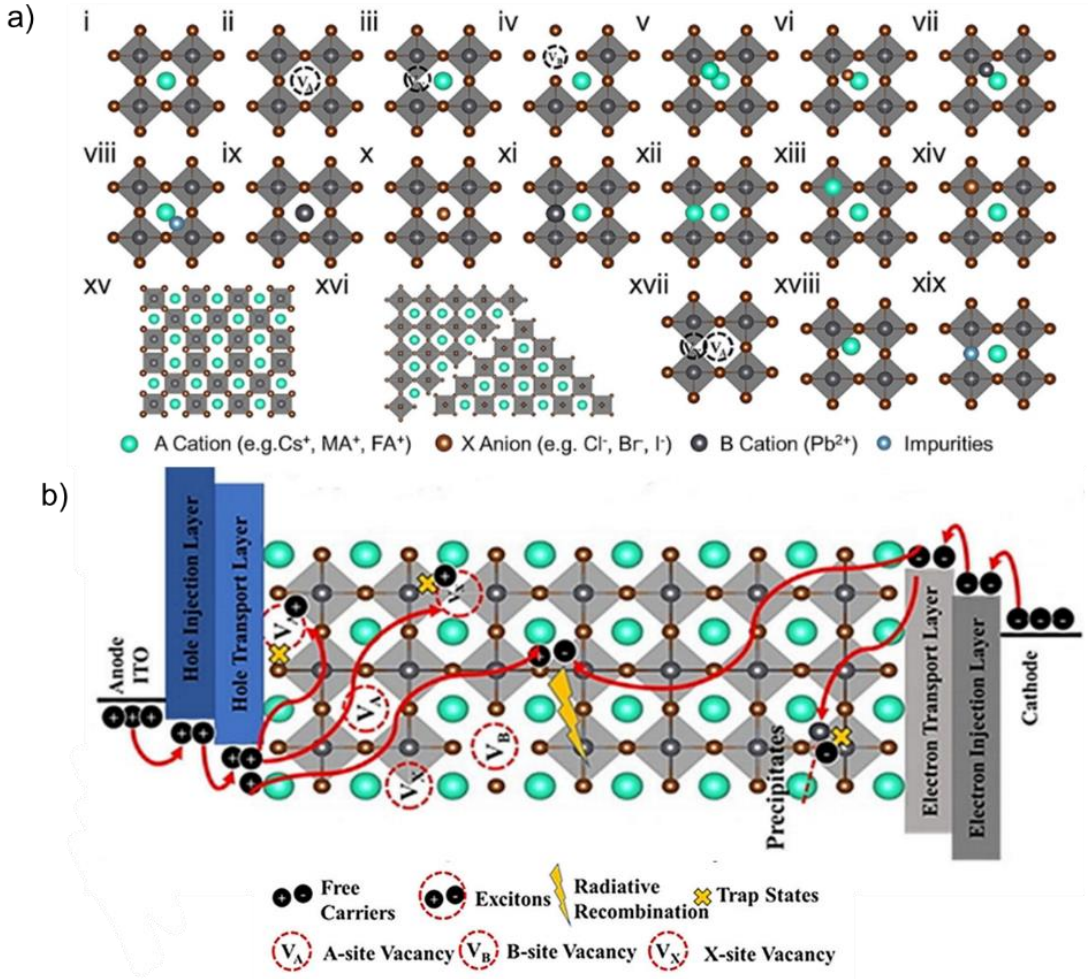

Figure 1.5. (a) Various defects present in LHP, i-xix) Ideal crystals, A-site vacancy, X-site vacancy, B-site vacancy, A-site interstitial, X-site interstitial, B-site interstitial, impurity interstitial, A_B anti-sites, A_X anti-sites, X_B anti-sites, X_A anti-sites, B_A anti-sites, B_x anti-sites, structural dislocations, grain interface defects, Schottky defect, Frenkel defect, and impurity doping, respectively.[44] (b) The injected carriers are captured by the defect in the perovskite LED which decreases the radiative recombination.[44]

significantly impact properties like conductivity, charge-carrier diffusion, and lifetimes, ultimately affecting the performance of devices. HPs gained popularity because of their low-cost synthesis, high PLQY, and tunable optoelectronic properties. However, because of the presence of defects, their commercialization is hindered.[45] Its unique ABX_3 crystal lattice has a repeating structural pattern. Any imperfections within this orderly framework act as defects. Uneven nucleation, incomplete crystallization, stress, and strain during HP crystal growth can increase the defect density. Various types of HP defects are illustrated in Figure 1.5a. In HP, defects are generally divided into two main types:

1. Point defects: Occur on the atomic scale.
2. Structural defects: Extended imperfections within the lattice.

Point defects involve a disruption at a specific location in the crystal lattice, affecting a single or a few atoms. It includes vacancies (missing atoms), interstitials (extra atoms positioned between regular lattice sites), and antisite defects (atoms located on incorrect lattice sites). It can function as a site that captures charge carriers (electrons and holes), leading to unwanted recombination (Figure 1.5b). Vacancies are responsible for ion migration inside the perovskite lattice making it unstable. On the other hand, structural defects are more extensive disruptions in the arrangement of atoms or molecules that affect larger regions. It includes dislocations, grain boundaries, cracks, and voids. They can create barriers to charge carrier movement and adversely affect electronic, mechanical, and optical properties. Moreover, structural defects are also responsible for mechanical weakness, and degradation of LHPs when exposed to the environment. Beyond these intrinsic imperfections, extrinsic impurities can also exist in HPs. Therefore, defect passivation is necessary to enhance the quality of HPs.

As I have discussed in the previous section the geometry of the $[BX_6]^{4-}$ octahedra is crucial in shaping the band structure, any distortions of this octahedral framework can further tune the material's electronic properties. External effects like heat, pressure or moisture can bring change to the octahedral lattice as well as in the electronic structure. Defects present in the LHP crystal can change the lattice bonding and orbital configuration. This induced localized electronic states (Figure 1.6) are different from the carrier transport bands. Photogenerated carriers energetically fall into these states and get

captured. This phenomenon adversely affects the efficiency of the device. A defect is considered shallow if its ground state energy level is close enough to the VB or CB edges, with a separation comparable to or lower than the thermal excitation energy, k_BT (k_B represents the Boltzmann constant, and T is the temperature). In contrast, deep defects have energy levels significantly far from the VB or CB edges (Figure 1.6b), positioned towards the mid-gap, with an energy difference $E \gg k_BT$.[43] HPs are theoretically said to be defect-tolerant compared to conventional semiconductors because of the lack of bonding-antibonding interaction.[46] However, several articles showed the mid-band gap traps in HPs which adversely affect the stability and efficiency of devices. For instance, Liu *et al*. showed that cation vacancies such as V_{Pb} and V_{Sn} produce defect states near the VB, affecting the carrier recombination processes but typically not shifting the overall bandgap.

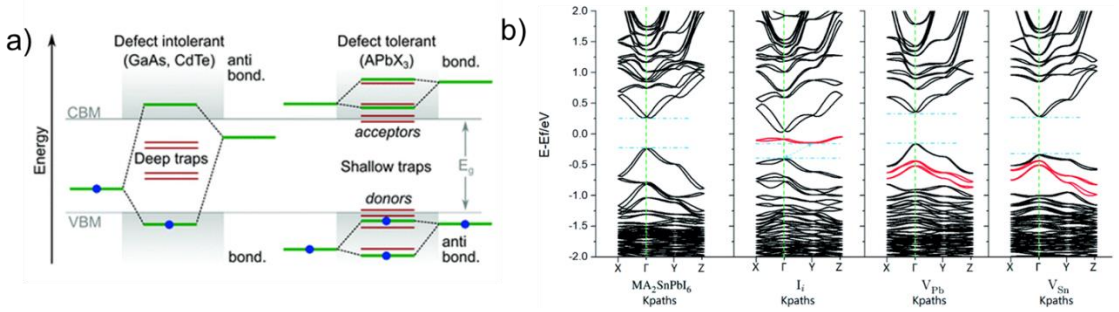

Figure 1.6. (a) A comparison of typical trap energy levels in relation to the electronic band structures of conventional semiconductors and LHPs[47] (b) Band structure of MA_2SnPbI_6 without and with intrinsic defects calculated by PBE + SOC. Red bands are because of defects.[48]

However, interstitial halogen defects I_i can introduce deep-level states, leading to faster carrier recombination and thereby, reducing the material's efficiency in solar cell applications.[48] Therefore, defect passivation is necessary.

1.2 PL properties

The PL is a critical factor for regulating the performance of LHP-based optoelectronic devices.[49] When these materials absorb photons with energy equal to or higher than its bandgap, electrons in the VB are transferred to the CB, creating electron-hole pairs. The excited carriers release excess energy as heat and relax to the CBM. The band edge

electron falls back to the VB by emitting a photon which results in PL. The energy of the emitted photon is smaller compared to the absorbed photon; a phenomenon known as the Stokes shift. When excited charge carriers recombine without emitting photons, it is called nonradiative recombination. For hybrid organic-inorganic HPs, the exciton binding energy is relatively low, making thermal dissociation possible at room temperature, that can lead to both free-carrier and excitonic luminescence.[50] Sometimes, the excited electron can undergo a transition from the singlet state to a triplet state by intersystem crossing which causes phosphorescence. Since singlet-to-triplet transitions are spin-forbidden, intersystem crossing is typically slower than other radiative transitions.

The PL lifetime and the PLQY are the measure of the efficiency of PL in a material. The PL lifetime is the time an electron stays at an excited state. On the other hand, PLQY is a measure of a material's efficiency in emitting light when it absorbs photons. Mathematically, PLQY can be expressed as -

$$\text{PLQY} = \frac{\text{Number of absorbed photons}}{\text{Number of emitted photons}} \times 100\%$$

The nonradiative carrier recombination decreases the value of PLQY. HPs can exhibit different PL behaviors when fabricated in different forms like polycrystalline structures, single crystals, PNCs, or PNC films. These structural variations influence factors such as defect density, grain boundaries, and surface states, all of which can affect PL efficiency and stability.

HP polycrystalline film is composed of small crystallines oriented in various directions (Figure 1.7a). The small size crystal grains, misaligned orientations, numerous grain boundaries, abundant defects, and significant surface roughness are responsible for their degradation in the external environment.[51, 52] Polycrystalline films can be prepared by different methods, including spin coating, vapor deposition, blade coating, dip coating, and spray coating. Solution-processing polycrystalline films usually exhibit low PL quantum efficiencies (PLQE). By altering fabrication conditions, the grain diameter of LHP thin films can be systematically manipulated. It has been observed that as the grain size increases, the PL peak tends to shift toward lower energy levels.[53] Typically, the grain

sizes of a polycrystalline thin film sample exceed several hundred nanometers,

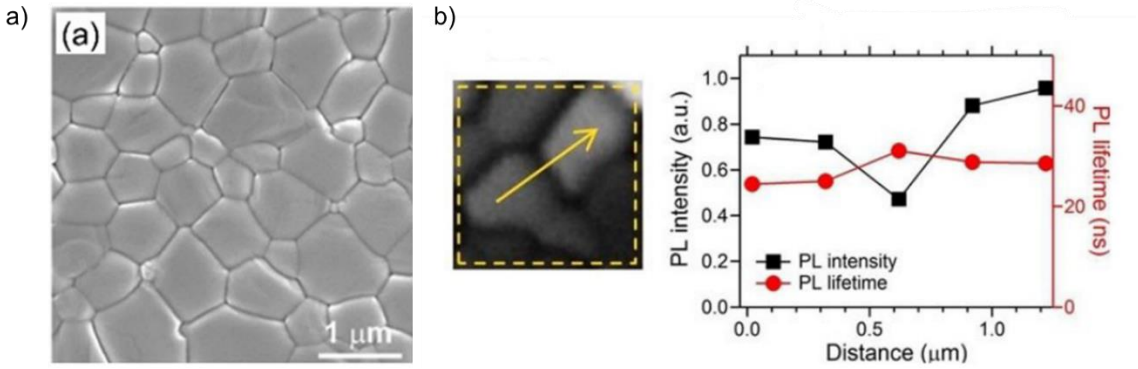

Figure 1.7. SEM (a) image of $MAPbI_3$ thin film representing grain boundaries. (a) $MAPbI_3$ polycrystalline film dark grain boundaries with boundary potential and PL obtained from Kelvin probe force microscopy studies. Both reproduced from Gegevičius *et al*.[54]

significantly larger than the exciton Bohr radius (e.g., 2.2 nm for $MAPbI_3$). As a result, the variations in PL peak energies for these films can't be attributed to quantum confinement effects commonly associated with PNCs and perovskite quantum dots (PQDs). Instead, the unusual redshift observed in films with μm-scale grains is attributed to reabsorption effects within the large crystals. This is due to the Stokes shift, where emitted photons are lower in energy than absorbed. Bulk perovskite often shows reabsorption emission (Figure 1.8). It occurs when emitted photons are reabsorbed by the material, leading to secondary emission at longer wavelengths.

However, PL properties also vary based on factors such as composition, preparation methods, and post-fabrication treatments.[55-57] It is reported that 100% efficiency can be achieved by post-synthesis passivation.[56] This indicates that in as-synthesized polycrystalline films, nonradiative recombination is predominant. Because the carriers are trapped at defect sites (Shockley-Read-Hall process). Sherkar *et al*. investigated the contribution of defects in nonradiative recombination in grain boundaries and interfaces.[58] They revealed that trap-assisted nonradiative recombination is predominant at the interface whereas, Braly *et al*. demonstrated that the surface is the main center of non-radiative recombination in this type of film.[56, 58]

Grain boundaries (GBs) generally appear as darker regions in PL images (Figure 1.7b), suggesting higher defect concentrations and increased nonradiative recombination

rates. deQuilettes *et al*. reported a 65% reduction in PL intensity at GBs.[59] However, other studies have shown different interpretations. For example, Tian *et al*. and Yang *et al*. found that PL lifetimes across GBs and within grains were comparable, even sometimes longer at the GBs, with reduced PL intensity possibly caused by carrier diffusion from GBs, creating a potential barrier (Figure 1.7b). [60, 61]

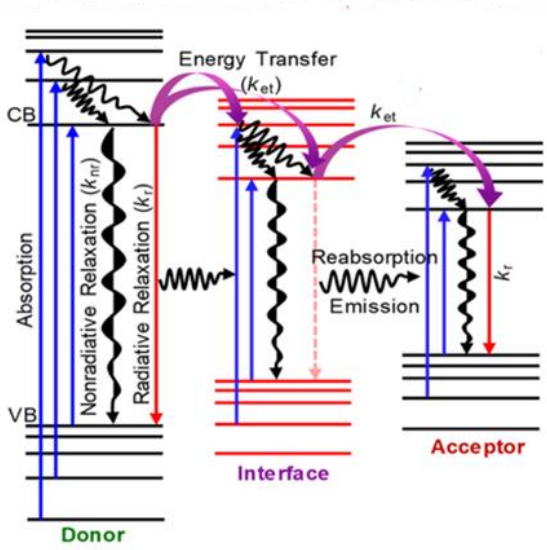

Figure 1.8. A diagram illustrating photon recycling and energy transfer at the heterojunction in the pellet of $MAPbBr_{3-x}I_x$.[62]

HP single crystal is free from grain boundaries because the crystal lattice is continuous throughout the entire crystal volume. It has less defect density compared to polycrystalline films, resulting in fewer trap states and nonradiative recombination sites. Single crystal trap density is between 10^{11} to 10^{9} cm^{-3}, almost 4 to 5 orders of magnitude smaller than that found in a polycrystalline LHP film.[63, 64 65, 66] Anti-solvent vapor-diffusion crystallization technique and the inverse temperature crystallization technique are the two widely accepted methods for the preparation of perovskite single crystal. Single crystals of LHPs exhibit significantly broader light absorption compared to thin films, often resulting in a redshift of their absorption onsets.[63] Shi *et al*. study of the optical absorption properties of $MAPbX_3$ single-crystal[64], as illustrated in Figure 1.9a, revealed a sharp absorption edge without any noticeable excitonic features, indicating a minimal presence of in-gap defect states. The bandgap of $MAPbBr_3$ and $MAPbI_3$ single crystals are 2.21 eV and 1.51 eV, respectively that are narrower bandgaps compared to their thin-film counterparts. Additionally, it exhibited narrow PL peaks near band edges.

Similarly, Zhumekenov *et al*. investigated the optical characteristics of the $FAPbX_3$ single crystals, as illustrated in Figure 1.9b.[67] Unlike polycrystalline films [68, 69], the single crystals displayed flat absorption profiles with a distinct band-edge cutoff and no evident excitonic features, indicating a lower in-gap defect density. Interestingly, these PL peaks showed a significant redshift compared to their counterparts in polycrystalline films (Figure 1.9c).[70, 71] This spectral shift originates from the high-order crystal structure and reduced defect density compared to polycrystalline film.

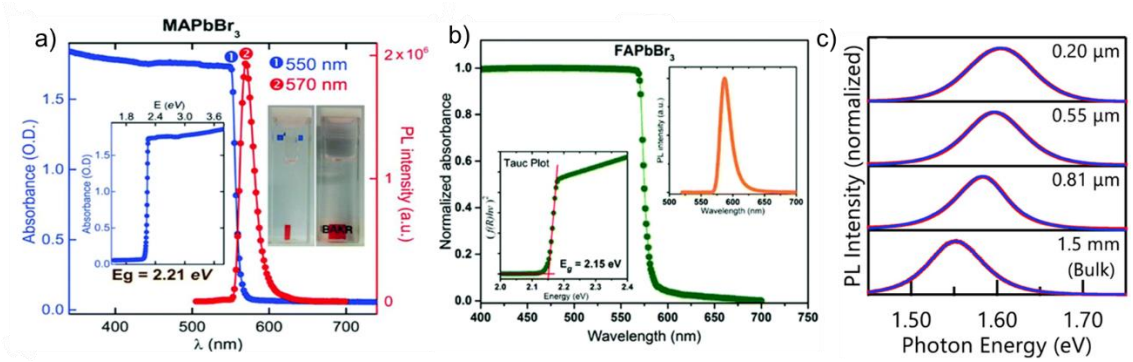

Figure 1.9. a-b) Absorption and PL spectra of $MAPbBr_3$[64] and $FAPbBr_3$[67] single crystal. c) PL spectral shift based on the crystal size.[72]

PL blinking is the variation of PL intensity of HPs between on and off states over time. Blinking mainly happens because of the Augur process or trapping at the defect site (Figure 1.10).[73] This trapping prevents radiative recombination because the trapped carrier is no longer available to recombine with its counterpart. This corresponds to the dark state of blinking. Trapped carriers can escape from the defect site due to thermal

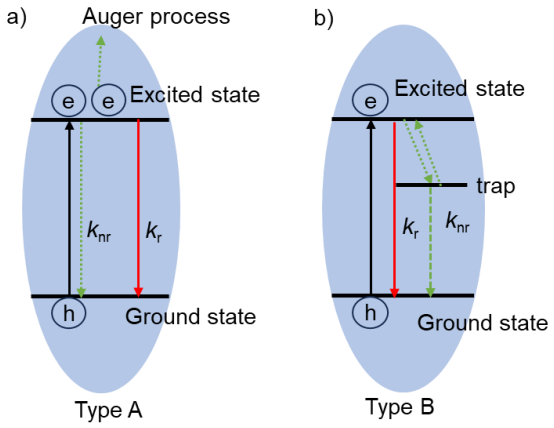

Figure 1.10. (a) Charging–discharging (type-A) and (b) the trapping-detrapping (type-B) mediated PL blinking.

activation or interaction with subsequent excitations. This corresponds to the bright state of blinking.

1.3. Nanocrystals and quantum dots

1.3.1 Synthesis and properties of PNCs and PQDs

The synthesis of LHP NCs and QDs involves preparing nanomaterials with distinctive optical and electronic characteristics. PNCs are commonly synthesized using solution-based methods, where a metal halide salt, such as lead iodide (PbI_2), is combined with an organic or inorganic halide, like MAI or CsI, in solvents such as DMF, DMSO, 1-hexadecane in presence of ligands like oleic acid, oleylamine, hexadecylamine. This reaction is often conducted at elevated temperatures to facilitate crystallization. A popular technique is the hot injection method (Figure 1.11a), where a hot precursor solution is rapidly inserted into another precursor to regulate the size and uniformity of the NCs. Surface passivating agents like oleic acid or oleylamine are used to improve the PNCs' stability and optical properties. On the other hand, QDs are typically synthesized through colloidal methods, where metal salts are mixed with organic ligands in a non-aqueous solvent like hexane or toluene. Heat is applied to promote the growth of PQDs, and careful control of reaction conditions allows for tuning their size and optical characteristics.

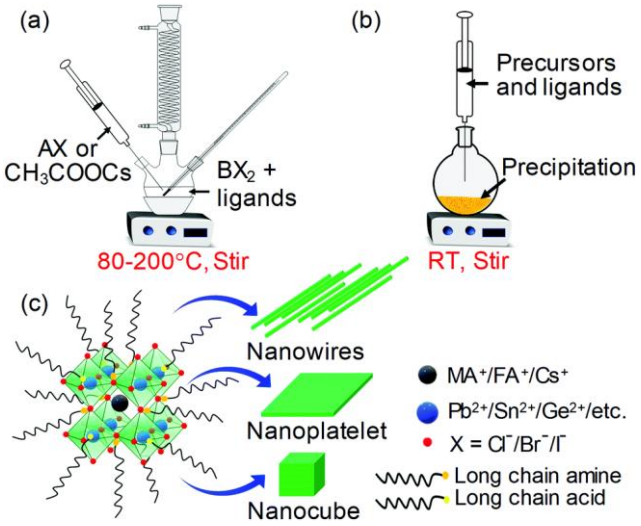

Figure 1.11. (a) PNCs synthesized following the hot-injection technique, and (b) the LARP method. (c) Ligand-coated PNCs exhibit various morphologies.

Schmidt *et al.* first mentioned the nanometer scale preparation of $CH_3NH_3PbBr_3$ perovskites with a size of around 6 nm.[74] These nanoparticles exhibit high stability, maintaining their integrity in both solid form and concentrated solutions for over

three months. They used octadecylammonium bromide, which can effectively cap the perovskite to maintain its crystal structure. The hot injection method is used typically to prepare $CsPbBr_3$ PNCs. In this synthesis process, cesium acetate with different kinds of ligands is first dissolved in 1-hexadecene at 120 °C. Meanwhile, a separate solution containing $PbBr_2$, oleic acid, and hexadecylamine is dissolved in the same solvent at the same temperature. The hot Cs-precursor solution is then injected into the $PbBr_2$ mixture at 170 °C. Quickly the reaction mixture is cooled using an ice water bath, and the NCs are separated and collected through centrifugation.[75] Similarly, 5-12 nm $FAPbBr_3$ PNCs are synthesized by injecting a FA-Pb precursor solution with oleic acid into octadecylammonium bromide in toluene maintaining a reaction temperature of 130 °C.[76] After 10 seconds, the reaction is stopped, and the PNCs are purified by washing the mixture with toluene and acetonitrile. $FAPbBr_3$ PQDs are also synthesized by injecting precursor solution in DMF to the hot ligand solution at 80 °C.[77] The LARP (Liquid–assisted recrystallization) method (Figure 1.11b) is another popular approach for synthesizing PNCs/PQDs in which synthesis is carried out at room temperature. Zhang *et al*. prepared 3.3 nm size $MAPbBr_3$ PQDs, following the reprecipitation method which involves adding a solution of precursor dropwise into the toluene-containing ligands under vigorous stirring.[78]

Ligands play an important role in synthesizing and stabilizing PNCs, influencing their morphology, size, surface properties, and optical/electronic characteristics. Ligands dictate the speed at which nucleation occurs and crystals grow by binding to specific facets of the LHP lattice. Depending upon the synthesis process and ligand used different types of nanomaterials are possible to synthesize (Figure 1.11c). Hydrophobic ligands (e.g., long alkyl chains) protect NCs from moisture-induced degradation and thermal instability. PNCs often show different PL properties from their bulk counterpart because of their size effect. With decreasing the size of NCs, quantum confinement effects lead to blue shifts in PL emission and enhanced PL intensity (Figure 1.12a). The confinement energy is primarily calculated by the size of the nanoparticle and its interaction with the surrounding environment. It can be determined by[79]-

$$\Delta E = \frac{\hbar^2 \pi^2}{2m^* r^2}$$

Where, m* denotes the exciton reduced mass, which is connected to the Bohr radius via the effective mass approximation, $\hbar$ is the reduced Planck constant, and r is the particle radius. The following equation can determine the bandgap (E_g) of a confined system[80]-

$$E_g = E_{g.bulk} + \Delta E_{confinement}$$

Here, $E_{g.bulk}$ is the bandgap of the material in its bulk (unconfined) state and $\Delta E_{confinement}$ is the change in the bandgap due to confinement effects.

Additionally, if quantum confinement decreases their PL properties resemble those observed in thin films. This is because the charge carriers experience less restriction in their movement. As a result, the material behaves more like a bulk material or thin film, where the electron-hole interactions are less pronounced, leading to a decrease in PL intensity and broader emission spectra.

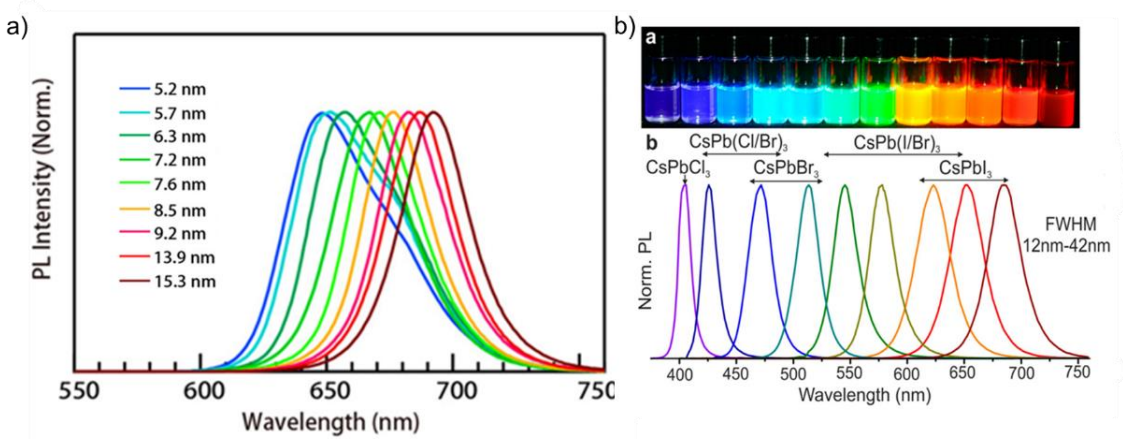

Figure 1.12. (a) Size-dependent tunable emission of $CsPbI_3$ PNCs.[81] (b) Colloidal $CsPbX_3$ PNCs (X = Cl, Br, I) show composition-dependent tunable emission which covers the entire UV-vis region.[82]

PNCs can also show halide-dependent optical emission (Figure 1.12b) like bulk, which can be readily achieved through post-synthetic halide exchange. However, in the case of bulk crystal, it isn't easy to obtain homogeneous halide exchange by post-synthetic treatment. PNCs show remarkable PLQY even without surface modifications making them potential for LEDs. When surface passivation techniques are applied, these efficiencies are further enhanced, and PL blinking behaviors are improved. Interestingly, anti-Stokes PL has also been detected in PNCs, sparking discussions about their potential

application in laser cooling.[83] In these NCs, reabsorption effects are minimal unless they are densely packed.

1.3.2 PNC films

LHP films are commonly utilized in various optoelectronic applications due to their exceptional characteristics, including high absorption efficiency, tunable band gaps, and excellent charge transport characteristics. Generally, a perovskite film is prepared in one step[84, 85], or two-step[86] (Figure 1.13) deposition of precursor solutions in DMF, DMSO, or GBL on glass slides by spin coating. Then the sample is annealed at a high temperature. PNC films can be fabricated by adding additives or ligands to the precursor solution.[87] The as-synthesized colloidal PNCs can also be spin-coated on glass and annealed to get PNC film. PNC In PNC films, the isolated PNCs are densely packed (Figure 1.14), which can lead to the overlap of the electronic wavefunction of adjacent NCs. This interaction can lower the effective bandgap, causing the emission peak to shift toward longer wavelengths (Figure 1.15).[88] PNC films exhibit excellent PLQY, low exciton binding energies, and efficient charge carrier generation, making them appropriate for applications in solar cells, LEDs, and lasers. Additionally, thin PNC film preparation is easy, maintaining their high carrier mobility, long diffusion lengths, and low defect densities.

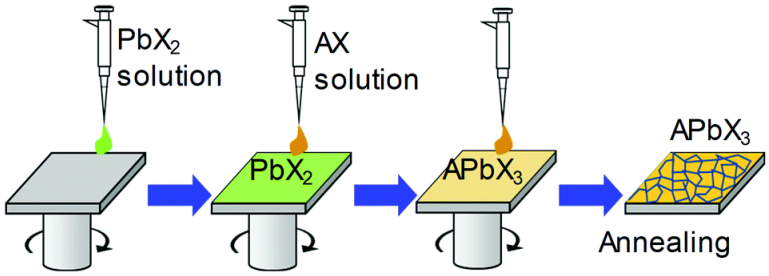

Figure 1.13. General procedure of perovskite film formation.[29]

The red shifting in PNC film can also be because of energy transfer[89] from one PNC to the adjacent PNC, or the band gap renormalization because of the electron-electron interactions. Electronic interactions between neighboring NCs can lead to energy transfer. This transfer often leads to a lowering of the emission energy, as the electron's energy state is effectively redistributed between PNCs with varying energy levels. The effect is

especially pronounced when the PNCs are tightly coupled, resulting in a broadening or red-shifting of absorption and emission spectra. On the other hand, when the densely packed PNCs are under high excitation power, the presence of electron-electron interactions modifies the local band structure, effectively narrowing the band gap. This shift can cause a red shift in both absorption and emission spectra.

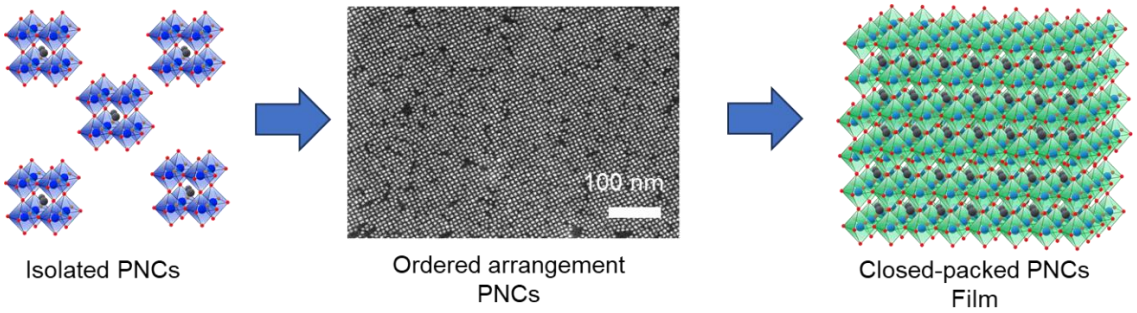

Figure 1.14. Thin films and assemblies of PNCs and PQDs.

The reabsorption emission is also found in the PNC film if the thickness of the film is large enough.[90] The PLQY of PNC film decreased compared to isolated PNC because of the opening of many nonradiative pathways including FRET and trap-assisted recombination. When PNCs aggregate in a film, the quantum confinement is less pronounced because the size of the individual particles in the aggregate is effectively larger than the exciton Bohr radius. As a result, the film exhibits behavior similar to bulk material, where quantum confinement is weaker or negligible. The FWHM in PNC film also increases because different degrees of interaction form particles of different sizes or shapes which contribute to a wider emission range.

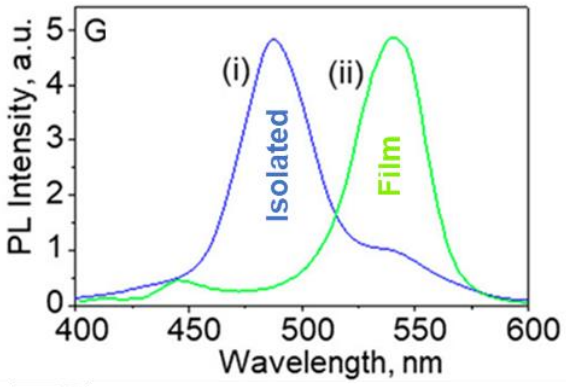

Figure 1.15. PL spectra shifting upon assembly formation of PNCs and PQDs.[91]

1.3.3 Exciton diffusion

Exciton diffusion is the process of photo-generated charge carriers (electrons and holes) transfer through the material. The fate of these carriers is the key property influencing the device's performance. HPs are interesting because of their long-range charge carrier diffusion length, increased carrier mobility, and low defect density, despite their relatively simple and cost-effective fabrication methods. In a highly confined system (PQD and PNC), there is a coulombic interaction between the carriers, and they exist as an exciton. In contrast, low-confined systems (polycrystalline film, single crystal, and thick PNC film) generate free carriers. When the exciton binding energy (E_b) is smaller compared to the thermal energy at room temperature (k_T), free carriers are generated. The ability of these carriers to travel significant distances before recombining is critical for efficient charge collection in devices. HPs show carrier lifetime from nanoseconds in QDs to several microseconds in films or assemblies. Various carrier relaxation processes decrease the carrier diffusion length presented in Figure 1.16. By considering the different carrier relaxation mechanisms, the free charge carrier density n(t) is calculated by the below rate equation[92]-

$$\frac{dn}{dr} = k_3 n^3 - k_2 n^2 - k_1 n$$

Here, k_1 corresponds to monomolecular recombination processes. k_2 represents intrinsic recombination between free electrons and holes (Figure 1.16). This process is influenced by the concentrations of electrons and holes. k_3 is the Auger recombination rate constant, a multi-particle interaction, that involves the annihilation of an electron and a hole, with the resulting energy and momentum transferred to another charge carrier, which can be either an electron or a hole. This process may also involve interactions with phonons.

Understanding carrier diffusion mechanisms in HPs involves examining intrinsic properties like the effective mass of carriers, the dielectric constant, and the interaction of carriers with phonons and defects. Advanced characterization techniques, including transient absorption spectroscopy, and time-resolved PL (TRPL), along with theoretical modeling, have been pivotal in uncovering these dynamics. Several models and experimental methods are used to calculate the charge carrier movement in LHPs. For

example, the Space-Charge-Limited Current (SCLC)[93] model measures the carrier mobility which is obtained from the current-voltage (I–V) characteristics in a perovskite device. Here, the LHP layer is placed between two electrodes and forms a sandwiched

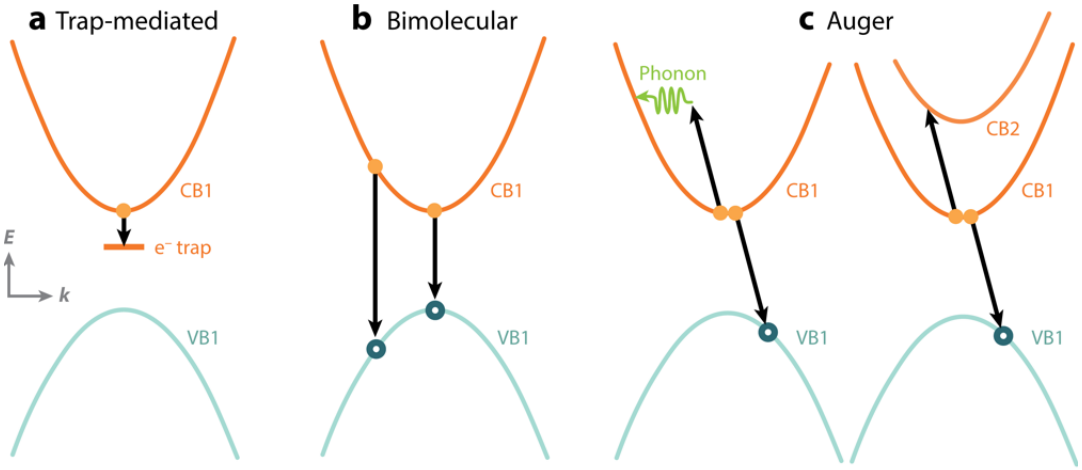

Figure 1.16. The recombination mechanisms in organic-inorganic metal HPs. a) Monomolecular trap-assisted process, b) bimolecular radiative recombination, and c) Auger recombination.[92]

structure. The current density J in the trap-free SCLC regime is given by:

$$J = \frac{9}{8} \epsilon \epsilon_0 \mu \frac{V^2}{L^3}$$

Where V denotes the applied voltage, ϵ is the relative permittivity of the material, ϵ_0 denotes the vacuum permittivity, L is the thickness of the perovskite layer, and μ is the charge carrier mobility. In the presence of traps, the equation is modified to account for the trap density. The other methods are Time-of-Flight (TOF), Hall Effect, Photoconductivity, Field-Effect Transistor (FET) Measurements, and Transient Photovoltage/Photocurrent (TPV/TPC). The charge carrier diffusion length (L_D) is typically calculated using the following equation[94]:

$$L_D = \sqrt{\frac{k_B T \mu \tau}{q}}$$

Here, k_B is Boltzmann constant, T denotes temperature, q is elementary charge, μ is carrier mobility, and τ is carrier lifetime.

Factors such as material composition, crystallinity, dimensionality (2D, 3D, or mixed-dimensional perovskites), and environmental stability all play vital roles in governing diffusion dynamics.

1.3.3.1 Exciton diffusion in polycrystalline films

In polycrystalline film, excitons are dissociated in free carriers very quickly. Piotr Piatkowsk *et al*. studied time-resolved terahertz (THz) spectroscopy of $FAPbI_3$ polycrystalline film. They reported that the weakly bonded and strongly bound excitons are dissociated into free carriers less than 1 ps and 20 ps respectively.[95] The movement of these charge carriers in polycrystalline HPs remains a topic of debate due to its complexity. This complexity arises from the interaction of two key processes: the movement of carriers within individual monocrystalline grains and their transport across grain boundaries. Grain boundaries are widely recognized for their significant influence on carrier dynamics in polycrystalline LHP films. Grain boundaries have structural defects and impurities that serve as sites for nonradiative recombination, adversely affecting the carrier diffusion length. Experimental studies suggest that the carrier mobilities in polycrystalline LHPs are generally smaller than those in single-crystal counterparts. Yet, this conclusion is complicated by the significant variability in reported mobility values. For instance, Jongchul Lim *et al.* reported mobility values for $MAPbI_3$ range widely, from 2.2 to 0.2 $cm^2\ V^{-1}\ s^{-1}$ between films[96], reflecting inconsistencies across different measurement techniques and material processing methods.

A reduction in carrier mobility has been reported for solution-processed polycrystalline LHP films[97], indicative of band-like charge transport similar to that observed in single-crystal systems. Conversely, studies have also documented an increase in carrier mobility with temperature[98, 99], implying a thermally activated hopping mechanism similar to charge transport in polysilicon. The diversity in results highlights the impact of GBs, defect densities, and fabrication methods on transport properties, necessitating more standardized characterization approaches for clearer comparisons.

Wenming Tian *et al.* reported unexpectedly high carrier diffusivities inside the gains of $CH_3NH_3PbI_3(Cl)$ polycrystalline films. These diffusivities, ranging from 1.5 to 3.3 cm^2/s, are equivalent to those observed in bulk single crystals. Additionally, the local PL

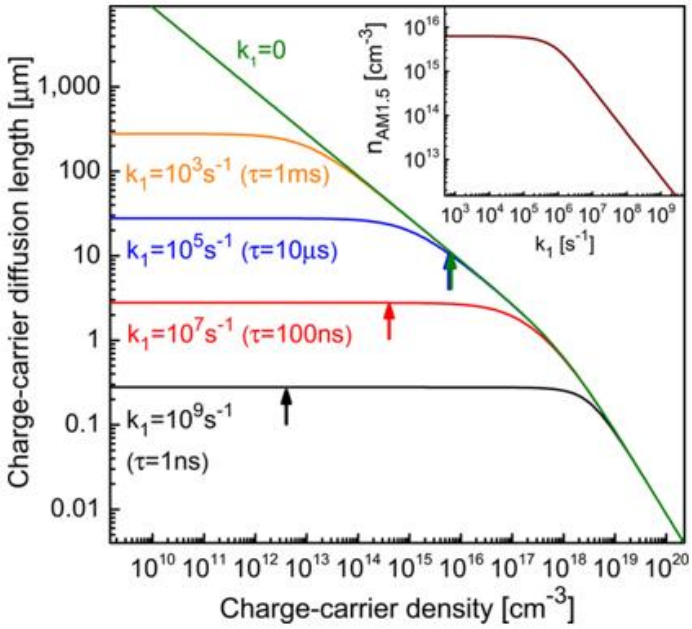

Figure 1.17. The diffusion lengths (L_D) of charge carriers in high-quality $MAPbI_3$ film have been determined as a function of charge-carrier density. This analysis considers a variety of monomolecular recombination rates (k_1), which are inversely related to the carrier lifetime (τ).[100]

lifetimes are approximately 200 ns, showing remarkable uniformity within individual grains and grain boundaries.[61] Another article reported the diffusion length of 25 μm (~75 $cm^2\ V^{-1}\ s^{-1}$) in the case of 210 nm $FAPbI_3$ polycrystalline film upon exciting above the absorption edge[95], which exceeds the diffusion length observed in single crystals. Considering different monomolecular recombination rates, the carrier diffusion in polycrystalline film can be higher up to 1ms (Figure 1.17). The carrier infusibility in the polycrystalline film also depends on the film's morphology. Adhyaksa *et al*. show different diffusion lengths when the polycrystalline film has a different morphology.[101]

1.3.3.2 Exciton diffusion in single crystals

Single crystal has a continuous and uniform crystal lattice without grain boundaries. This structure provides minimal scattering sites for carriers, allowing for more carrier lifetime and efficient diffusion (Figure 1.18). Shi *et al.* reported the $MAPbX_3$ ($X = Br^-, I^-$) LHP single crystals exhibit charge carrier diffusion lengths of more than 10 μm and possess an exceptionally low trap density in the range of 10^9 to 10^{10} cm^{-3}.[64] Different sizes of single

crystals have different carrier diffusion lengths. For instance, Yu Bi *et al*. reported the carrier diffusion length of $CH_3NH_3PbI_3$ having dimensions of 10 × 8 × 3 mm^3 can reach up to 50 μm.[102] Moreover, Dong *et al*. demonstrated the highest carrier diffusion lengths in $CH_3NH_3PbI_3$ single crystals synthesized through a solution-growth approach of more than 175 μm when exposed to 1 sun illumination. Furthermore, the carrier diffusion in

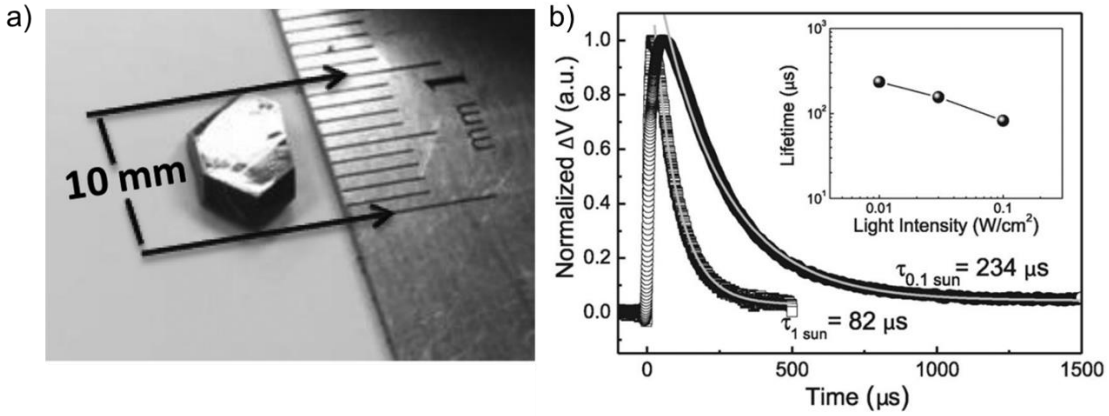

Figure 1.18. a) As-prepared $MAPbI_3$ single crystal. (b) The $MAPbI_3$ single-crystal device has a high carrier lifetime under 1 sun and 0.1 sun illumination. Both figures are reproduced from Dong *et al*.[63]

the case of Ruddlesden-Popper (RP) layered perovskites single crystal varies on the number of layers. Shrestha *et al*. measured the carrier diffusion length of RP single crystal using the scanning photocurrent microscopy method, which depends on different n values. They observed that as n decreased, the diffusion length also diminished.[103]

Due to their superior optoelectronic properties including carrier lifetime and carrier diffusion length, these kinds of bulk LHPs are more promising for application in solar cells, LED, lasing, and photodetectors. However, desired low-dimensional thin bulk LHPs (e.g. single crystal) are difficult to prepare, which is required for most of the optoelectronic device fabrication. In bulk LHPs, photogenerated charge carriers have to travel more distance to reach the charge transfer layer which increases its chance of radiative and nonradiative recombination (Figure 1.19). Moreover, this bulk LHP consumes large amounts of materials increasing the cost. Therefore, PNC films are getting more attention in this sense because of their easy synthesis of desired size film and excellent PLQY.

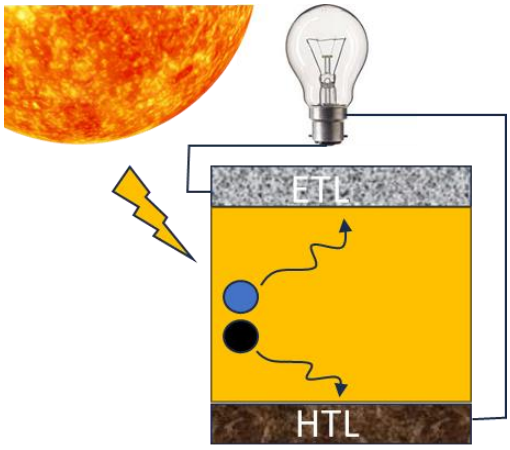

Figure 1.19. Extended carrier diffusion is essential in single-crystal LHP solar cells due to the larger thickness of the crystal.

1.3.3.3 Exciton diffusion in PNC films

When the dimensionality of HPs reduced to leverage quantum confinement effects, it introduces significant alterations to the lattice structure. This reduction is often achieved by incorporating insulating organic ligands, which disrupt the crystalline framework. Such modifications bring intriguing questions about the charge diffusion behavior within these materials, as the interplay between confined excitons, lattice disruptions, and organic barriers becomes increasingly complex.

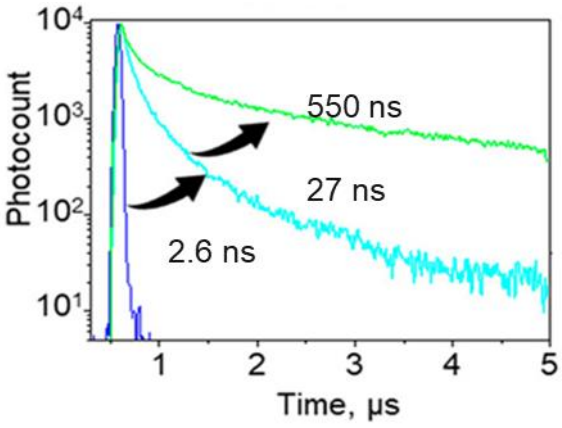

Figure 1.20. PL lifetime change of PNC during assembly formation.[91]

In conventional inorganic QD systems, such as cadmium selenide (CdSe) QDs, the exciton diffusion lengths are typically limited to just a few tens of nanometers.[104, 105] In contrast, PNC film can have longer exciton diffusion. Zhang *et al*. reported the carrier

lifetime increased upto the 550 ns during film formation (Figure 1.20).[91] The diffusion length of a carrier is directly related to its lifetime. Giovanni *et al.* reported that exciton diffusion in $CH_3NH_3PbBr_3$ PNC films exhibits remarkable behavior, having diffusion lengths exceeding 1 μm.[106] Notably, the exciton mobilities in their films can achieve values as high as 10 ± 2 cm^2 V^{-1} s^{-1}, which is unexpectedly multiple times longer than the carrier mobilities observed in three-dimensional (3D) LHP films. This extraordinary diffusion capability arises from a combination of highly efficient inter-PNC exciton hopping (Figure 1.21), facilitated by Förster resonance energy transfer, and a notable yet smaller contribution from photon recycling mechanisms. Nair *et al.* demonstrated the carrier hopping inside the NC film. They said that alkyl chain ligand helps to come closer to the PNC by hydrophobic interactions which helps to increase the carrier diffusion[107].

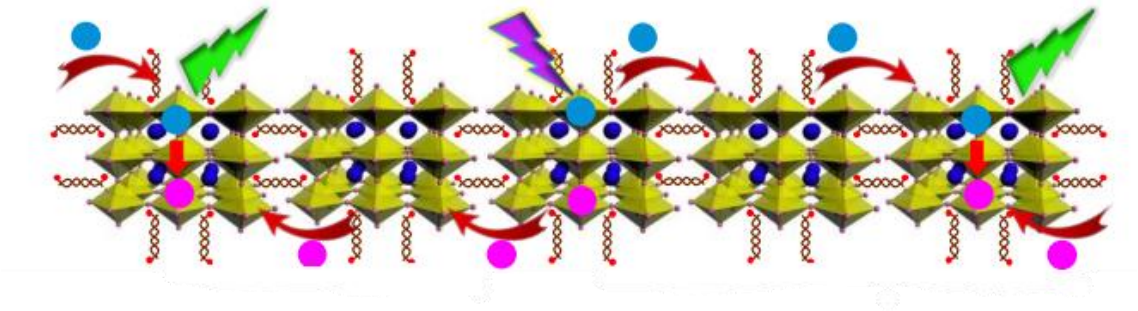

Figure 1.21. Charge carrier diffusion in self-assembled PNCs.[108]

1.4 Carrier extraction

Carrier extraction in HPs refers to the process of efficiently collecting the photogenerated charge carriers/excitons from the LHP layer by the electrode. Efficient carrier extraction is crucial for increasing the efficiency of HP-based devices because it directly impacts the device's efficiency by reducing losses due to radiative and non-radiative recombination. Because of the direct band gap nature, low exciton binding energies, high light absorption, exceptional charge mobility, and long charge carrier diffusion lengths, HPs show balanced ambipolar charge transport.[109] Theoretically, this allows PSCs to operate without additional carrier transport layers, as the HP layer itself can enable direct transfer of generated carriers to the electrodes.[110] Shi *et al*. demonstrated the ETL-free PSC fabricated with $MAPbI_3$ achieves a maximum PCE of nearly 13%.[109] The reported maximum efficiency obtained without a charge transport layer is around 20%.[111] However,

despite these potential benefits, devices without charge transport layers generally exhibit lower PCEs compared to those with optimized CTLs.

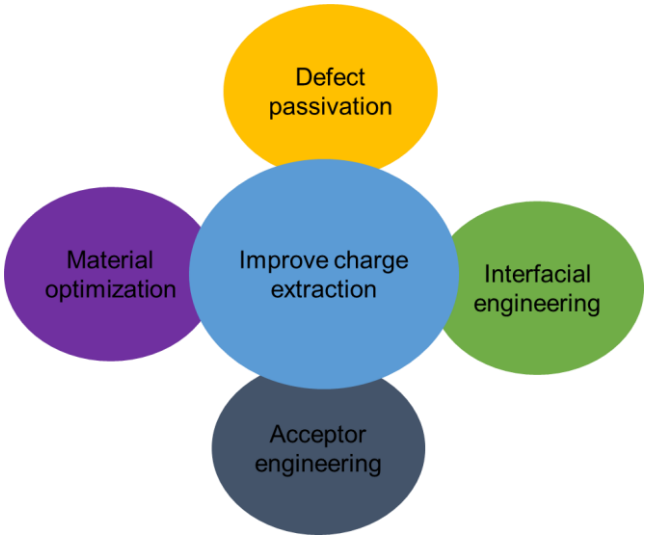

Figure 1.22. Various strategies used to improve charge carrier extraction from the LHP active layer.

Recently, there are different types of HTL and ETL have been utilized to increase the efficiency of carrier extraction from LHPs. While HTLs and ETLs are crucial for selectively guiding holes and electrons to the respective electrodes, their interactions with perovskite layers introduce several issues impacting device performance, stability, and scalability. Energy level misalignment, interface-induced recombination, poor stability of transport layers, and low conductivity of common issues of charge transport layers. Therefore, various strategies (Figure 1.22) are reported by the researcher to improve the charge extraction which is discussed in the next section.

1.4.1 Strategies to improve carrier extraction

1.4.1.1 Material optimization

Material optimization can be done by adjusting the ratio of lead, halides, and organic-inorganic cations which tune the bandgap and stability. Consequently, the carrier transport improves. Introducing 2D perovskite layers upon the 3D structure can enhance stability, and passivate surface defects. Singh *et al*. reported the rapid carrier extraction in 2D/3D PSCs compared to 3D PSCs.[112] Different types of additives are incorporated into the perovskite precursor material to decrease the crystal grain and reduce defects. For

instance, studies by Wang *et al*. revealed that low concentrations of Al^{3+} doping reduced crystal defects due to decreased micro strain in the lattice of $MAPbI_3$. Additionally, this doping lowered urbach energy from 13.09 to 12.64 meV, indicating less lattice disorder and suggesting enhanced electronic properties of the perovskite films.[113] Similarly, monovalent cations such as Cu^+, Na^+, and Ag^+, with ionic radius comparable to Pb^{2+}, have been suggested for surface or grain boundary passivation.[114]

1.4.1.2 Defect passivation

Like other semiconductor materials, HPs also contain defects. It is reported that defects with low formation energy inset shallow traps whereas high formation energy defects introduce deep traps inside the bandgap. These function as a center for nonradiative recombination.[115] On the other hand, organic cations are volatile creating further defects in the crystal upon interaction with light and heat.[116] Recently, Li *et al*. showed that the use of Rb to fill the vacancy of A site MA cation increases carrier transport by reducing nonradiative recombination.[116] Jiang *et al.* achieved comparable improvements by applying phenethylammonium iodide, an organic halide salt, onto $HC(NH_2)_2$–CH_3NH_3 mixed LHP films to decrease surface defects.[117] Liao *et al*. demonstrated the use of a 2D polymer semiconductor on a perovskite to passivate defects at the GBs and/or surface which improves charge extraction and transport.[118]

1.4.1.3 Interface engineering

Optimization of ETL (e.g., SnO_2, and TiO_2) and HTL (e.g., Spiro-OMeTAD, and PEDOT) is crucial for better alignment of energy bands, conductivity, and reduced recombination. Matching the energy levels of the perovskite with ETL and HTL can create a more favorable band alignment for efficient charge transfer. This can be accomplished by altering the materials used in transport layers or applying interfacial layers to shift energy levels. Using materials with high electron mobility and modifying them with surface treatments (e.g., UV-ozone, self-assembled monolayers) can improve electron extraction. Nanostructured or mesoporous ETLs also enhance charge collection. High-mobility hole transport materials can improve hole extraction. Adding ultra-thin buffer layers, such as LiF or organic molecules, within the perovskite and transport layers can minimize recombination and enhance carrier extraction.[119] Moreover, HP's interfacial passivation

using different methods can ensure intimate contact which reduces trap and facilitates carrier transport.

Reducing nonradiative recombination is necessary by surface defect passivation or interface engineering. Similarly, minimizing radiative recombination by ultrafast carrier extraction is equally important to enhance charge carrier extraction in HPs. Different charge acceptor molecules are reported in the literature including fullerene, carbon nanotube, TCNQ, TCNB, and 4,5-dibromofluorescein. A good acceptor can quickly extract carriers from the HPs and reduce recombination.

1.4.2 Biexciton and nonradiative Auger recombination

In semiconductor physics, a biexciton is a quasi-particle comprising two bound electron-hole pairs or excitons. On the other hand, multiexciton refers to a state where multiple excitons coexist within the same semiconductor nanostructure. These multi-particle complexes arise from attractive Coulomb interactions. They can be generated through single-photon or multi-photon excitation processes. Juska *et al.* reported that the resonant two-photon excitation can efficiently initialize biexciton states in semiconductor QDs.[120] In contrast, Fomichev *et al.* theoretically demonstrated that a biexciton can be generated in silicon nanostructures through single-photon excitation.[121] The phenomenon of the absorption of a single photon leads to the creation of more than one exciton in semiconductor materials, which is called multiple exciton generation (MEG).[122] This occurs when the photon energy significantly exceeds the material's bandgap. The excess energy absorbed is transferred to the creation of additional electron-hole pairs, rather than being dissipated as heat. MEG is particularly significant in materials with quantum confinement effects, where electron and hole interactions are enhanced.[123, 124]

Multiexcitons exhibit optical properties that differ from those of individual excitons. MEG offers several advantages, particularly in optoelectronic applications such as solar cells, light-emitting diodes, and lasers. One of the key benefits is the increased PLQY. In MEG, the material can produce a higher number of photons per absorbed photon, improving the efficiency of light emission. This enhancement in PLQY can be especially important for developing high-efficiency light sources and improving the performance of photodetectors.[125] Additionally, MEG enables simulated emission in the presence of an

external electromagnetic field, offering a pathway to create highly efficient lasing sources.[124] This capability is highly desirable for low-threshold lasers and optical amplifiers, where efficient photon generation and emission are essential. Moreover, MEG can enhance the performance of solar cells by creating more excitons from a single photon. The more charge carriers available for collection, the better the efficiency of solar cells.

Although MEG can significantly boost the performance of devices, it is also accompanied by challenges. For instance, Auger recombination, where the energy from one exciton is transferred to another exciton non-radiatively, can lead to energy loss.[126] This is particularly problematic in high-density exciton systems where the probability of these non-radiative processes is elevated. The rate of Auger recombination is often dependent on several factors, including the size of the PNCs (due to quantum confinement effects), the type of material, and the exciton density. Smaller QDs, for example, tend to have higher exciton densities, which can increase the likelihood of Auger recombination. In PSC, MEG increases the number of carriers to be extracted. However, slow extraction can initiate the Auger recombination. Therefore, to minimize this, quick carrier extraction is necessary.

1.5 Applications of halide perovskites

1.5.1 Solar cell

PSCs are gaining popularity due to their remarkable and rapid advancements in efficiency. After the pioneering work by Miyasaka in 2009, the next major advancement in PSCs came in 2012 from the research groups of Michael Grätzel and Nam-Gyu Park.[127] Their work showcased solid-state photovoltaic devices based on perovskite materials, achieving an efficiency of 9.7% where they used spiro-MeOTAD as a HTL. Now the PCE reaches up to 26% comparable to silicon solar cells. PSCs offer numerous benefits over traditional and emerging solar cells. For example, silicon solar cells need purified silicon, which involves heating sand at high temperatures (over 1000 °C). The production of silicon solar cells involves multiple steps, including wafer slicing, texturing, coating, and assembling into modules which require specialized facilities and energy, all of which contribute to higher manufacturing costs. In contrast, HPs can be produced through solution processing, enabling simpler, low-energy synthesis with common coating techniques. Some other emerging solar technologies, like organic solar cells (OSCs), are

generally less expensive and can also be processed in solution, unlike silicon solar cells. However, OSCs face challenges with their intrinsic properties, such as low dielectric constants which limit the generation of free charge carriers upon photoexcitation, low charge-carrier mobility, and limited charge-carrier diffusion lengths. In contrast, PSCs exhibit a higher dielectric constant, higher charge-carrier mobility, and greater diffusion lengths.

PSCs typically consist of multiple layers (Figure 1.23a). These include a transparent conductive oxide (TCO)-coated glass substrate, followed by an n-type ETL, a perovskite active layer, a p-type HTL, and a back-contact, which may be made of metal, TCO, or

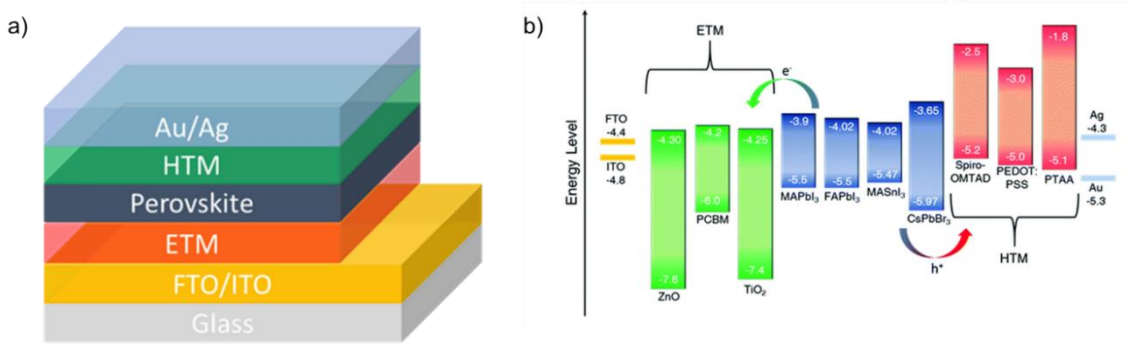

Figure 1.23. (a) Structure of a typical PSC. (b) Energy alignments of different electron-transport, hole-transport, perovskite, and electrode components. Both are reproduced from Chouhan *et al*.[29]

carbon. Each layer has a crucial function in facilitating the flow of the carriers and enhancing the cell's efficiency in producing electricity from sunlight. PSCs is either standard (n–i–p) or inverted (p–i–n), which depends on the arrangement of charge-selective layers. The operation of PSCs involves light absorption by the perovskite layer, which generates charge carriers that are subsequently extracted via the HTL and ETL to their respective electrodes. The properties of HTL and ETL are very important to effectively extract the photogenerated charge carrier. The optimal ETL material should possess high electron conductivity, well-matched energy level with the perovskite layer (Figure 1.23b), and high transparency to enable light to pass through and reach the active layer for absorption.[128, 129] Ideal HTL materials should have higher hole mobility, good stability, and appropriate energy level alignment with the perovskite layer. Common ETL includes TiO_2, TCNQ, TCNB, and HTL includes PDOT: PSS, spiro-MeOTAD. The

interfaces of PSCs are critical because they determine the efficiency of charge extraction and transport. Poor interface quality can lead to recombination losses, reducing the device's overall performance. Correct positioning of energy levels across the layers, as well as minimizing defects at the interfaces, ensures that the electron and hole currents flow effectively.

1.5.2 LED

The tunable PL and high PLQY of HPs have garnered significant interest in creating multicolor perovskite-based LEDs (PeLEDs).[130] While efforts to utilize HPs in LED applications began in the early 1990s, recently room-temperature multicolor PeLEDs have been successfully demonstrated. Notable advancements include achieving peak external quantum efficiencies (EQEs) of 20.3% for green[131] PeLEDs and 21.6% for red PeLEDs[132]. Blue PeLEDs, often based on pure chloride or mixed chloride-bromide perovskites, have also been developed.

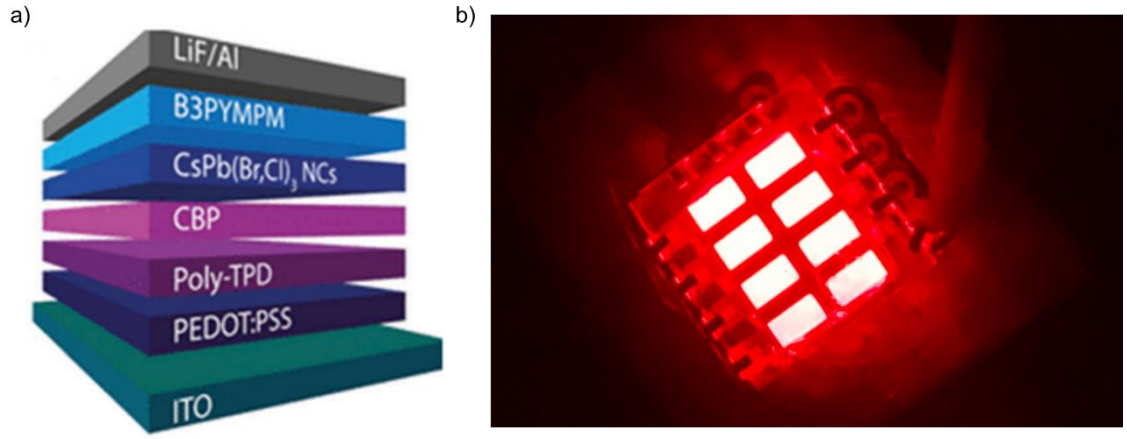

Figure 1.24. Structure of a typical PeLED (a).[29] Image of a red PeLED (b)[133]

LED is a multilayer structure device (Figure 1.24a) comprising a transparent conductive substrate (e.g., ITO), ETL, a perovskite emissive layer, an HTL, and a metal electrode.[134] The ETL was deposited on the substrate to facilitate electron injection. Next, HP is spin-coated or solution-processed to serve as the emissive layer. The HTL (e.g., Spiro-OMeTAD or PEDOT: PSS) is then applied to inject hole. Finally, a reflective metal electrode (e.g., Au or Al) is deposited through thermal evaporation. Careful optimization of each layer and the interfaces is crucial to achieving higher efficiency with balanced color mixing and high device stability. When a voltage is applied to the LED, electrons

are introduced from the ETL, while holes are injected from the HTL. As electrons and holes meet at the p-n junction, they recombine. During this recombination process, the electrons lose energy, which is released in the form of photons (light). This is the key principle of how LEDs emit light.

1.5.3 Laser

The impressive PLQY, low defect density, and high absorption capability of LHPs make it highly potential for lasing applications. In 2015, Yakunin *et al*. reported that the solution-processed $CsPbX_3$ (where X = Cl, Br, I) NCs have low-threshold amplified spontaneous emission (ASE).[135] After that research on lasing and ASE has expanded to

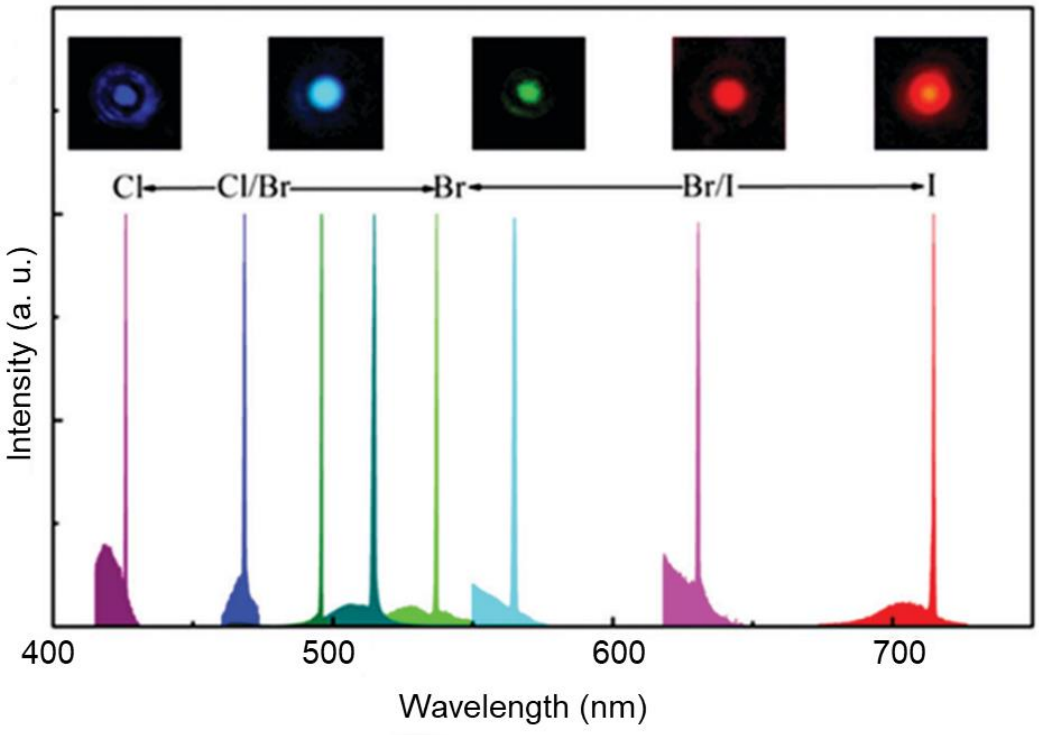

Figure 1.25. The multicolor single-mode lasing and the associated emission patterns of $CsPbX_3$ microspheres.[29]

explore various forms of HPs. As the intensity of the excitation light increases, the emission shifts to the narrow, red-shifted peak from broad spontaneous emission (SE) which is indicative of ASE behavior. Moreover, single-mode and multimode lasing, characterized by an ultra-narrow emission spectrum and high quality (Q) factor, have been achieved in these materials. The Q factor is a measure of the damping or energy loss in a resonant system, such as a laser cavity. It quantifies how sharply the system

resonates at its natural frequency. A high Q factor indicates that the system can store energy efficiently with minimal energy loss over time.

In the context of lasers, a high Q factor implies that the laser has a narrow emission linewidth, meaning it can emit light with a very specific frequency or wavelength. This leads to high spectral purity and stability, which is desirable for applications requiring precise and controlled emission. The lasing wavelength in HPs can be changed across the visible to NIR range by adjusting the halide composition (Figure 1.25). Lasing has been demonstrated in all types of HPs, using various cavity configurations, including vertical microcavities, random cavities, Fabry–Pérot cavities, and Whispering Gallery Mode cavities. Cavities play a crucial role in facilitating lasing by providing a confined space where light can be amplified and sustain oscillations. They achieve this by creating resonant conditions, where light bounces between reflective surfaces, such as mirrors or other optical structures, repeatedly stimulating the lasing material. This repeated stimulation leads to the amplification of light through stimulated emission, which is the core mechanism of lasing. The cavity also ensures that only specific wavelengths of light, corresponding to the resonance modes, are amplified, allowing for coherent and monochromatic light output. By controlling the geometry and reflective properties of the cavity, it is possible to fine-tune the lasing threshold, emission linewidth, and overall efficiency of the laser.

1.6 Motivation and objective of this research

In addition to the outstanding photophysical and optoelectronic properties of HPs, their solution processability and cost-effective synthesis processes positioned them as promising candidates for next-generation photovoltaic applications. HPs possess low exciton binding energy which make excitons dissociate into free carriers at room temperature without requiring additional power. The quick dissociation reduces the likelihood of electron-hole recombination. Extended carrier diffusion is necessary for improving the efficiency of devices. Bulk perovskites have increased carrier lifetime and extended carrier diffusion length making them suitable for application in solar cells and other photovoltaic devices. However, low-dimension thin film preparation is difficult using bulk perovskite. Therefore, perovskite NCs gaining popularity due to the ease of synthesizing films with the desired thickness. When PNCs are organized to form self-

assembly, the carrier lifetime and carrier diffusion increase. Moreover, defect-free NCs further enhance carrier migration and efficient carrier extraction because of the low degree of non-radiative recombination. To minimize radiative recombination at the interface, quick extraction of diffused electrons from NC films to ETL is necessary. Therefore, defect passivation, systematic arrangement of PNC, and interfacial engineering are important. Although researchers trying to solve these issues, significant scope of improvement in this field remains. In Chapter 3, I have focused on the defect passivation in isolated $CsPbBr_3$ PNCs using different bromide salts at the organic-aqueous interface. In Chapter 4, I investigated the formation of $FAPbBr_3$ PQD assembly in the polymer microenvironment. In this Chapter, I also reported the modulation of the exciton/carrier recombination by reversibly making and breaking the assembly using heat. In Chapter 5, I focused on the multiwall carbon nanotube template-assisted arrangement of $CsPbBr_3$ PNCs and ultrafast carrier extraction from PNCs to multiwall carbon nanotubes. This work contributes valuable insights toward fabricating PSCs with improved efficiency.

References

(1) Ortega-San-Martin, L. Introduction to perovskites: A historical perspective. *Revolution of Perovskite: Synthesis, Properties and Applications* **2020**, 1-41.

(2) Attfield, J. P.; Lightfoot, P.; Morris, R. E. Perovskites. *Dalton Transactions* **2015**, *44* (23), 10541-10542.

(3) Shirane, G.; Hoshino, S.; Suzuki, K. Crystal structure of lead titanate and of lead-barium titanate. *Journal of the Physical Society of Japan* **1950**, *5* (6), 453-455.

(4) Vegas, A.; Vallet-Regi, M.; Gonzalez-Calbet, J.; Alario-Franco, M. The $ASnO_3$ (A= Ca, Sr) perovskites. *Acta Crystallographica Section B: Structural Science* **1986**, *42* (2), 167-172.

(5) Rupprecht, G.; Bell, R. Dielectric constant in paraelectric perovskites. *Physical Review* **1964**, *135* (3A), A748.

(6) Alvarez, G.; Conde-Gallardo, A.; Montiel, H.; Zamorano, R. About room temperature ferromagnetic behavior in $BaTiO_3$ perovskite. *Journal of Magnetism and Magnetic Materials* **2016**, *401*, 196-199.

(7) Warren, W.; Robertson, J.; Dimos, D.; Tuttle, B.; Pike, G.; Payne, D. Pb displacements in $Pb(Zr,Ti)O_3$ perovskites. *Physical Review B* **1996**, *53* (6), 3080.

(8) Khirnyi, V. Properties of internal (chemical) pressure in superconducting $YBa_2Cu_3O_{7-y}$ perovskite created by oxygen. *Functional Materials* **2014**.

(9) Kalmykova, T.; Tarapov, S.; Neduch, S.; Krivoruchko, V.; Danilenko, I.; Burchovetckii, V.; Gurtovoj, D. Peculiarities of electromagnetic waves absorption in polymer magnetic nanocomposites (La, Sr) MnO_3. *Functional Materials* **2012**.

(10) Pandey, D. Keynote Lecture. *Acta Cryst* **2014**, *70*, C11.

(11) Wells, H. L. Über die cäsium-und kalium-bleihalogenide. *Zeitschrift für anorganische Chemie* **1893**, *3* (1), 195-210.

(12) Møller, C. K. Crystal structure and photoconductivity of caesium plumbohalides. *Nature* **1958**, *182* (4647), 1436-1436.

(13) Weber, D. $CH_3NH_3SnBr_xI_{3-x}$ (x= 0-3), ein Sn (II)-system mit kubischer perowskitstruktur/$CH_3NH_3SnBr_xI_{3-x}$ (x= 0-3), a Sn (II)-system with cubic perovskite structure. *Zeitschrift für Naturforschung B* **1978**, *33* (8), 862-865.

(14) Kojima, A.; Teshima, K.; Shirai, Y.; Miyasaka, T. Organometal halide perovskites as visible-light sensitizers for photovoltaic cells. *Journal of the American Chemical Society* **2009**, *131* (17), 6050-6051.

(15) Liu, S.; Li, J.; Xiao, W.; Chen, R.; Sun, Z.; Zhang, Y.; Lei, X.; Hu, S.; Kober-Czerny, M.; Wang, J. Buried interface molecular hybrid for inverted perovskite solar cells. *Nature* **2024**, *632* (8025), 536-542.

(16) Lin, H.; Yang, M.; Ru, X.; Wang, G.; Yin, S.; Peng, F.; Hong, C.; Qu, M.; Lu, J.; Fang, L. Silicon heterojunction solar cells with up to 26.81% efficiency achieved by

electrically optimized nanocrystalline-silicon hole contact layers. *Nature Energy* **2023**, *8* (8), 789-799.

(17) Ma, L.; Yan, Z.; Zhou, X.; Pi, Y.; Du, Y.; Huang, J.; Wang, K.; Wu, K.; Zhuang, C.; Han, X. A polymer controlled nucleation route towards the generalized growth of organic-inorganic perovskite single crystals. *Nature Communications* **2021**, *12* (1), 2023.

(18) Shahjahan, M.; Yuyama, K. i.; Okamoto, T.; Biju, V. Heterojunction perovskite microrods prepared by remote-controlled vacancy filling and halide Exchange. *Advanced Materials Technologies* **2021**, *6* (2), 2000934.

(19) Zhang, D.; Okamoto, T.; Biju, V. Thermodynamically and kinetically controlled nucleation and growth of halide perovskite single crystals. *Small* **2023**, *19* (48), 2304900.

(20) Sachith, B. M.; Zhang, Z.; Subramanyam, P.; Subrahmanyam, C.; Furube, A.; Tamai, N.; Okamoto, T.; Misawa, H.; Biju, V. Photoinduced interfacial electron transfer from perovskite quantum dots to molecular acceptors for solar cells. *Nanoscale* **2023**, *15* (17), 7695-7702.

(21) Sarangi, A.; Basavarajappa, M. G.; Chakraborty, S. Tuning composition space in lead-free divalent and tetravalent halide perovskite: a critical review. *Emergent Materials* **2022**, *5* (4), 1021-1032.

(22) Giuri, A.; Vanni, N.; Ahmad, M.; Rolston, N.; Corcione, C. E.; Listorti, A.; Colella, S.; Rizzo, A. Incorporation of Functional Polymers into Metal Halide Perovskites thin-films: from interactions in solution to crystallization. *Materials Advances* **2023**.

(23) Su, Y.; Yang, J.; Rao, H.; Zhong, Y.; Sheng, W.; Tan, L.; Chen, Y. Environmentally friendly anti-solvent engineering for high-efficiency tin-based perovskite solar cells. *Energy & Environmental Science* **2023**, *16* (5), 2177-2186.

(24) Ou, Q.; Bao, X.; Zhang, Y.; Shao, H.; Xing, G.; Li, X.; Shao, L.; Bao, Q. Band structure engineering in metal halide perovskite nanostructures for optoelectronic applications. *Nano Materials Science* **2019**, *1* (4), 268-287.

(25) Manser, J. S.; Christians, J. A.; Kamat, P. V. Intriguing optoelectronic properties of metal halide perovskites. *Chemical Reviews* **2016**, *116* (21), 12956-13008.

(26) Koutselas, I. B.; Ducasse, L.; Papavassiliou, G. C. Electronic properties of three-and low-dimensional semiconducting materials with Pb halide and Sn halide units. *Journal of Physics: Condensed Matter* **1996**, *8* (9), 1217.

(27) Chiarella, F.; Zappettini, A.; Licci, F.; Borriello, I.; Cantele, G.; Ninno, D.; Cassinese, A.; Vaglio, R. Combined experimental and theoretical investigation of optical, structural, and electronic properties of $CH_3NH_3SnX_3$ thin films (X= Cl, Br). *Physical Review B—Condensed Matter and Materials Physics* **2008**, *77* (4), 045129.

(28) Umebayashi, T.; Asai, K.; Kondo, T.; Nakao, A. Electronic structures of lead iodide based low-dimensional crystals. *Physical Review B* **2003**, *67* (15), 155405.

(29) Chouhan, L.; Ghimire, S.; Subrahmanyam, C.; Miyasaka, T.; Biju, V. Synthesis, optoelectronic properties and applications of halide perovskites. *Chemical Society Reviews* **2020**, *49* (10), 2869-2885.

(30) Even, J.; Pedesseau, L.; Jancu, J.-M.; Katan, C. Importance of spin–orbit coupling in hybrid organic/inorganic perovskites for photovoltaic applications. *The Journal of Physical Chemistry Letters* **2013**, *4* (17), 2999-3005.

(31) Utzat, H.; Sun, W.; Kaplan, A. E.; Krieg, F.; Ginterseder, M.; Spokoyny, B.; Klein, N. D.; Shulenberger, K. E.; Perkinson, C. F.; Kovalenko, M. V. Coherent single-photon emission from colloidal lead halide perovskite quantum dots. *Science* **2019**, *363* (6431), 1068-1072.

(32) Kepenekian, M.; Even, J. Rashba and Dresselhaus couplings in halide perovskites: Accomplishments and opportunities for spintronics and spin–orbitronics. *The Journal of Physical Chemistry Letters* **2017**, *8* (14), 3362-3370.

(33) Arya, M.; Bhumla, P.; Sheoran, S.; Bhattacharya, S. Rashba and Dresselhaus effects in doped methylammonium lead halide perovskite $MAPbI_3$. *Physical Chemistry Chemical Physics* **2024**, *26* (13), 10419-10426.

(34) Fedorov, D. G.; Koseki, S.; Schmidt, M. W.; Gordon, M. S. Spin-orbit coupling in molecules: Chemistry beyond the adiabatic approximation. *International Reviews in Physical Chemistry* **2003**, *22* (3), 551-592.

(35) Wulfsberg, G. *Inorganic Chemistry*; University Science books, 2000.

(36) Wang, T.; Daiber, B.; Frost, J. M.; Mann, S. A.; Garnett, E. C.; Walsh, A.; Ehrler, B. Indirect to direct bandgap transition in methylammonium lead halide perovskite. *Energy & Environmental Science* **2017**, *10* (2), 509-515.

(37) Motta, C.; El-Mellouhi, F.; Kais, S.; Tabet, N.; Alharbi, F.; Sanvito, S. Revealing the role of organic cations in hybrid halide perovskite $CH_3NH_3PbI_3$. *Nature Communications* **2015**, *6* (1), 1-7.

(38) Mahajan, S. Defects in semiconductors and their effects on devices. *Acta Materialia* **2000**, *48* (1), 137-149.

(39) Queisser, H. J.; Haller, E. E. Defects in semiconductors: some fatal, some vital. *Science* **1998**, *281* (5379), 945-950.

(40) McCluskey, M. D.; Janotti, A. Defects in semiconductors. *Journal of Applied Physics* **2020**, *127* (19).

(41) Gao, F.; Zhao, Y.; Zhang, X.; You, J. Recent progresses on defect passivation toward efficient perovskite solar cells. *Advanced Energy Materials* **2020**, *10* (13), 1902650.

(42) Ball, J. M.; Petrozza, A. Defects in perovskite-halides and their effects in solar cells. *Nature Energy* **2016**, *1* (11), 1-13.

(43) Ono, L. K.; Liu, S.; Qi, Y. Reducing detrimental defects for high-performance metal halide perovskite solar cells. *Angewandte Chemie International Edition* **2020**, *59* (17), 6676-6698.

(44) Ye, J.; Byranvand, M. M.; Martínez, C. O.; Hoye, R. L.; Saliba, M.; Polavarapu, L. Defect passivation in lead-halide perovskite nanocrystals and thin films: toward efficient LEDs and solar cells. *Angewandte Chemie* **2021**, *133* (40), 21804-21828.

(45) Duan, L.; Uddin, A. Defects and stability of perovskite solar cells: a critical analysis. *Materials Chemistry Frontiers* **2022**, *6* (4), 400-417.

(46) Huang, H.; Bodnarchuk, M. I.; Kershaw, S. V.; Kovalenko, M. V.; Rogach, A. L. Lead halide perovskite nanocrystals in the research spotlight: stability and defect tolerance. *ACS Energy Letters* **2017**, *2* (9), 2071-2083.

(47) Jin, H.; Debroye, E.; Keshavarz, M.; Scheblykin, I. G.; Roeffaers, M. B.; Hofkens, J.; Steele, J. A. It's a trap! On the nature of localised states and charge trapping in lead halide perovskites. *Materials Horizons* **2020**, *7* (2), 397-410.

(48) Liu, Q.; Li, A.; Chu, W.; Prezhdo, O. V.; Liang, W. Influence of intrinsic defects on the structure and dynamics of the mixed Pb–Sn perovskite: first-principles DFT and NAMD simulations. *Journal of Materials Chemistry A* **2022**, *10* (1), 234-244.

(49) Stranks, S. D.; Hoye, R. L.; Di, D.; Friend, R. H.; Deschler, F. The physics of light emission in halide perovskite devices. *Advanced Materials* **2019**, *31* (47), 1803336.

(50) Miyata, A.; Mitioglu, A.; Plochocka, P.; Portugall, O.; Wang, J. T.-W.; Stranks, S. D.; Snaith, H. J.; Nicholas, R. J. Direct measurement of the exciton binding energy and effective masses for charge carriers in organic–inorganic tri-halide perovskites. *Nature Physics* **2015**, *11* (7), 582-587.

(51) Boyd, C. C.; Cheacharoen, R.; Leijtens, T.; McGehee, M. D. Understanding degradation mechanisms and improving stability of perovskite photovoltaics. *Chemical Reviews* **2018**, *119* (5), 3418-3451.

(52) Wang, Q.; Chen, B.; Liu, Y.; Deng, Y.; Bai, Y.; Dong, Q.; Huang, J. Scaling behavior of moisture-induced grain degradation in polycrystalline hybrid perovskite thin films. *Energy & Environmental Science* **2017**, *10* (2), 516-522.

(53) D'Innocenzo, V.; Srimath Kandada, A. R.; De Bastiani, M.; Gandini, M.; Petrozza, A. Tuning the light emission properties by band gap engineering in hybrid lead halide perovskite. *Journal of the American Chemical Society* **2014**, *136* (51), 17730-17733.

(54) Gegevičius, R.; Franckevičius, M.; Gulbinas, V. The role of grain boundaries in charge carrier dynamics in polycrystalline metal halide perovskites. *European Journal of Inorganic Chemistry* **2021**, *2021* (35), 3519-3527.

(55) Richter, J. M.; Abdi-Jalebi, M.; Sadhanala, A.; Tabachnyk, M.; Rivett, J. P.; Pazos-Outón, L. M.; Gödel, K. C.; Price, M.; Deschler, F.; Friend, R. H. Enhancing photoluminescence yields in lead halide perovskites by photon recycling and light out-coupling. *Nature Communications* **2016**, *7* (1), 13941.

(56) Braly, I. L.; DeQuilettes, D. W.; Pazos-Outón, L. M.; Burke, S.; Ziffer, M. E.; Ginger, D. S.; Hillhouse, H. W. Hybrid perovskite films approaching the radiative limit with over 90% photoluminescence quantum efficiency. *Nature Photonics* **2018**, *12* (6), 355-361.

(57) Stranks, S. D.; Burlakov, V. M.; Leijtens, T.; Ball, J. M.; Goriely, A.; Snaith, H. J. Recombination kinetics in organic-inorganic perovskites: excitons, free charge, and subgap states. *Physical Review Applied* **2014**, *2* (3), 034007.

(58) Sherkar, T. S.; Momblona, C.; Gil-Escrig, L.; Avila, J.; Sessolo, M.; Bolink, H. J.; Koster, L. J. A. Recombination in perovskite solar cells: significance of grain boundaries, interface traps, and defect ions. *ACS Energy Letters* **2017**, *2* (5), 1214-1222.

(59) DeQuilettes, D. W.; Jariwala, S.; Burke, S.; Ziffer, M. E.; Wang, J. T.-W.; Snaith, H. J.; Ginger, D. S. Tracking photoexcited carriers in hybrid perovskite semiconductors: trap-dominated spatial heterogeneity and diffusion. *Acs Nano* **2017**, *11* (11), 11488-11496.

(60) Yang, M.; Zeng, Y.; Li, Z.; Kim, D. H.; Jiang, C.-S.; Van De Lagemaat, J.; Zhu, K. Do grain boundaries dominate non-radiative recombination in $CH_3NH_3PbI_3$ perovskite thin films? *Physical Chemistry Chemical Physics* **2017**, *19* (7), 5043-5050.

(61) Tian, W.; Cui, R.; Leng, J.; Liu, J.; Li, Y.; Zhao, C.; Zhang, J.; Deng, W.; Lian, T.; Jin, S. Limiting perovskite solar cell performance by heterogeneous carrier extraction. *Angewandte Chemie International Edition* **2016**, *55* (42), 13067-13071.

(62) Ghimire, S.; Takahashi, K.; Takano, Y.; Nakamura, T.; Biju, V. Photon recycling by energy transfer in piezochemically synthesized and close-packed methylammonium lead halide perovskites. *The Journal of Physical Chemistry C* **2019**, *123* (45), 27752-27758.

(63) Dong, Q.; Fang, Y.; Shao, Y.; Mulligan, P.; Qiu, J.; Cao, L.; Huang, J. Electron-hole diffusion lengths> 175 μm in solution-grown $CH_3NH_3PbI_3$ single crystals. *Science* **2015**, *347* (6225), 967-970.

(64) Shi, D.; Adinolfi, V.; Comin, R.; Yuan, M.; Alarousu, E.; Buin, A.; Chen, Y.; Hoogland, S.; Rothenberger, A.; Katsiev, K. Low trap-state density and long carrier diffusion in organolead trihalide perovskite single crystals. *Science* **2015**, *347* (6221), 519-522.

(65) Saidaminov, M. I.; Abdelhady, A. L.; Murali, B.; Alarousu, E.; Burlakov, V. M.; Peng, W.; Dursun, I.; Wang, L.; He, Y.; Maculan, G. High-quality bulk hybrid perovskite single crystals within minutes by inverse temperature crystallization. *Nature Communications* **2015**, *6* (1), 7586.

(66) Lian, Z.; Yan, Q.; Gao, T.; Ding, J.; Lv, Q.; Ning, C.; Li, Q.; Sun, J. Perovskite $CH_3NH_3PbI_3$(Cl) single crystals: rapid solution growth, unparalleled crystalline quality, and low trap density toward 108 cm–3. *Journal of the American Chemical Society* **2016**, *138* (30), 9409-9412.

(67) Zhumekenov, A. A.; Saidaminov, M. I.; Haque, M. A.; Alarousu, E.; Sarmah, S. P.; Murali, B.; Dursun, I.; Miao, X.-H.; Abdelhady, A. L.; Wu, T. Formamidinium lead halide perovskite crystals with unprecedented long carrier dynamics and diffusion length. *ACS Energy Letters* **2016**, *1* (1), 32-37.

(68) Hanusch, F. C.; Wiesenmayer, E.; Mankel, E.; Binek, A.; Angloher, P.; Fraunhofer, C.; Giesbrecht, N.; Feckl, J. M.; Jaegermann, W.; Johrendt, D. Efficient planar heterojunction perovskite solar cells based on formamidinium lead bromide. *The Journal of Physical Chemistry Letters* **2014**, *5* (16), 2791-2795.

(69) Rehman, W.; Milot, R. L.; Eperon, G. E.; Wehrenfennig, C.; Boland, J. L.; Snaith, H. J.; Johnston, M. B.; Herz, L. M. Charge-carrier dynamics and mobilities in

formamidinium lead mixed-halide perovskites. *Advanced Materials* **2015**, *27* (48), 7938-7944.

(70) Stoumpos, C. C.; Malliakas, C. D.; Kanatzidis, M. G. Semiconducting tin and lead iodide perovskites with organic cations: phase transitions, high mobilities, and near-infrared photoluminescent properties. *Inorganic chemistry* **2013**, *52* (15), 9019-9038.

(71) Eperon, G. E.; Stranks, S. D.; Menelaou, C.; Johnston, M. B.; Herz, L. M.; Snaith, H. J. Formamidinium lead trihalide: a broadly tunable perovskite for efficient planar heterojunction solar cells. *Energy & Environmental Science* **2014**, *7* (3), 982-988.

(72) Yamada, T.; Yamada, Y.; Kanemitsu, Y. Photon recycling in perovskite $CH_3NH_3PbX_3$ (X= I, Br, Cl) bulk single crystals and polycrystalline films. *Journal of Luminescence* **2020**, *220*, 116987.

(73) Chouhan, L.; Ito, S.; Thomas, E. M.; Takano, Y.; Ghimire, S.; Miyasaka, H.; Biju, V. Real-time blinking suppression of perovskite quantum dots by halide vacancy filling. *ACS Nano* **2021**, *15* (2), 2831-2838.

(74) Schmidt, L. C.; Pertegás, A.; González-Carrero, S.; Malinkiewicz, O.; Agouram, S.; Minguez Espallargas, G.; Bolink, H. J.; Galian, R. E.; Pérez-Prieto, J. Nontemplate synthesis of $CH_3NH_3PbBr_3$ perovskite nanoparticles. *Journal of the American Chemical Society* **2014**, *136* (3), 850-853.

(75) Ghimire, S.; Chouhan, L.; Takano, Y.; Takahashi, K.; Nakamura, T.; Yuyama, K.-i.; Biju, V. Amplified and multicolor emission from films and interfacial layers of lead halide perovskite nanocrystals. *ACS Energy Letters* **2018**, *4* (1), 133-141.

(76) Protesescu, L.; Yakunin, S.; Bodnarchuk, M. I.; Bertolotti, F.; Masciocchi, N.; Guagliardi, A.; Kovalenko, M. V. Monodisperse formamidinium lead bromide nanocrystals with bright and stable green photoluminescence. *Journal of the American Chemical Society* **2016**, *138* (43), 14202-14205.

(77) Khatun, M. F.; Okamoto, T.; Biju, V. Self-assembled halide perovskite quantum dots in polymer thin films showing temperature-controlled exciton recombination. *Chemical Communications* **2023**, *59* (93), 13831-13834.

(78) Zhang, F.; Zhong, H.; Chen, C.; Wu, X.-g.; Hu, X.; Huang, H.; Han, J.; Zou, B.; Dong, Y. Brightly luminescent and color-tunable colloidal $CH_3NH_3PbX_3$ (X= Br, I, Cl) quantum dots: potential alternatives for display technology. *ACS Nano* **2015**, *9* (4), 4533-4542.

(79) Butkus, J.; Vashishtha, P.; Chen, K.; Gallaher, J. K.; Prasad, S. K.; Metin, D. Z.; Laufersky, G.; Gaston, N.; Halpert, J. E.; Hodgkiss, J. M. The evolution of quantum confinement in $CsPbBr_3$ perovskite nanocrystals. *Chemistry of Materials* **2017**, *29* (8), 3644-3652.

(80) Di, D.; Musselman, K. P.; Li, G.; Sadhanala, A.; Ievskaya, Y.; Song, Q.; Tan, Z.-K.; Lai, M. L.; MacManus-Driscoll, J. L.; Greenham, N. C. Size-dependent photon emission from organometal halide perovskite nanocrystals embedded in an organic matrix. *The Journal of Physical Chemistry Letters* **2015**, *6* (3), 446-450.

(81) Zhao, Q.; Hazarika, A.; Schelhas, L. T.; Liu, J.; Gaulding, E. A.; Li, G.; Zhang, M.; Toney, M. F.; Sercel, P. C.; Luther, J. M. Size-dependent lattice structure and confinement properties in $CsPbI_3$ perovskite nanocrystals: negative surface energy for stabilization. *ACS Energy Letters* **2019**, *5* (1), 238-247.

(82) Protesescu, L.; Yakunin, S.; Bodnarchuk, M. I.; Krieg, F.; Caputo, R.; Hendon, C. H.; Yang, R. X.; Walsh, A.; Kovalenko, M. V. Nanocrystals of cesium lead halide perovskites ($CsPbX_3$, X= Cl, Br, and I): novel optoelectronic materials showing bright emission with wide color gamut. *Nano Letters* **2015**, *15* (6), 3692-3696.

(83) Morozov, Y. V.; Zhang, S.; Brennan, M. C.; Janko, B.; Kuno, M. Photoluminescence up-conversion in $CsPbBr_3$ nanocrystals. *ACS Energy Letters* **2017**, *2* (10), 2514-2515.

(84) Noel, N. K.; Stranks, S. D.; Abate, A.; Wehrenfennig, C.; Guarnera, S.; Haghighirad, A.-A.; Sadhanala, A.; Eperon, G. E.; Pathak, S. K.; Johnston, M. B. Lead-free organic–inorganic tin halide perovskites for photovoltaic applications. *Energy & Environmental Science* **2014**, *7* (9), 3061-3068.

(85) Jeon, N. J.; Na, H.; Jung, E. H.; Yang, T.-Y.; Lee, Y. G.; Kim, G.; Shin, H.-W.; Il Seok, S.; Lee, J.; Seo, J. A fluorene-terminated hole-transporting material for highly efficient and stable perovskite solar cells. *Nature Energy* **2018**, *3* (8), 682-689.

(86) Im, J.-H.; Jang, I.-H.; Pellet, N.; Grätzel, M.; Park, N.-G. Growth of $CH_3NH_3PbI_3$ cuboids with controlled size for high-efficiency perovskite solar cells. *Nature Nanotechnology* **2014**, *9* (11), 927-932.

(87) Wang, Y.; Li, T.; Li, Z.; Wang, S.; Deng, X. Solution-Processed Laminated Perovskite Layers for High-Performance Solar Cells. *Advanced Functional Materials* **2019**, *29* (45), 1903330.

(88) Li, J.; Yuan, X.; Jing, P.; Li, J.; Wei, M.; Hua, J.; Zhao, J.; Tian, L. Temperature-dependent photoluminescence of inorganic perovskite nanocrystal films. *RSC Advances* **2016**, *6* (82), 78311-78316.

(89) de Weerd, C.; Gomez, L.; Zhang, H.; Buma, W. J.; Nedelcu, G.; Kovalenko, M. V.; Gregorkiewicz, T. Energy transfer between inorganic perovskite nanocrystals. *The Journal of Physical Chemistry C* **2016**, *120* (24), 13310-13315.

(90) Davis, N. J.; de la Peña, F. J.; Tabachnyk, M.; Richter, J. M.; Lamboll, R. D.; Booker, E. P.; Wisnivesky Rocca Rivarola, F.; Griffiths, J. T.; Ducati, C.; Menke, S. M. Photon reabsorption in mixed $CsPbCl_3$: $CsPbI_3$ perovskite nanocrystal films for light-emitting diodes. *The Journal of Physical Chemistry C* **2017**, *121* (7), 3790-3796.

(91) Zhang, Z.; Ghimire, S.; Okamoto, T.; Sachith, B. M.; Sobhanan, J.; Subrahmanyam, C.; Biju, V. Mechano-optical modulation of excitons and carrier recombination in self-assembled halide perovskite quantum dots. *ACS Nano* **2022**, *16* (1), 160-168.

(92) Herz, L. M. Charge-carrier dynamics in organic-inorganic metal halide perovskites. *Annual Review of Physical Chemistry* **2016**, *67* (1), 65-89.

(93) Le Corre, V. M.; Duijnstee, E. A.; El Tambouli, O.; Ball, J. M.; Snaith, H. J.; Lim, J.; Koster, L. J. A. Revealing charge carrier mobility and defect densities in metal halide

perovskites via space-charge-limited current measurements. *ACS Energy Letters* **2021**, *6* (3), 1087-1094.

(94) Murali, B.; Kolli, H. K.; Yin, J.; Ketavath, R.; Bakr, O. M.; Mohammed, O. F. Single crystals: the next big wave of perovskite optoelectronics. *ACS Materials Letters* **2019**, *2* (2), 184-214.

(95) Piatkowski, P.; Cohen, B.; Ponseca Jr, C. S.; Salado, M.; Kazim, S.; Ahmad, S.; Sundstrom, V.; Douhal, A. Unraveling charge carriers generation, diffusion, and recombination in formamidinium lead triiodide perovskite polycrystalline thin film. *The Journal of Physical Chemistry Letters* **2016**, *7* (1), 204-210.

(96) Lim, J.; Hörantner, M. T.; Sakai, N.; Ball, J. M.; Mahesh, S.; Noel, N. K.; Lin, Y.-H.; Patel, J. B.; McMeekin, D. P.; Johnston, M. B. Elucidating the long-range charge carrier mobility in metal halide perovskite thin films. *Energy & Environmental Science* **2019**, *12* (1), 169-176.

(97) Chin, X. Y.; Cortecchia, D.; Yin, J.; Bruno, A.; Soci, C. Lead iodide perovskite light-emitting field-effect transistor. *Nature Communications* **2015**, *6* (1), 7383.

(98) Peng, J.; Sun, Y.; Chen, Y.; Yao, Y.; Liang, Z. Light and thermally induced evolutional charge transport in $CH_3NH_3PbI_3$ perovskite solar cells. *ACS Energy Letters* **2016**, *1* (5), 1000-1006.

(99) Zhang, X.; Bi, S.; Zhou, J.; You, S.; Zhou, H.; Zhang, Y.; Tang, Z. Temperature-dependent charge transport in solution-processed perovskite solar cells with tunable trap concentration and charge recombination. *Journal of Materials Chemistry C* **2017**, *5* (36), 9376-9382.

(100) Johnston, M. B.; Herz, L. M. Hybrid perovskites for photovoltaics: charge-carrier recombination, diffusion, and radiative efficiencies. *Accounts of Chemical Research* **2016**, *49* (1), 146-154.

(101) Adhyaksa, G. W.; Veldhuizen, L. W.; Kuang, Y.; Brittman, S.; Schropp, R. E.; Garnett, E. C. Carrier diffusion lengths in hybrid perovskites: processing, composition, aging, and surface passivation effects. *Chemistry of Materials* **2016**, *28* (15), 5259-5263.

(102) Bi, Y.; Hutter, E. M.; Fang, Y.; Dong, Q.; Huang, J.; Savenije, T. J. Charge carrier lifetimes exceeding 15 μs in methylammonium lead iodide single crystals. *The Journal of Physical Chemistry Letters* **2016**, *7* (5), 923-928.

(103) Shrestha, S.; Li, X.; Tsai, H.; Hou, C.-H.; Huang, H.-H.; Ghosh, D.; Shyue, J.-J.; Wang, L.; Tretiak, S.; Ma, X. Long carrier diffusion length in two-dimensional lead halide perovskite single crystals. *Chem* **2022**, *8* (4), 1107-1120.

(104) Akselrod, G. M.; Prins, F.; Poulikakos, L. V.; Lee, E. M.; Weidman, M. C.; Mork, A. J.; Willard, A. P.; Bulović, V.; Tisdale, W. A. Subdiffusive exciton transport in quantum dot solids. *Nano Letters* **2014**, *14* (6), 3556-3562.

(105) Lee, E. M.; Tisdale, W. A. Determination of exciton diffusion length by transient photoluminescence quenching and its application to quantum dot films. *The Journal of Physical Chemistry C* **2015**, *119* (17), 9005-9015.

(106) Giovanni, D.; Righetto, M.; Zhang, Q.; Lim, J. W. M.; Ramesh, S.; Sum, T. C. Origins of the long-range exciton diffusion in perovskite nanocrystal films: photon recycling vs exciton hopping. *Light: Science & Applications* **2021**, *10* (1), 2.

(107) Nair, V. C.; Muthu, C.; Rogach, A. L.; Kohara, R.; Biju, V. Channeling exciton migration into electron transfer in formamidinium lead bromide perovskite nanocrystal/fullerene composites. *Angewandte Chemie* **2017**, *129* (5), 1234-1238.

(108) Ghimire, S.; Nair, V. C.; Muthu, C.; Yuyama, K.-i.; Vacha, M.; Biju, V. Photoinduced photoluminescence enhancement in self-assembled clusters of formamidinium lead bromide perovskite nanocrystals. *Nanoscale* **2019**, *11* (19), 9335-9340.

(109) Shi, T.; Chen, J.; Zheng, J.; Li, X.; Zhou, B.; Cao, H.; Wang, Y. Ti/Au Cathode for Electronic transport material-free organic-inorganic hybrid perovskite solar cells. *Scientific Reports* **2016**, *6* (1), 39132.

(110) Liao, J.-F.; Wu, W.-Q.; Jiang, Y.; Zhong, J.-X.; Wang, L.; Kuang, D.-B. Understanding of carrier dynamics, heterojunction merits and device physics: towards designing efficient carrier transport layer-free perovskite solar cells. *Chemical Society Reviews* **2020**, *49* (2), 354-381.

(111) Wu, W.-Q.; Wang, Q.; Fang, Y.; Shao, Y.; Tang, S.; Deng, Y.; Lu, H.; Liu, Y.; Li, T.; Yang, Z. Molecular doping enabled scalable blading of efficient hole-transport-layer-free perovskite solar cells. *Nature Communications* **2018**, *9* (1), 1-8.

(112) Singh, M.; Ho, I.-H.; Singh, A.; Chan, C.-W.; Yang, J.-W.; Guo, T.-F.; Ahn, H.; Tung, V.; Chu, C. W.; Lu, Y.-J. Unveiling ultrafast carrier extraction in highly efficient 2D/3D bilayer perovskite solar cells. *ACS Photonics* **2022**, *9* (11), 3584-3591.

(113) Wang, J. T.-W.; Wang, Z.; Pathak, S.; Zhang, W.; deQuilettes, D. W.; Wisnivesky-Rocca-Rivarola, F.; Huang, J.; Nayak, P. K.; Patel, J. B.; Yusof, H. A. M. Efficient perovskite solar cells by metal ion doping. *Energy & Environmental Science* **2016**, *9* (9), 2892-2901.

(114) Abdi-Jalebi, M.; Dar, M. I.; Sadhanala, A.; Senanayak, S. P.; Franckevičius, M.; Arora, N.; Hu, Y.; Nazeeruddin, M. K.; Zakeeruddin, S. M.; Grätzel, M. Impact of monovalent cation halide additives on the structural and optoelectronic properties of $CH_3NH_3PbI_3$ perovskite. *Advanced Energy Materials* **2016**, *6* (10), 1502472.

(115) Yin, W.-J.; Shi, T.; Yan, Y. Unusual defect physics in $CH_3NH_3PbI_3$ perovskite solar cell absorber. *Applied Physics Letters* **2014**, *104* (6).

(116) Li, X.; Li, Y.; Feng, Y.; Qi, J.; Shen, J.; Shi, G.; Yang, S.; Yuan, M.; He, T. Strain regulation of mixed-Halide perovskites enables high-performance wide-bandgap photovoltaics. *Advanced Materials* **2024**, 2401103.

(117) Jiang, Q.; Zhao, Y.; Zhang, X.; Yang, X.; Chen, Y.; Chu, Z.; Ye, Q.; Li, X.; Yin, Z.; You, J. Surface passivation of perovskite film for efficient solar cells. *Nature Photonics* **2019**, *13* (7), 460-466.

(118) Liao, J.-F.; Wu, W.-Q.; Zhong, J.-X.; Jiang, Y.; Wang, L.; Kuang, D.-B. Enhanced efficacy of defect passivation and charge extraction for efficient perovskite photovoltaics with a small open circuit voltage loss. *Journal of Materials Chemistry A* **2019**, *7* (15), 9025-9033.

(119) Namatame, M.; Yabusaki, M.; Watanabe, T.; Ogomi, Y.; Hayase, S.; Marumoto, K. Direct observation of dramatically enhanced hole formation in a perovskite-solar-cell material spiro-OMeTAD by Li-TFSI doping. *Applied Physics Letters* **2017**, *110* (12).

(120) Juska, G.; Ranjbar Jahromi, I.; Mattana, F.; Varo, S.; Dimastrodonato, V.; Pelucchi, E. Biexciton initialization by two-photon excitation in site-controlled quantum dots: The complexity of the antibinding state case. *Applied Physics Letters* **2020**, *117* (13).

(121) Fomichev, S.; Burdov, V. Direct biexciton generation in Si nanocrystal by a single photon. *The Journal of Chemical Physics* **2024**, *160* (23).

(122) Beard, M. C.; Knutsen, K. P.; Yu, P.; Luther, J. M.; Song, Q.; Metzger, W. K.; Ellingson, R. J.; Nozik, A. J. Multiple exciton generation in colloidal silicon nanocrystals. *Nano Letters* **2007**, *7* (8), 2506-2512.

(123) McGuire, J. A.; Joo, J.; Pietryga, J. M.; Schaller, R. D.; Klimov, V. I. New aspects of carrier multiplication in semiconductor nanocrystals. *Accounts of Chemical Research* **2008**, *41* (12), 1810-1819.

(124) Klimov, V. I. Mechanisms for photogeneration and recombination of multiexcitons in semiconductor nanocrystals: Implications for lasing and solar energy conversion. *The Journal of Physical Chemistry B* **2006**, *110* (34), 16827-16845.

(125) Chen, Y.; Yin, J.; Wei, Q.; Wang, C.; Wang, X.; Ren, H.; Yu, S. F.; Bakr, O. M.; Mohammed, O. F.; Li, M. Multiple exciton generation in tin–lead halide perovskite nanocrystals for photocurrent quantum efficiency enhancement. *Nature Photonics* **2022**, *16* (7), 485-490.

(126) Villamil Franco, C.; Mahler, B.; Cornaggia, C.; Gustavsson, T.; Cassette, E. Auger recombination and multiple exciton generation in colloidal two-dimensional perovskite nanoplatelets: implications for light-emitting devices. *ACS Applied Nano Materials* **2020**, *4* (1), 558-567.

(127) Kim, H.-S.; Lee, C.-R.; Im, J.-H.; Lee, K.-B.; Moehl, T.; Marchioro, A.; Moon, S.-J.; Humphry-Baker, R.; Yum, J.-H.; Moser, J. E. Lead iodide perovskite sensitized all-solid-state submicron thin film mesoscopic solar cell with efficiency exceeding 9%. *Scientific Reports* **2012**, *2* (1), 591.

(128) Noh, M. F. M.; Teh, C. H.; Daik, R.; Lim, E. L.; Yap, C. C.; Ibrahim, M. A.; Ludin, N. A.; bin Mohd Yusoff, A. R.; Jang, J.; Teridi, M. A. M. The architecture of the electron transport layer for a perovskite solar cell. *Journal of Materials Chemistry C* **2018**, *6* (4), 682-712.

(129) Mahmood, K.; Sarwar, S.; Mehran, M. T. Current status of electron transport layers in perovskite solar cells: materials and properties. *Rsc Advances* **2017**, *7* (28), 17044-17062.

(130) Ochsenbein, S. T.; Krieg, F.; Shynkarenko, Y.; Rainò, G.; Kovalenko, M. V. Engineering color-stable blue light-emitting diodes with lead halide perovskite nanocrystals. *ACS Applied Materials & Interfaces* **2019**, *11* (24), 21655-21660.

(131) Lin, K.; Xing, J.; Quan, L. N.; de Arquer, F. P. G.; Gong, X.; Lu, J.; Xie, L.; Zhao, W.; Zhang, D.; Yan, C. Perovskite light-emitting diodes with external quantum efficiency exceeding 20 per cent. *Nature* **2018**, *562* (7726), 245-248.

(132) Xu, W.; Hu, Q.; Bai, S.; Bao, C.; Miao, Y.; Yuan, Z.; Borzda, T.; Barker, A. J.; Tyukalova, E.; Hu, Z. Rational molecular passivation for high-performance perovskite light-emitting diodes. *Nature Photonics* **2019**, *13* (6), 418-424.

(133) Pandey, P. *New findings open opportunities beyond conventional LED technologies for Infrared Perovskite LEDs*. University of Cambridge, Cavendish Laboratory, 2023. https://www.phy.cam.ac.uk/news/new-findings-open-opportunities-beyond-conventional-led-technologies-infrared-perovskite-leds (accessed 2025 10th January).

(134) Ma, D.; Lin, K.; Dong, Y.; Choubisa, H.; Proppe, A. H.; Wu, D.; Wang, Y.-K.; Chen, B.; Li, P.; Fan, J. Z. Distribution control enables efficient reduced-dimensional perovskite LEDs. *Nature* **2021**, *599* (7886), 594-598.

(135) Yakunin, S.; Protesescu, L.; Krieg, F.; Bodnarchuk, M. I.; Nedelcu, G.; Humer, M.; De Luca, G.; Fiebig, M.; Heiss, W.; Kovalenko, M. V. Low-threshold amplified spontaneous emission and lasing from colloidal nanocrystals of caesium lead halide perovskites. *Nature Communications* **2015**, *6* (1), 8056.

Chapter 2

Experimental

Abstract

This chapter outlines the various materials and experimental methods employed in my research. I detailed the synthesis procedures for lead halide perovskites (LHPs) and the characterization techniques used, including an explanation of their fundamental principles. It also includes the multiwall carbon nanotube (MWCNT) functionalization procedure, and instrumentation used for investigating the conjugates. I synthesized LHP quantum dots (PQDs) and nanocrystals (PNCs) using the hot injection method. UV-visible absorption spectroscopy was employed to measure the absorption and steady-state fluorescence spectroscopy was employed to measure the emission characteristics of the synthesized halide perovskites. X-ray diffraction (XRD) was employed to determine the crystal structure of the perovskites. Small-angle X-ray scattering (SAXS) provided insights into interparticle distances during assembly formation. On the other hand, the functionalization of MWCNT was investigated using X-ray photoelectron spectroscopy (XPS), Fourier transform infrared spectroscopy (FTIR), and Raman spectroscopy. The size and shape of PQDs, PNCs, and MWCNTs as well as their conjugates were determined by scanning transmission electron microscopy (STEM). Moreover, STEM coupled with energy-dispersive X-ray spectroscopy (EDX) was used to determine the composition of PNCs. The fluorescence blinking of individual PNCs and PQDs was investigated through single-particle microscopy. To assess carrier lifetime, photoluminescence (PL) decays were analyzed using time-correlated single-photon counting (TCSPC) techniques, utilizing ultrafast pulsed laser systems operating in the picosecond (ps) and femtosecond (fs) ranges. Additionally, I employed Quantaurus-Tau for PL lifetime measurement where LEDs were used as excitation sources to measure the carrier lifetime. These techniques helped me to understand charge carrier recombination in the samples. For exploring excited-state carrier dynamics and carrier transfer, I used transient absorption spectroscopy with a 400 nm fs pulse laser as the pump and a white light continuum as the probe.

2.1 Materials

The following chemicals and materials were used in this research without any further purification:

Formamidine hydrobromide (FABr, TCI, >98.0%), cesium acetate (CH_3COOCs, Sigma-Aldrich, 99.9%), lead (II) bromide ($PbBr_2$, Sigma-Aldrich, ≥98%), hexadecyl amine ($C_{16}H_{35}N$, TCI, >95.0%), n-octylamine hydrobromide (TCI, >98.0%), oleic acid (TCI, >85.0%), polybutadiene (PBD, Sigma-Aldrich, average Mw ~200,000), multiwall-carbon nanotube (Sigma–Aldrich, >90% carbon basis, D×L = 110-170 nm ×5-9 μm), 4-nitrobenzediazonium tetrafluoroborate (TCI, >98.0%), cresyl violet perchlorate (Sigma-Aldrich), sodium borohydride, dehydrated N, N-dimethylformamide (DMF, Fujifilm Wako), potassium bromide [KBr, crystallized from the HBr (Fujifilm Wako, 47.0–49.0%) + KOH (Fujifilm Wako, 85%) reaction in ice-cold water], dimethyl sulfoxide (DMSO**,** Fujiifilm Wako), sodium bromide (NaBr, Fujifilm Wako, 99.5%), rhodamine B (Fujiifilm Wako), cesium bromide (CsBr, TCI, >99.0%), coumarin 120 (TCI, 98%), coumarin 6 (Sigma-Aldrich, 98%), fluorescein sodium salt (Sigma-Aldrich), 1-octadecene (TCI, >90.0%), 1-hexadecene (TCI, 98%), acetone (Fujifilm Wako, ≥99.5%), hexane (Fujifilm Wako, >96.0%), toluene (Fujifilm Wako, ≥99.5%), dimethyl sulfoxide, acetonitrile (Fujifilm Wako, ≥99.5%), $(NH_4)_2CO_3$ (Fujiifilm Wako), HCl (Fujiifilm Wako, 35-37%), HBr (Fujiifilm Wako, 47-49%**)**, tetrahydrofuran (THF, Fujifilm Wako, 99.5%), and distilled water (Fujifilm Wako).

2.2 Sample preparation

2.2.1 Preparation of PQDs and PNCs

Preparation of $FAPbBr_3$ PQDs

$FAPbBr_3$ PQDs were synthesized by following a hot injection method with some modifications.[1] 25 mg FABr (0.2 mmol) and 73.4 mg $PbBr_2$ (0.2 mmol) were solubilized in 400 μL dry DMF to prepare a precursor solution. In a separate three-neck flask, 25.2 mg (0.12 mmol) n-octylammonium bromide, 200 μL (0.63 mmol) oleic acid, and 1-octadecene (4 mL) were taken and mixed well to prepare a ligand solution. The ligand solution was vacuumed for 15 minutes to remove dissolved moisture and air. The temperature was raised to 80 °C while maintaining an argon flow and the mixture was stirred continuously for 10 minutes. Afterward, 400 μL precursor solution was incorporated into the flask containing ligand solution. Then, acetone and hexane mixture (1:1 v/v) was added under vigorous stirring, and the reaction vessel was rapidly transferred to the ice water bath to stop the perovskite overgrowth. Next, 100 μL of the synthesized PQD solution was diluted with 3 mL of toluene while stirring vigorously.

The resulting PQD dispersion was centrifuged at 14,500 rpm for 5 minutes, and the DMF-containing supernatant was discarded. The PPT was then redispersed in toluene and used for further experiments. Figure 2.1 presents a schematic of the synthesis procedure of $FAPbBr_3$ PQDs.

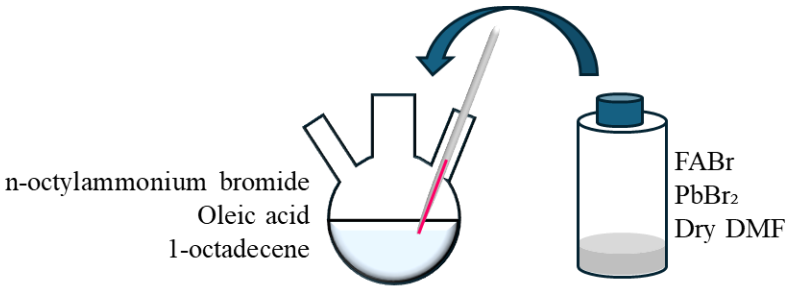

Figure 2.1. A scheme of the synthesis of $FAPbBr_3$ PQDs.

Preparation of $CsPbBr_3$ PNCs

Using the hot injection method, I synthesized the $CsPbBr_3$ PNCs (Figure 2.2).[2, 3] In a three-neck conical flask, 420 mg (1.1 mmol) of $PbBr_2$, 3.2 mL (10 mmol) of oleic acid, 2.4 g (10 mmol) of hexadecyl amine, and 50 mL of 1-hexadecene were taken and heated at 120 °C under vacuum condition for 1 hour. Simultaneously, in another three-necked flask, 30 mg (0.15 mmol) of cesium acetate, 1.2 mL of 1-hexadecene, and 180 µL (0.5 mmol) of oleic acid were taken and heated at 120 °C under reduced pressure for 1 hour. Once all the precursors had been fully dissolved, argon gas was introduced, and the temperature was increased to 170 °C. At 170 °C, the cesium acetate precursor solution was rapidly injected into the lead precursor solution, causing an immediate color change to greenish yellow. The mixture was then quickly cooled in an ice-water bath to stop the reaction and prevent further growth of the NCs.

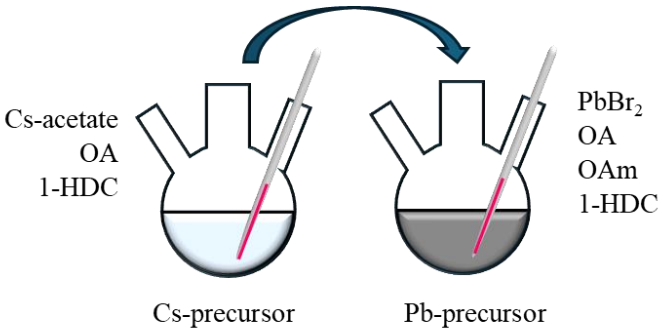

Figure 2.2. A scheme of the synthesis of $CsPbBr_3$ PNCs.

Afterward, the as-synthesized PNC colloid in 1-hexadecene was mixed with 50 mL of toluene and centrifuged at 14,500 rpm for 30 minutes. The resulting PPT was dispersed in

toluene. To isolate the small, uniform-sized PNCs, the mixture was centrifuged again at 3,000 rpm for 5 minutes, and the larger particles in the precipitate were discarded. The purified sample was then used for further analysis.

2.2.2 Functionalization of MWCNTs

1 g of 4-Nitrobenzediazonium tetrafluoroborate (NBDTFB) was added to the 100 mg of MWCNTs in a vial. They were mixed very well by shaking and later using a motor and pastel. After confirming uniform mixing, the mixture was heated to 150 °C, leading to the decomposition of NBDTFB and the formation of free radicals (Figure 2.3).[4] These free radicals are very unstable and react with the surface of the MWCNT very quickly.[5, 6] The crude product was dispersed in acetonitrile, subjected to sonication, and centrifuged. The washing procedure continued until the acetonitrile turned colorless. The resulting pure nitrobenzene functionalized MWCNT (MWCNT-NO_2) was dried under a high vacuum.

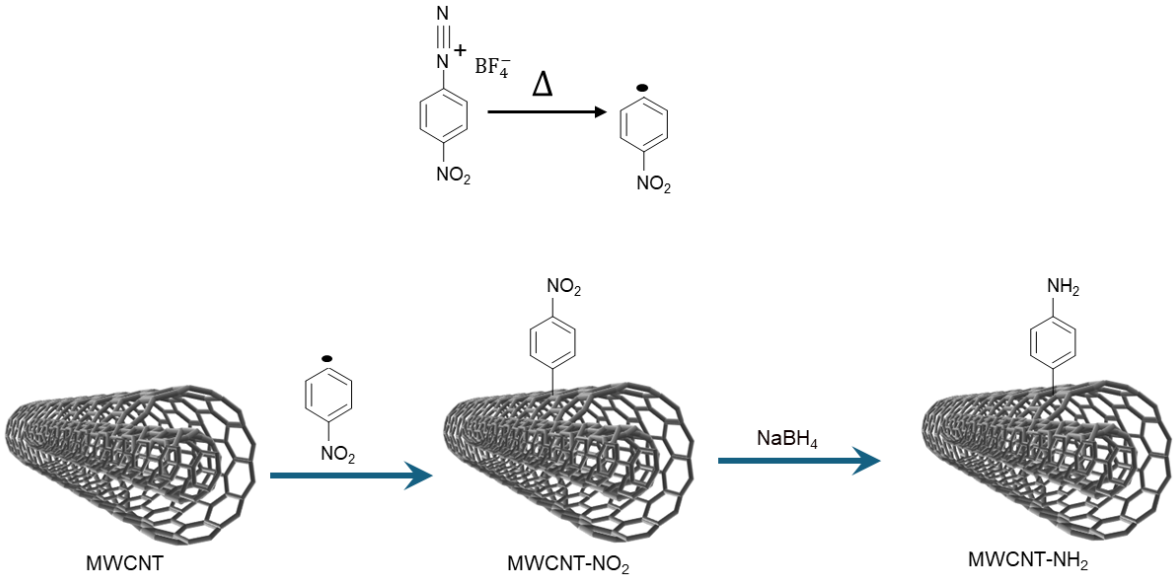

Figure 2.3. Representation of the chemical reaction taking place on the MWCNT surface during the functionalization with a terminal phenylamine group.

The obtained MWCNT-NO_2 was dispersed in 10 mL of dimethyl sulfoxide (DMSO) in a vial. Then sodium borohydride ($NaBH_4$) was added to an excess amount to the vial under vigorous stirring at 100 °C. The reaction was accelerated by adding a small amount (200 µL) of water. $NaBH_4$ reduced the -NO_2 groups of MWCNT-NO_2 to -NH_2 groups.[7] The reaction progress was tracked by observing the generation of hydrogen bubbles in the DMSO. The reaction continued for 24 hours. The crude phenylamine functionalized MWCNT (MWCNT-NH_2) was washed with acidic water to remove any unreacted $NaBH_4$. It was then rinsed

multiple times with pure water until the pH reached neutral. The pH was adjusted to slightly basic by adding ammonium carbonate ($(NH_4)_2CO_3$) to deprotonate the MWCNT-NH_3^+ groups. Finally, the MWCNT-NH_2 was properly dried. This sample was used for characterization and conjugate formation.

2.2.3 Preparation of PQD assemblies and PNC-MWCNT conjugates

Preparation of $FAPbBr_3$ PQD and polybutadiene film (PQD-PBD film)

PQD-PBD film was fabricated using the drop-casting method. 25 mg/mL PBD and the $FAPbBr_3$ PQD solution (10 mg/mL) in toluene were mixed well by shaking. The uniform mixing was confirmed by sonicating for 5 minutes. A 5 µL portion of the mixture was placed onto a glass coverslip (25×50 mm^2). Then the film was dried very well.

Preparation of $CsPbBr_3$ PNCs and MWCNT conjugates (PNC-MWCNT) via post-mixing method

MWCNT-NH_2 was converted to MWCNT-$NH_3^+Br^-$ before assembly formation by treatment with dilute HBr. MWCNT-NH_3^+ Br^- was dried properly under a high vacuum. It was then mixed with dilute $CsPbBr_3$ PNCs in the toluene-THF (9:1 v/v) mixture. THF was used to decrease the aggregation of MWCNT. After 2 days, the sedimented MWCNT-PNC was collected and the upper solvent was discarded. The collected sample was washed with the same ratio of toluene-THF mixture to remove excess unattached PNC from the surface of MWCNT. The scheme is presented in Figure 2.4.

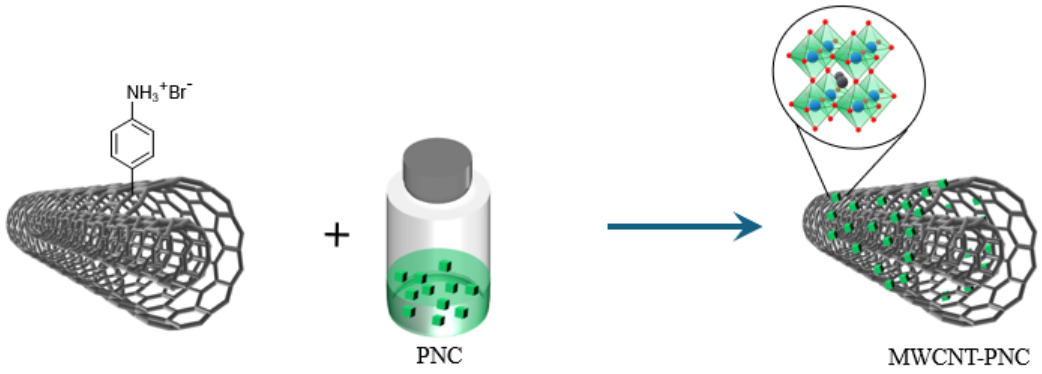

Figure 2.4. MWCNT-PNC conjugate formation by the post-mixing method.

Preparation of $CsPbBr_3$ PNCs and MWCNT conjugates (PNC-MWCNT) via in-situ hot injection method

In-situ PNC-MWCNT conjugates are prepared following the hot injection synthesis procedure of $CsPbBr_3$ PNCs with little modifications. My method is similar but not the same as the already reported method of preparing these types of assembly of PNC around CNT.[8]

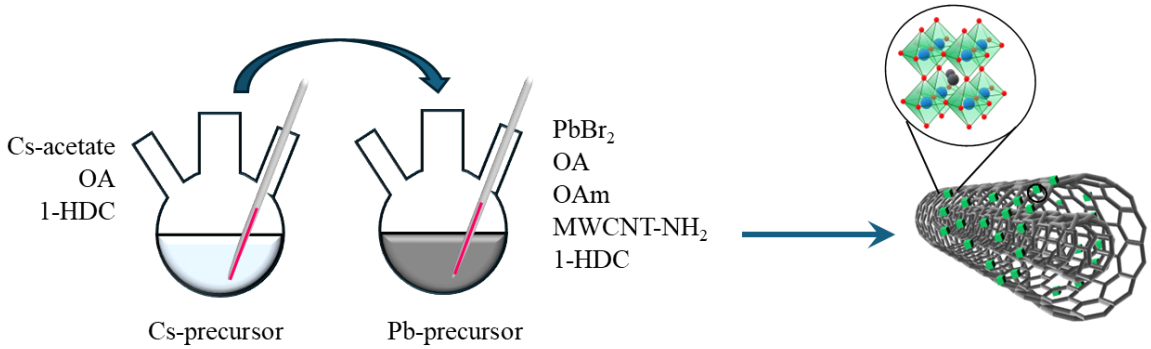

Figure 2.5. MWCNT-PNC conjugate formation by in-situ hot injection method.

Here, in a three-neck flask, 420 mg of $PbBr_2$, 3.2 mL of oleic acid, 2.4 g of hexadecyl amine, and 35 mL of 1-hexadecene were added. 5 mg of MWCNT-NH_2 was sonicated with 15 mL of 1-hexadecene for 15 mins and then added to this flask. In another three-neck conical flask, 30 mg of cesium acetate, 1.2 mL of 1-hexadecene, and 180 µL of oleic acid were added. Both of the flasks were heated at 120 °C under high vacuum for 1 hour. After stopping the vacuum, argon was flashed inside the flasks, and the temperature was increased to 170 °C. Then all the Cs-precursor solution was injected into the Pb-precursor flask. Immediately the color changes to yellowish green. The reaction mixture was cooled using an ice bath, and the conjugates were harvested by centrifugation at 1000 rpm for 3 mins. Then conjugates were redispersed in toluene. This sample was used for further experiments. The scheme is presented in Figure 2.5.

2.2.4 Preparation of samples for single-particle and time-resolved spectroscopy studies

The drop-and-drag method was used to obtain the $CsPbBr_3$ PNC single particle distribution on a coverslip. The distribution of PNCs was confirmed through single-particle microscopy. After confirmation, the sample's lifetime and PL blinking were measured. Films for measuring the PL lifetime of PNC-MWCNT conjugates and PNC films were prepared by dropping the samples on a glass coverslip and drying them properly.

2.3 Methods

2.3.1 UV-vis absorption spectroscopy

The ultraviolet-visible or UV-vis absorption spectra of $FAPbBr_3$ PQDs, $CsPbBr_3$ PNCs, and conjugates were measured using a UV-Vis spectrophotometer (Evaluation 220, Thermo Fisher Scientific). A typical schematic of a UV-vis absorption spectrophotometer is presented in Figure 2.6. This method primarily assesses the quantity of light absorbed or passed through the sample. A light source provides a continuous spectrum of light covering both UV and visible regions. The light travels through the monochromator (prism or diffraction grating) and

separates it into different wavelengths. The desired wavelength of light that will be passed through the sample can be selected by adjusting the monochromator. Molecules in the sample absorb specific wavelengths of light.

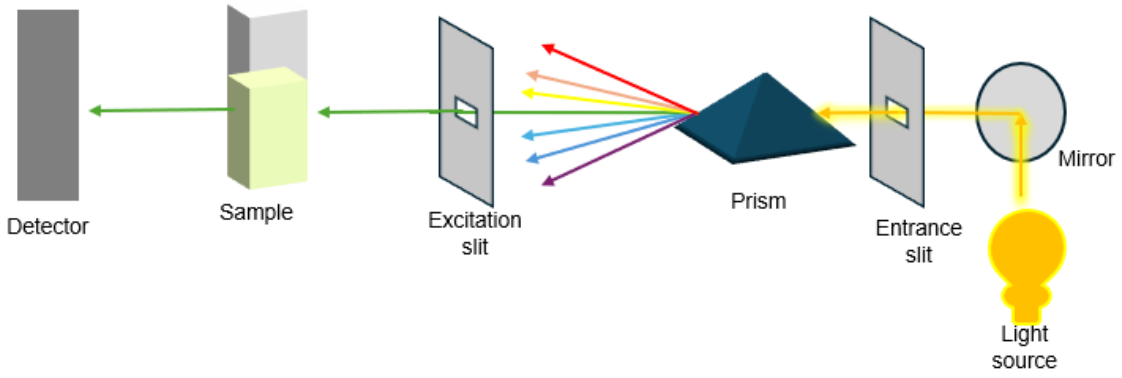

Figure 2.6. Schematic representation of a typical UV-vis absorption spectroscopy.

Based on their electronic transitions, a reduction in the strength of the incident light occurs. The transmitted light that emerges from the sample is detected by a photodetector (e.g., photomultiplier tube or photodiode). The detector measures the intensity of the transmitted light and transforms it into an electrical signal. The instrument compares the light's intensity before and after it travels through the sample. The difference in intensity is used to calculate the absorbance of the sample. From the absorption spectra, I can identify the sample and measure its concentration following the Beer-Lambert Law. According to this law, absorbance (A) is directly proportional to both the concentration (c) of the absorbing substance and the optical path (l) through which the light travels.

$$A=\varepsilon cl$$

Here, ε is the molar absorptivity or molar extinction coefficient, which quantifies the extent to which a substance absorbs light at a specific wavelength.

Anyway, when a molecule absorbs or emits light, it undergoes a transition between various electronic states. The electronic states and the vibrational energy levels involved with the electronic states play a role in the transition (Figure 2.7). The intensity and likelihood of electronic transitions (e.g., during absorption or emission of light) in molecules can be explained by the Franck-Condon Principle.

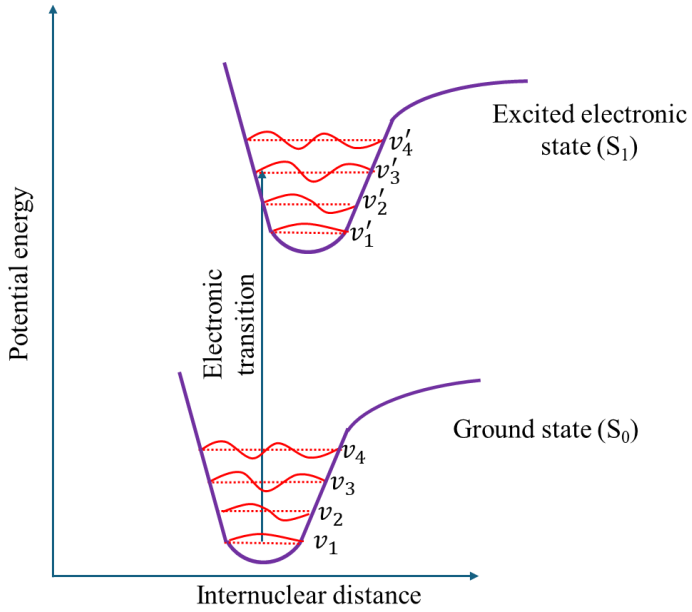

Figure 2.7. Different electronic states of a molecule with probable transition.

When a molecule absorbs or emits light, electrons rearrange almost instantaneously, while the nuclei (protons and neutrons in the atoms) move much more slowly. This is because nuclei have significantly greater mass compared to electrons. Due to the slower movement of the nuclei, electronic transitions occur "vertically" on a potential energy diagram. This means that when an electron jumps from one energy state to another, the nuclei do not have time to adjust during the transition. Thus, the transition happens at a fixed nuclear configuration. The likelihood of a transition is dependent on the overlap of the vibrational wavefunctions in the initial and final electronic states. These overlaps are known as Frank-Condon factors. The greater the overlap, the more probable the transition. Like in Figure 2.7 the position of excited states slightly changes from the ground state. Here the most probable transition is from v_1 to v'_3.

2.3.2 Steady-state fluorescence spectroscopy

Steady-state fluorescence spectroscopy is a powerful technique for studying the PL properties of materials and molecules. PL spectra give us insight into excitonic relaxation. I measured the PL spectra of my samples using a fluorescence spectrometer (F-4500, Hitachi). The scheme of the spectrometer is presented in Figure 2.8.

In this instrument, the light emitted from the source goes through an excitation monochromator or filter to select the specific wavelength needed to excite the sample. The selected excitation light is directed toward the sample holder or cuvette, which contains the perovskite colloidal samples. The sample is usually placed at a 90° angle to the excitation light

path to minimize the detection of the excitation light and ensure that only the emitted fluorescence is collected. The fluorescence signal is then directed to the detector. When a compound absorbs light, it gains energy and is transferred from its ground electronic state (S_0) to the excited electronic state (S_1 or higher). The energy of the absorbed photon must match the energy difference between the molecule's ground state and its excited state. Kasha's rule states that fluorescence emission almost always takes place from the lowest excited singlet

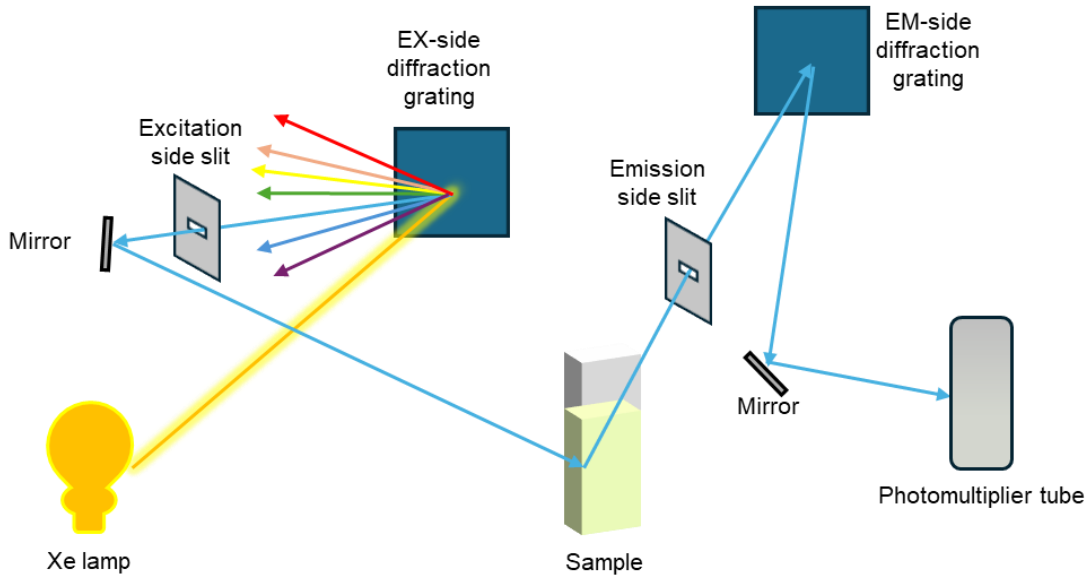

Figure 2.8. Schematic representation of a typical steady-state fluorescence spectroscopy.

state (S_1), regardless of which higher excited state (S_2, S_3, etc.) was initially populated upon photon absorption. As a result, following excitation, the molecule rapidly releases excess energy as heat and relaxes back to the first excited electronic state's (S_1) lowest vibrational level. This process occurs through internal conversion or non-radiative relaxation by electron-phonon coupling, where excess energy is dissipated as heat. This intra-band relaxation happens within a very short period (femtosecond and picosecond level). Once the molecule returns to the lowest vibrational level of the S_1 level, it can go back to the S_0 state by releasing a photon. The emitted photon typically has lower energy than the absorbed photon because of energy loss during vibrational relaxation. This difference in absorption and emission energy is known as the Stokes shift. If there is an intersystem crossing, the photon is emitted as a phosphorescence. All the possible transitions after the excitation of the charge carrier are presented in Figure 2.9 (Jablonski Diagram). The PL quantum yield (QY) refers to the ratio of emitted photons and absorbed photons, while the PL lifetime is the average duration a compound remains excited before emitting a photon.

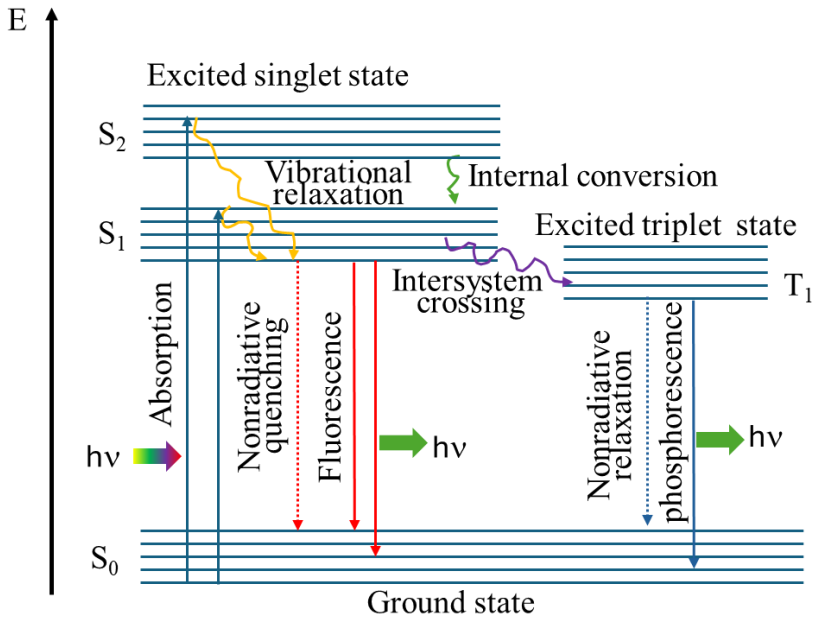

Figure 2.9. A simplified Jablonski Diagram.

2.3.3 Time-resolved photoluminescence spectroscopy

Femtosecond lifetime measurement system

I used femtosecond PL lifetime measurement systems for monitoring the exciton dynamics in $FAPbBr_3$ PQDs film and PQD-PBD assembly. This machine is used to measure ultrafast carrier relaxation dynamics that occur on the femtosecond (10^{-15} seconds) timescale. The mechanism behind such systems relies on generating and detecting very short laser pulses and monitoring the fate of photogenerated charge carriers after excitation. The instrumentation of this system is presented in Figure 2.10. The perovskite samples were irradiated with a 405 nm pulse laser having a pulse width of 150 fs and frequency of 200kHz. This 405 nm laser is generated by a series of events. First, A mode-locked Ti: sapphire oscillator (Mira 900) generates 800 nm 76 MHz femtosecond seed pulses through Kerr-lens mode-locking. This light is sent to the amplifier (Rega 9000) where it converts to 800 nm, 200 kHz, and 150 fs laser. This laser is then introduced to the optical parametric amplifier (OPA 9400) where it goes through the second harmonic generation (SHG) crystal. SHG is a nonlinear optical process that takes place in a nonlinear crystal. When two photons with identical frequencies merge, they combine to create a new photon that possesses double the energy of the individual photons. This process results in a photon with half the original wavelength. This laser is then split into two parts: one part goes to the digital delay via photodiode and another to the sample via a series of optics.

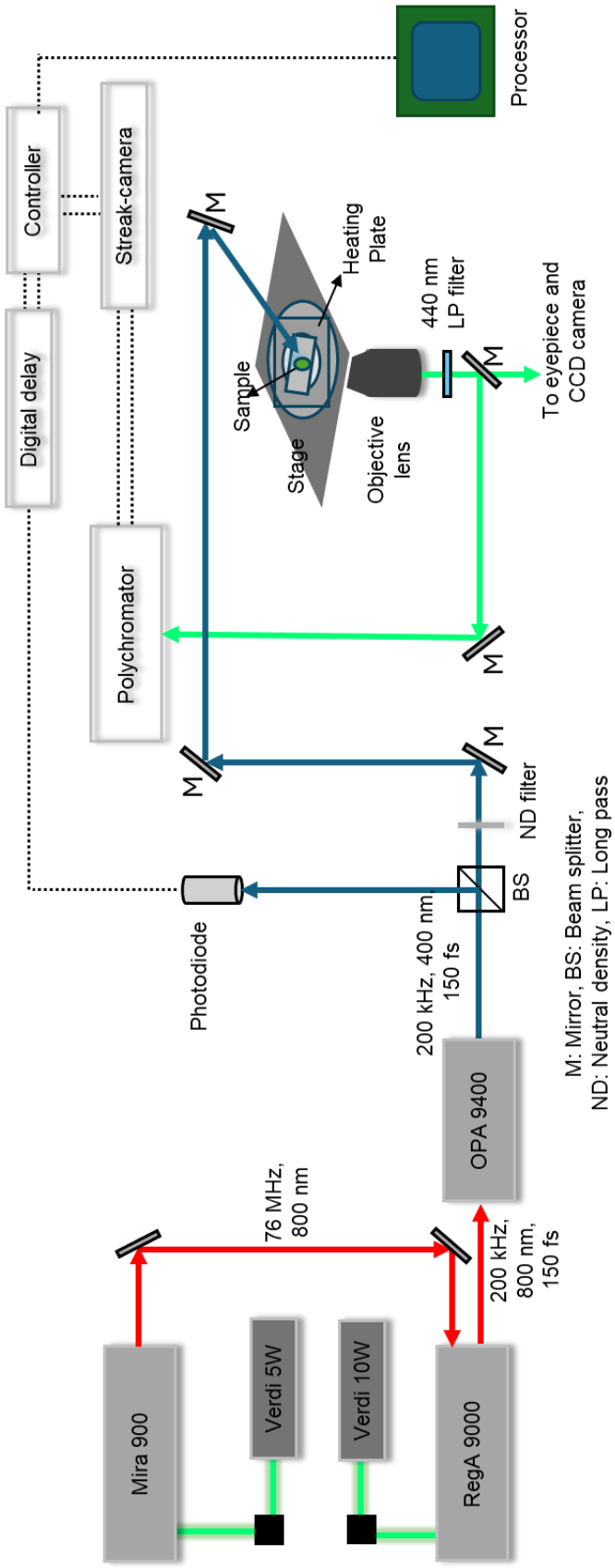

Figure 2.10. Optical setup for time-resolved PL studies using an ultrafast femtosecond laser.

Here I used a heating plate for heating the PQD-PBD assembly. The emission goes through the objective lens (Olympus) and is detected by the streak camera. The computer then processes both excitation and emission signals. The PL decay curves obtained were fitted by the following equation-

$$\tau_{average} = \frac{a_1\tau_1 + a_2\tau_2 + a_3\tau_3 + \ldots\ldots}{a_1 + a_2 + a_3 + \ldots\ldots}$$

Here, τ is the lifetime component and a is the amplitude. The short PL lifetime component is because of the nonradiative recombination which is mainly contributed by the traps. Traps are localized states in the material where charge carriers (electrons or holes) can become temporarily trapped. When an electron recombines with a hole via a trap, the recombination does not result in the emission of a photon, but instead, the energy is released as heat through interactions with the lattice (phonon emission). These traps often arise due to defects, impurities, or surface states within the material. The longest component is because of the radiative recombination where the energy is released as a photon (light). The $\tau_{average}$ is the average time a charge carrier stays excited.

Picosecond lifetime measurement system

I used the picosecond lifetime measurement system to measure the PL lifetime of $CsPbBr_3$ single particles, PNC-MWCNT conjugates, and $CsPbBr_3$ PNC film. This setup is designed to measure the carrier lifetime in the picosecond (10^{-12} seconds) range. The whole arrangement is represented in Figure 2.11. The 405 nm pulse laser is generated from a PicoQuant GmbH picosecond laser diode. Laser frequency 1MHz was used. The pulse width is <50 ps. Neutral density filters were employed to regulate the intensity of the laser. This laser goes through different optics, and ultimately through the objective lens where it illuminates the sample. I prepared my samples on a glass cover slip and placed them on the stage. I used the pinhole on the irradiation side in every measurement to irradiate only a small selected area. On the emission side, I used a 480 nm long pass filter to cut the laser. The emission goes to the avalanche photodiode (SPCM-AQR, PerkinElmer) and TCSPC system (SPC-830, Becker and Hickl GmBH) for counting photons. The resulting histogram on the screen provides a temporal decay curve of the emitted photons. This decay curve is analyzed to extract information such as fluorescence lifetimes, which indicate carrier dynamic processes within the sample. The acquired PL decay curves were analyzed using a triexponential fitting approach, applying the same equation used for the femtosecond laser system.

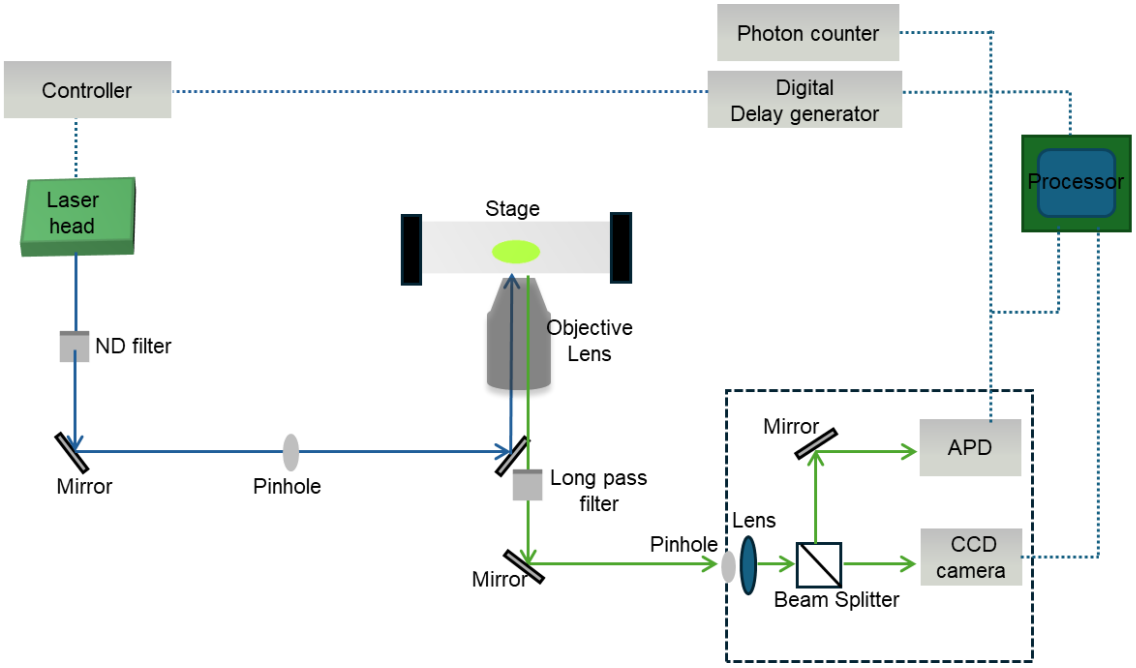

Figure 2.11. Optical setup for time-resolved PL studies using a picosecond laser system.

Transient absorption spectroscopy

Transient absorption spectroscopy of my $CsPbBr_3$ PNC and conjugates were measured using an ultrafast femtosecond pump and probe system. Mode-locked Ti: sapphire (Solstice, Spectra-Physics, Milpitas, CA) generates an 800 nm laser (1 kHz repetition rate and 150 fs pulse width). The laser is then fed into an amplifier, where its energy is boosted. The 800 nm pulse laser then goes to the OPA (optical parameter amplifier) where it is converted to the 400 passing through the BBO crystal. This crystal works via a second harmonic generation. The probe light is produced by directing signal light from an optical parametric amplifier (TOPAS, Light Conversion Ltd., centered at 1.6 μm) onto a CaF_2 plate. The probe light is detected using a complementary metal-oxide-semiconductor detector (PMA-20, Hamamatsu Photonics, Shizuoka, Japan). The typical setup of the pump-probe system is given in Figure 2.12.

For t<0, the probe pulse arrives and measures the initial absorption (A_0) of the LHP samples. At t=0, the pump pulse excites the sample, promoting a significant number of ground-state (S_0) electrons to the excited state (S_1). When t>0, the probe pulse again measures the absorption (A_t) which is less than A_0. Therefore, absorption change $\Delta A = A_t - A_0$. These absorbance changes at each wavelength are recorded for various time delays. The result is a 2D dataset showing how ΔA evolves over time and across the spectral range (Figure 2.12b).

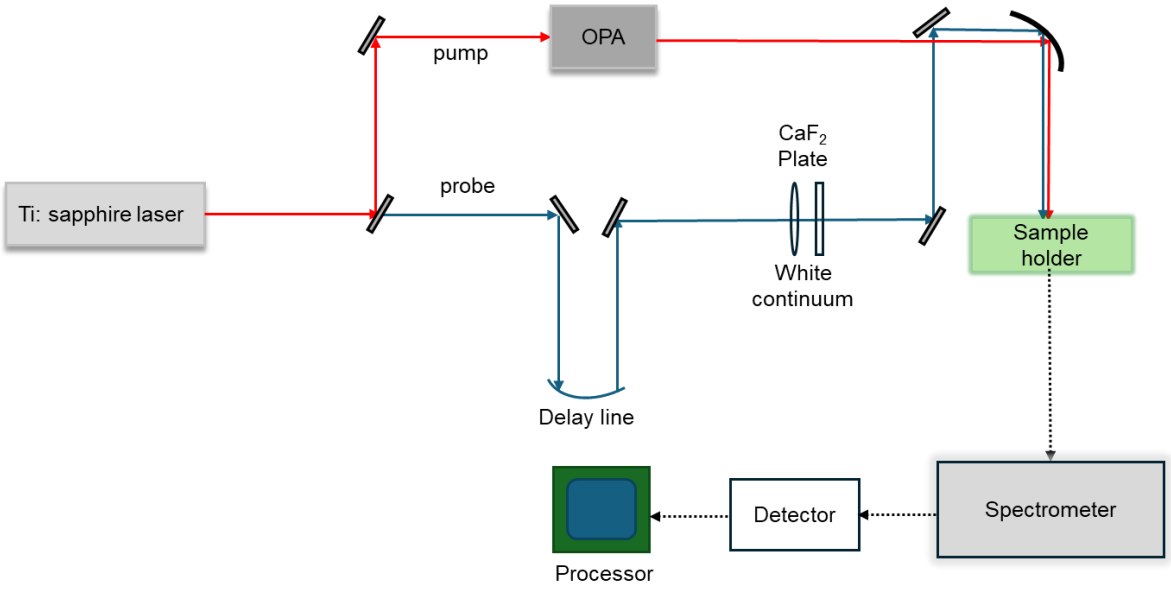

Figure 2.12. Optical setup for transient absorption studies using a pump-probe system.

Ground state bleach (GBS) peak appeared because of the decrease in absorption of ground state. When the pump pulse excites electrons from the ground state to an excited state, fewer molecules are available to absorb photons at the wavelength corresponding to the ground-state absorption. This depletion appears as a negative signal spectrum. Photo-induced absorption (PIA) peak arises from excited-state absorption, where excited electrons in higher

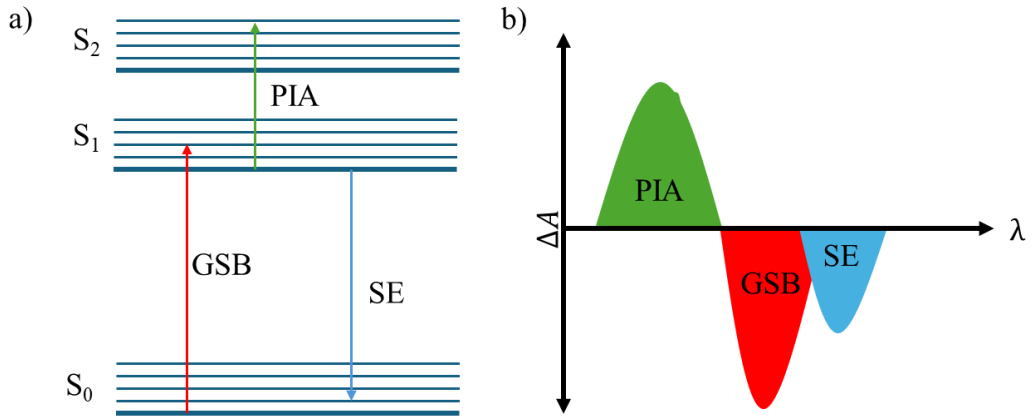

Figure 2.13. a) The different possible transitions of the carriers recorded by a pump-probe system after getting photoexcited. b) A typical spectrum generated by a pump-probe system.

energy states absorb additional photons, promoting them to even higher states. This is a positive signal in the spectrum. The excited molecules can relax by emitting photons spontaneously (spontaneous emission). This process occurs randomly and is independent of external electromagnetic fields. Sometimes, stimulated emission (SE) occurs when the incident photon from the probe pulse induces an excited molecule to emit a photon of the same energy, phase,

and direction as the probe pulse photon. SE is a negative signal because the emitted photons amplify the probe pulse, effectively reducing the net absorbance. Using this system, excited carrier dynamics as well as charge transfer and energy transfer can be predicted.

2.3.4 Single-particle spectroscopy

A single-particle microscope allows the visualization and analysis of individual particles at the nanoscale. I used this system to measure the PL blinking properties of $CsPbBr_3$ PNCs single dots. The setup of a single particle microscope is presented in Figure 2.14a. 400 nm CW laser generated from the laser head goes through different optics and illuminates the sample. The main part of this system is the Electron-Multiplying Charge-Coupled Device (EMCCD) camera. EMCCDs are built on the traditional CCD architecture, consisting of a sensor chip (Figure 2.14b) with an array of light-sensitive pixels that convert incoming photons into charge. Each

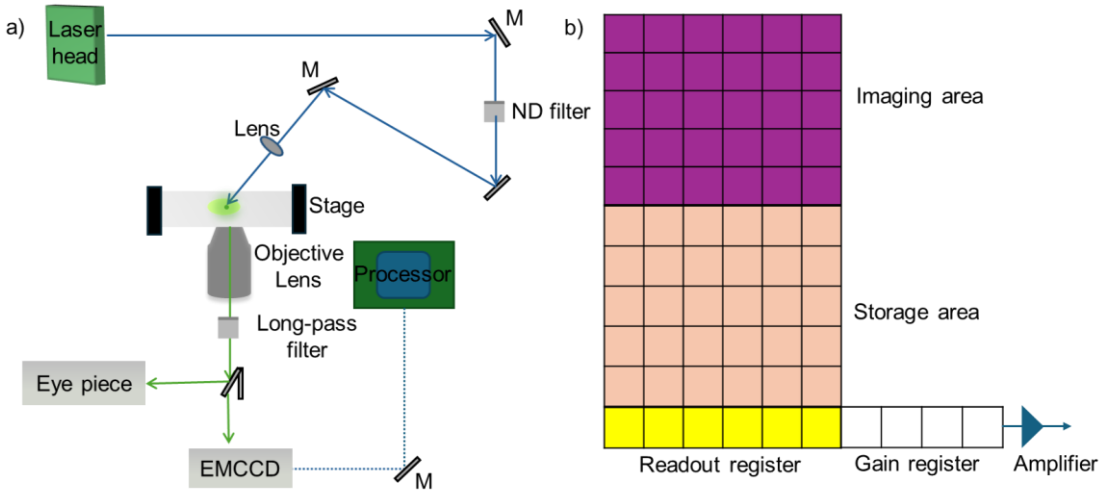

Figure 2.14. Optical setup of a single-particle microscopy system (a) and structure of an EMCCD sensor chip (b).

pixel accumulates a charge based on the number of photons detected. This chip has a series of charge transfer channels that allow for the movement of the generated charge from one pixel to another. The gain register of EMCCD is responsible for the electron multiplication process. Once the charge has been multiplied, it is transferred to the output node, where the charge is converted into a voltage signal that can be digitized and read out. EMCCD is equipped with a cooling mechanism (typically around -80 °C) to minimize thermal noise.

Quantaurus-tau

Quantaurus-tau (Hamamatsu, C11367 series) was used to measure the PL lifetime of $CsPbBr_3$ PNC in the colloidal state. Among the different LED excitation wavelengths available, I used

365 nm LED excitation. The obtained decay curves were fitted triexponentially using the instrument software.

2.3.5 XRD and SAXS

XRD is a method for analyzing the structure of crystalline materials. When X-ray is focused on a crystalline sample, it is scattered by the atoms in the crystal lattice. The constructive interference of these scattered X-rays leads to a pattern that can be analyzed to assess various characteristics of the material. I measured the XRD of my PNCs and PQDs to understand the crystal structure of them. The fundamental equation governing XRD is Bragg's Law, which relates the wavelength of the incident X-rays to the angles at which they are diffracted by the crystal planes. It is expressed as:

$$n\lambda = 2dsin(\theta)$$

Where, n = Order of diffraction, λ = X-ray wavelength, d = Distance between crystal planes, and θ = Diffraction angle.

SAXS provides critical information about the size, shape, and arrangement of particles or domains of the LHP assembly/film. The interparticle distance d (Bragg distance or center-to-center distance) within the film can be calculated from the position of the peak q, using the following equation:

$$d = \frac{2\pi}{q}$$

Both XRD and SAXS of my PQDs and PQD-polymer assembly were measured using a SmartLab X-ray diffractometer (RIGAKU), equipped with a copper Kα (λ = 0.15406 nm) X-ray source. For the XRD analysis, samples were put on glass slides, while for the SAXS measurements, Kapton films were first attached to the glass. LHP samples were drop casted on that film.

2.3.6 XPS

XPS of my functionalized multiwall carbon nanotubes was measured to examine the elemental composition and chemical states. It helped me to confirm successful functionalization. XPS operates on the principle of the photoelectric effect, where X-rays are employed to eject electrons from the surface of the material. When X-rays are directed at a sample, they impart energy to core-level electrons, causing them to be emitted from the material. The kinetic energy

of the emitted photoelectrons is measured. The binding energy of the electrons can then be calculated using the following equation:

$$EB = hv - Ek - \varphi$$

Where: EB= Binding energy of the electron, hv= Energy of the incident X-ray photon, Ek= Kinetic energy of the emitted electron, and φ = Work function of the spectrometer.

The binding energy values are characteristic of the specific elements and their chemical states present. The relative intensity of the peaks corresponding to different elements allows for the quantification of their presence, while the chemical shifts in these peaks provide insight into the oxidation states and bonding environments of the elements. By examining the peak intensities and position in the XPS spectrum, I was able to ascertain the elemental composition and identify the chemical states of the species present on the surface of the MWCNT.

2.3.7 FTIR

For the characterization of the functionalization of MWCNT, FTIR was also measured. It provides valuable information about the molecular structure, functional groups, and chemical bonding in materials. In FTIR, infrared radiation passes through a sample, certain wavelengths are absorbed, causing molecular bonds to vibrate. Molecules undergo various types of vibrations, including stretching and bending. The result is a spectrum that displays transmittance versus wavenumber, with characteristic peaks corresponding to specific molecular vibrations. The key advantage of FTIR over traditional IR spectroscopy is its use of a mathematical process called Fourier Transform, which allows FTIR to collect a broad range of wavelengths simultaneously, rather than measuring each one individually. Then it converts the data into a spectrum. Analyzing the peaks of the spectrum helps to identify the functional groups and molecular structures. Common functional group regions include O-H stretching: 3200-3600 cm^{-1} (alcohols, phenols); C-H stretching: 2800-3000 cm^{-1} (alkanes, alkenes); C=O stretching: 1650-1750 cm^{-1} (carbonyls, carboxylic acids), and N-H stretching: 3300-3500 cm^{-1} (amines, amides).

2.3.8 STEM-EDX

The size and shape of PNC, PQD, assembly, conjugates, and MWCNT were observed using a STEM. The sample is placed in the STEM grid (ELS-C10, Okenshoji Co., Ltd). Dried well and inserted into the STEM (HD-2000, Hitachi). Here, a focused beam of high-energy electrons passes through the extremely thin perovskite sample. The acceleration voltage is 200 kV. The

electrons can interact with the sample, and the transmitted electrons are detected to form an image. The setup is presented in Figure 2.15. STEM coupled with EDX is used for both high-resolution imaging and elemental analysis. I used STEM-EDX to determine the elemental composition of the PNCs. It helped me to determine the halide vacancies

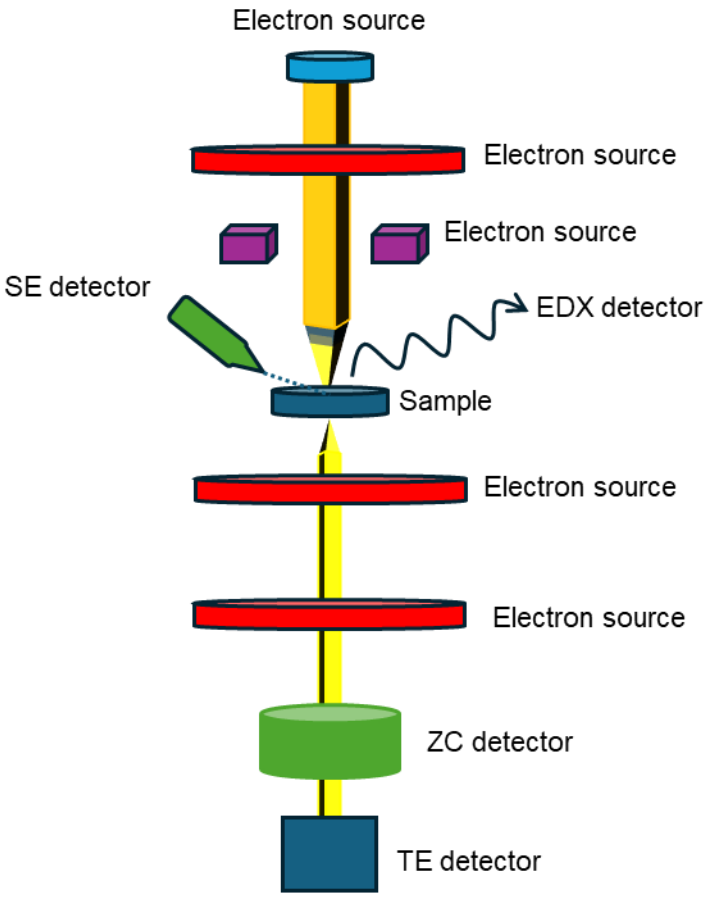

Figure 2.15. Scanning transmission electron microscopy.

present in my sample. When high-energy electrons hit the sample, it can cause the ejection of inner-shell electrons from atoms, leading to vacancies. Higher energy levels of electrons then transition to fill these vacancies, leading to the emission of X-rays characteristic of the elements present in the sample. The EDX detector detects this.

2.3.9 Raman spectroscopy

Functionalized MWCNTs characterization was also performed by measuring the Raman spectra. It involves the scattering of monochromatic light by molecules. Renishaw inVia reflex Raman microscope was used. I used a 532 nm monochromatic laser to excite the sample. Light interacting with a sample can be scattered elastically (Rayleigh scattering) or inelastically (Raman scattering). The Raman scattering has a different energy than the incident light. The energy difference corresponds to vibrational or rotational transitions in the molecule. The

scattered light passes through a notch or edge filter to block Rayleigh's scattered light and allow only the Raman-shifted signals. This signal is then dispersed using a grating. The grating

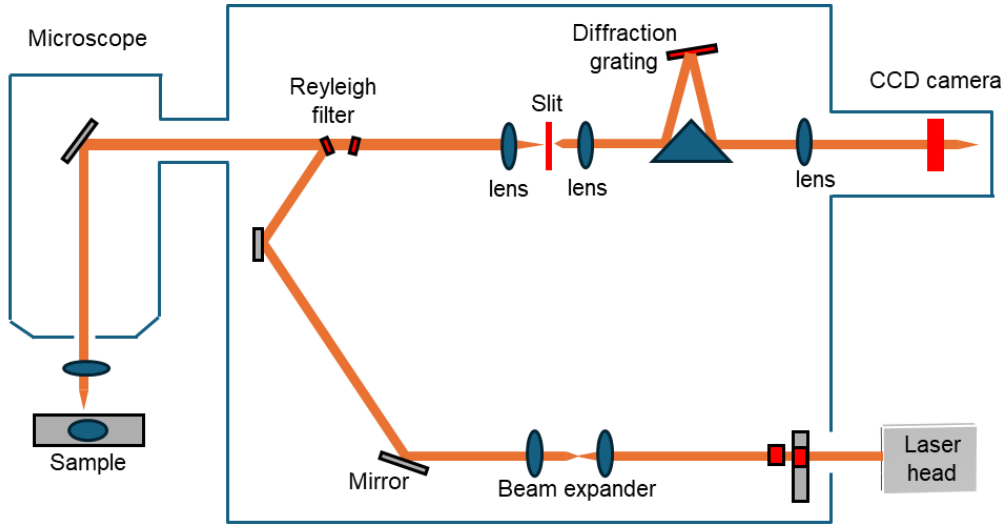

Figure 2.16. Optical setup of a typical Raman microscope.

spreads the light according to its wavelength, creating a Raman spectrum. A CCD detector recorded the spectrum. The instrumental is presented in Figure 2.16. In the case of my sample, the intensity difference of D and G peaks in Raman spectra before and after functionalization helped me to ensure successful functionalization.

References:

(1) Khatun, M. F.; Okamoto, T.; Biju, V. Self-assembled halide perovskite quantum dots in polymer thin films showing temperature-controlled exciton recombination. *Chemical Communications* **2023**, *59* (93), 13831-13834.

(2) Ghimire, S.; Khatun, M. F.; Sachith, B. M.; Okamoto, T.; Sobhanan, J.; Subrahmanyam, C.; Biju, V. Highly luminescent and stable halide perovskite nanocrystals by interfacial defect passivation and amphiphilic ligand capping. *ACS Applied Materials & Interfaces* **2023**, *15* (34), 41081-41091.

(3) Okamoto, T.; Biju, V. Slipping-free halide perovskite supercrystals from supramolecularly-assembled nanocrystals. *Small* **2023**, *19* (32), 2303496.

(4) de Souza, E. L. S.; Oliveira, C. C. Selective radical transformations with aryldiazonium salts. *European Journal of Organic Chemistry* **2023**, *26* (12), e202300073.

(5) Hetemi, D.; Noël, V.; Pinson, J. Grafting of diazonium salts on surfaces: Application to biosensors. *Biosensors* **2020**, *10* (1), 4.

(6) Oskin, P.; Demkina, I.; Dmitrieva, E.; Alferov, S. Functionalization of carbon nanotubes surface by aryl groups: a review. *Nanomaterials* **2023**, *13* (10), 1630.

(7) Kadam, H. K.; Tilve, S. G. Advancement in methodologies for reduction of nitroarenes. *RSC Advances* **2015**, *5* (101), 83391-83407.

(8) Lee, J.; Lee, H.; Kim, C.; Nguyen, T. T. T.; Kim, Y.; Jeong, G.; Chang, M.; Yun, C.; Yoon, H. Controlled growth of perovskite nanocrystals on nanotubes via a nanoseeding intermediate stage: toward novel optoelectronic applications. *The Journal of Physical Chemistry Letters* **2023**, *14* (39), 8837-8845.

Chapter 3

Defect passivation in isolated nanocrystals

Abstract

Excitons are quasi-particles formed due to the coulombic attraction between an electron and a hole in a semiconductor. These entities significantly influence materials' optical and electronic behavior, especially in nanostructures like perovskite nanocrystals (PNCs) and quantum dots (PQDs). Photoluminescence (PL) is produced through the process of radiative exciton recombination. Exciton lifetime is a critical parameter for optimizing devices such as solar cells, where extended excitonic lifetimes enhance charge separation efficiency. Defect-induced exciton/carrier trapping is one of the prominent factors in reducing exciton lifetime. In halide perovskite (HPs), halide vacancies are the major defects responsible for nonradiative recombination. These vacancies are also accountable for lattice degradation, halide ion migration, and PL blinking. Therefore, addressing these defects is important for enhancing the perovskite's performance in optoelectronic applications. In this chapter, I discussed the bromide vacancy filling in $CsPbBr_3$ PNC. Various strategies for filling these vacancies were examined, specifically using NaBr, KBr, or CsBr at the toluene-water interface. EDX, XRD, PL, and exciton lifetime were used to confirm the vacancy filling. Post-treatment with NaBr led to a remarkable increase in PLQY from 57% to 98%, which provides direct evidence of reduced nonradiative decay rates. Single-particle blinking studies further confirm vacancy passivation, as the PL of initially poorly luminescent particles shows significant improvement after vacancy filling. This defect passivation strategy not only enhances the optoelectronic properties but also holds promise for the development of stable, water-soluble HPs which opens new possibilities for high-performance perovskite devices.

3.1 Introduction

HPs have become a focal point of research due to their remarkable optical and electronic characteristics, including strong light absorption, extended carrier diffusion capability, and exceptional energy conversion efficiency in solar cells.[1-3] Although advancements in light-harvesting efficiency have driven remarkable progress in optoelectronic applications, the stability of these devices remains inferior. The instability limits their commercialization and long-term performance.[4] Perovskite instability is a multifaceted issue driven by environmental factors including moisture, heat, and UV exposure, and inherent properties including vacancies, ion migration, and phase transitions.[4-6] Moisture and oxygen can penetrate perovskite layers and trigger chemical reactions that degrade the crystal structure.[7] Prolonged light exposure and thermal cycling can cause phase transitions or ion migration.[8, 9]

Halide vacancies are a key intrinsic factor contributing to the instability of HPs. These vacancies contribute to both chemical degradation and performance losses. For example, Shi *et al.* identified halogen vacancies as the primary electron-trapping defects within halide structures.[10] These vacancies create localized defects in the crystal lattice. These defects create energy levels within the material's band structure that act as a trap. These traps function as centers for non-radiative recombination, capturing either the electron or the hole from the exciton, preventing them from recombining radiatively.[11] Ran *et al*. demonstrated, using machine learning techniques, that bromine vacancies introduce trap states between the band gap in $CsPbBr_3$ at room temperature.[12] For perovskite solar cell applications, efficient extraction of charge carriers is essential to enhance device performance and maximize power conversion efficiency (PCE).[13] However, vacancy-induced energy states in the perovskite structure can capture charge carriers, which hinders their transport and reduces overall device efficiency.[14] Moreover, halide vacancies at the surface or grain boundaries facilitate ion migration, which limits the long-term device stability. Moreover, ion migration can alter the desired bandgap of the material.[15] Therefore, filling these vacancies is crucial to maintaining precise control over excitonic recombination dynamics and carrier lifetimes.

There are various strategies for vacancy-related defect passivation mentioned in the literature. For example, Chouhan *et al.* demonstrated the halide vacancy filling of

$MAPbBr_3$ and $MAPbI_3$ using MABr and MAI solution in dichloromethane. They reported the increased PLQY and lifetime of excitons after successful vacancy filling.[16] Shahjahan *et al.* reported that vacancy-related halide exchange can be homogeneously suppressed by filling the vacancy using the precursor solution.[17] Ren *et al.* also carried out a similar study and showed that the $HC(NH_2)_2PbI_xBr_{3-x}$ perovskite optoelectronic properties are improved by vacancy filling. They achieved PCE up to 18.2% after removing defects from the surface.[18] Similarly Subramaniam *et al.* reported the successful halide vacancy filling of $CsPbBr_3$ PQDs using $SbBr_3$ in toluene.[19] However, the process of halide vacancy filling at the aqueous-organic interface represents a novel area of study. Water is known to infiltrate the perovskite structure, dissolving precursor materials and leading to degradation of the crystal lattice. However, numerous studies have reported that introducing trace amounts of water during synthesis or post-treatment can enhance the optical and electronic properties, and stability of perovskite materials simultaneously by effectively passivating grain boundaries and mitigating surface trap states.[20-24] For instance, Bhatia *et al.* reported that the controlled incorporation of small quantities of water to $FAPbBr_3$ PNCs significantly increases their stability, resulting in a PLQY of 95% in PNC thin films.[22]

This chapter focused on the photogenerated excitons of $CsPbBr_3$ PNCs and their lifetime. I examined the influence of halide vacancies on the PLQY of PNCs and demonstrated a strategy for vacancy passivation. Using the saturated aqueous solution of halide salts, I achieved interfacial halogen transfer from the water phase to the toluene phase which effectively passivates surface vacancies. This process enhances both PL intensity and exciton lifetime. Additionally, single-particle blinking trajectories were analyzed to confirm the effective passivation of halide vacancies. Trap-assisted activation and deactivation of PL are responsible for the Type-B blinking.[25] Our data indicate that halide vacancy passivation suppresses blinking and enhances PL in low-emission particles. These results reveal that effective defect passivation can enhance the stability and efficiency of the optoelectronic devices by reducing nonradiative recombination pathways and limiting ion migration within the perovskite structure. This defect management strategy is therefore promising for the advancement of stable, high-performance PNC-based optoelectronic devices.

3.2 Results and discussions

3.2.1 Synthesis and characterization of $CsPbBr_3$ PNCs

$CsPbBr_3$ PNCs were prepared following the hot injection technique.[26] The hot injection method was used because it enables accurate control over the nucleation of perovskite crystals by injecting a precursor into a hot solvent containing ligands. Several researchers reported that monodispersed PNCs with narrow size distribution can be attained through the hot injection method.[27, 28]

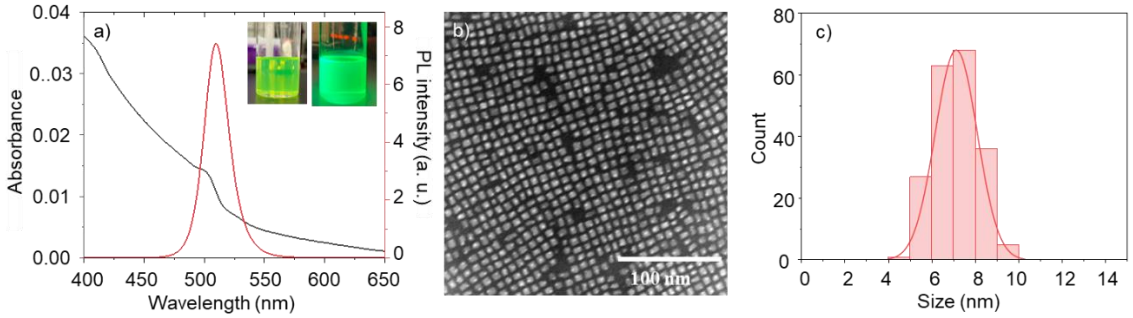

Figure 3.1. Absorption (black) and PL (red) spectra (a), STEM (b), and size distribution (c) of $CsPbBr_3$ PNCs. Inset: Images of $CsPbBr_3$ PNCs at room light and under 365 nm UV radiation.

In this synthesis procedure, I used oleic acid and hexadecylamine as the ligands, and perovskite precursors cesium acetate and $PbBr_2$ were used. 120 °C temperature was used to dissolve all the components in 1-hexadecene. The samples were vacuumed to remove all the moisture and air which are detrimental for PNC synthesis. Hot injection of the Cs-precursor into the Pb-precursor was done at 170 °C under an argon atmosphere. The change in precursor color confirmed the PNC formation after injecting the Cs-precursor into the Pb-precursor. The detailed procedure of synthesis is presented in the experimental chapter. After purification by centrifugation, the final color of the PNCs in toluene is greenish yellow, and under 365 nm laser excitation, it shows green emission (Figure 3.1a inset).

The absorption and PL emission spectra of the colloidal $CsPbBr_3$ PNCs in toluene were measured. The excitation wavelength was 365nm. The absorption and steady-state PL spectra are presented in Figure 3.1a. The as-synthesized $CsPbBr_3$ PNC shows absorption excitonic peak and emission peak in toluene at 501 nm and 510 nm,

respectively (Figure 3.1a). The small Stocks shift represents the higher excitonic binding energy. The Stokes shift denotes the energy disparity between the absorption peak and PL emission maxima of a material. In PNCs, a small Stokes shift indicates that the excitons (electron-hole pairs) recombine without significant energy loss, often attributed to strong Coulombic interactions between the photogenerated electron and hole. High excitonic binding energy results in stronger confinement of excitons, leading to efficient radiative recombination. This is reflected in the small Stokes shift. The size, shape, and morphology of the PNCs were analyzed using STEM. The STEM specimens were prepared by depositing a diluted PNC solution in toluene onto a STEM grid via the drop-

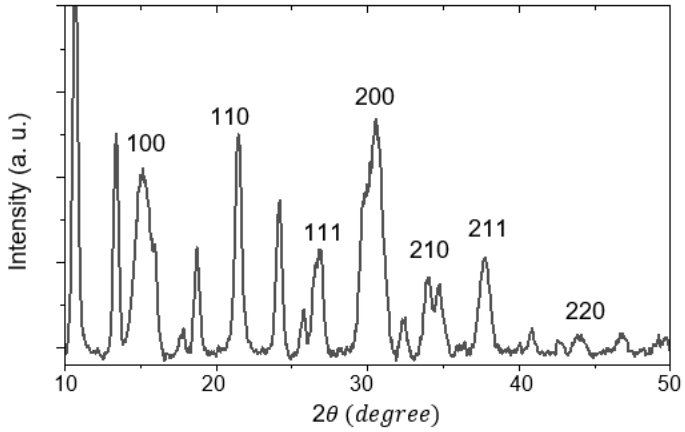

Figure 3.2. XRD of $CsPbBr_3$ PNCs.

casting technique. The residual solution was eliminated by adsorption using an absorbent tissue. The STEM grid was dried overnight under the vacuum. A well-dispersed cubic shape PNCs were observed (Figure 3.1b). The average size of PNCs was 7.12 ± 0.96 nm which was analyzed using the image-j program. The size distribution of the $CsPbBr_3$ PNCs is represented in Figure 3.1c. This is similar to the previously reported data.[29] Smaller size PNCs also indicate the more quantum confinement of the PNCs. When the dimensions of a PNC approach or fall below the exciton Bohr radius, the charge carriers experience quantum confinement in all three spatial directions. This phenomenon arises from fundamental quantum mechanics principles. This quantum confinement alters the optoelectronic properties of the PNCs. As the crystal size shrinks, the spatial confinement of charge carriers increases, raising their kinetic energy. This is a direct consequence of the Heisenberg Uncertainty Principle. Decreasing the spatial extent (Δx) increases the

momentum uncertainty (ΔP), leading to higher energy. Instead of a continuous band of states (as in bulk materials), the energy levels in PNCs become discrete due to size confinement. The separation between energy levels (ΔE) increases with decreasing size.

The crystallographic structure of the as-synthesized PNCs was investigated through XRD analysis of the PNC thin film. The as-synthesized PNC sample was subjected to centrifugation at 14,500 rpm for 15 minutes. The obtained PPT from centrifuged samples was drop cast to prepare films for XRD measurements. The observed XRD peaks arise due to constructive interference of X-rays diffracted by lattice planes. These planes are described by their Miller indices (hkl). The XRD spectra show the characteristic peak at 15.05°, 21.48°, 30.63°, 33.96°, 37.92°, 44.10° and 48.55° corresponding to 100, 110, 200, 210, 211, 220, and 310. These peaks represent the cubic phase (*Pm3m* crystal structure) of $CsPbBr_3$ PNCs (Figure 3.2).[30, 31] The cubic phase of the PNCs was determined by analyzing the reported literature[32-34] and standard ICSD card no #29073. The extra peaks may be generated from the precursors. Defects are common in HPs. Therefore, to assess the quality of synthesized PNCs and to understand defect states, I measured the PLQY (Φ) of the as-prepared $CsPbBr_3$ PNCs. I calculated the Φ values using a relative method, employing standard fluorophores as references for comparison. The fluorophores and their properties are shown in Table 3.1.

Table 3.1. Standard dyes and experimental conditions used for measuring the relative PLQY (Φ) of PNCs.

Dyes	Solvent	λ_{ex} (nm)	λ_{em} (nm)	PLQY	Reference
Coumarin 120	Methanol	365	432	0.71	1
Coumarin 6	Ethanol	420	502	0.78	2
Fluoresceine	Ethanol	425	512	0.79	3
Rhodamine B	Ethanol	510	566	0.70	4
Cresyl violet	Ethanol	540	623	0.54	5

The PLQY of the PNCs was calculated using the following equation[26]

$$\Phi_{PNC} = \Phi_{standard} \times \frac{(\Delta I/\Delta A)_{PNC}}{(\Delta I/\Delta A)_{standard}} \times \frac{\eta_{PNC}^2}{\eta_{standard}^2}$$

Where Φ_{PNC} and $\Phi_{standard}$ represent the PLQY of the PNCs and the standard dyes, respectively. η_{PNC} and $\eta_{standard}$ denote the refractive indices of the solvents that were used to dissolve the PNCs and standard dyes, respectively. $\frac{\Delta I}{\Delta A}$ corresponds to the slope of the integrated PL intensity (I) versus absorbance (A) plots for the standard dyes and PNCs across various dilutions.

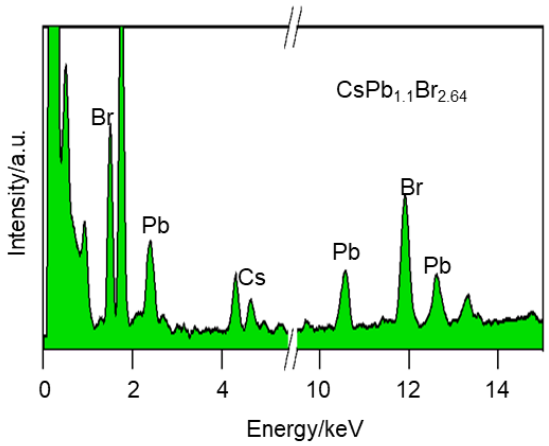

Figure 3.3. EDX of $CsPbBr_3$ PNC thin film.

In this investigation, toluene (η=1.496) was employed as the solvent for dissolving PNC. For the standard dyes, either methanol (η =1.328) or ethanol (η =1.361) was utilized as the solvent. This choice of solvents ensures appropriate solubility and consistency in measurements, thereby enhancing the accuracy of the PLQY determinations. Anyway, the calculated Φ for the PNCs is 57%, which is much lower. PLQY represents the ratio of emitted photons to absorbed photons. A low PLQY indicates that a substantial fraction of the absorbed energy in a material is not re-emitted as light but is lost through non-radiative processes. Radiative recombination occurs through the emitting photon which is responsible for increasing the PLQY. La-Placa *et al.* reported that the low PLQY can be ascribed to the presence of free charge carriers and defect-induced trap states, which serve as pathways for non-radiative recombination.[35] Xiaochen Wang *et al.* reported the deep-level chloride vacancy in mixed halide PNC with PLQY 30% only.[36] Usually PNCs have high surface-to-volume ratio which increases the likelihood of surface imperfections and surface-related defects. There are different kinds of point defects in the HPs as discussed in Chapter 1. Vacancies are a type of point defect commonly found in perovskites. Due to their relatively low formation energy, vacancies tend to form more easily[37], often resulting

in the creation of trap states inside the material. These trap states can capture charge carriers and hinder the efficient recombination of excitons. However, there are different types of vacancies present in the perovskite including A-site, B-site, and halide vacancies.[38]

To further elucidate the nature of these defects (vacancies), I conducted STEM-EDX (Figure 3.3). STEM-EDX provides elemental maps and spectra for all elements of a compound. The intensity of the X-ray peaks is proportional to the elemental concentration within the sample. The sample preparation for these experiments is similar to STEM sample preparation as discussed before. The resultant elemental ratios were determined to be Cs:Pb:Br = 1:1.1:2.64. This lower amount of bromine in the synthesized PNCs compared to the expected stoichiometric ratio (Cs:Pb:Br = 1:1:3) can be attributed to the presence of bromine vacancies. This Br- vacancies is the reason for the low Φ value.

The density and energy distribution of defect-induced traps within the electronic band structure are crucial factors influencing the performance of the device. An increase in trap density is associated with a shift in trap energy levels closer to the mid-band gap and has been shown to negatively impact carrier diffusion and reduce the open-circuit voltage of solar cells.[39] Studies have revealed that the trap density in perovskite is highly sensitive to processing techniques, leading to variations in results even for the same material.[11, 40] Addressing and minimizing these traps is still a significant scientific and technological challenge. However, reducing their effects is essential for improving optoelectronic properties because, nearly trap-free conditions have been achieved in $CsPbI_3$ QDs, resulting in PLQY approaching unity.[41] Various defect passivation methods have been extensively reported in the literature. For PNCs, post-synthetic passivation methods are among the most commonly employed strategies.[42] Typically, a range of organic and inorganic compounds serve as halide sources for this purpose. However, organic compounds such as methylammonium iodide (MAI) are volatile, which can inadvertently introduce additional defects. Moreover, organic compounds often face solubility challenges in non-polar solvents, as PNCs are highly sensitive to polar solvents. Additionally, some halide sources, such as antimony bromide ($SbBr_3$), are expensive,

limiting their practical application. Therefore, developing an efficient and cost-effective strategy to address halide vacancy passivation in PNCs remains a critical research priority.

3.2.2 Defect passivation

I investigated the passivation of halide vacancies using various inorganic bromide salts including CsBr, NaBr, and KBr. First, a saturated solution of the salts is prepared by dissolving them in water. The PNC dispersion in toluene is added to the mixture, followed by vigorous shaking to ensure thorough mixing. The phases are then allowed to settle, and this process is conducted multiple times. Since the solution is saturated, the likelihood

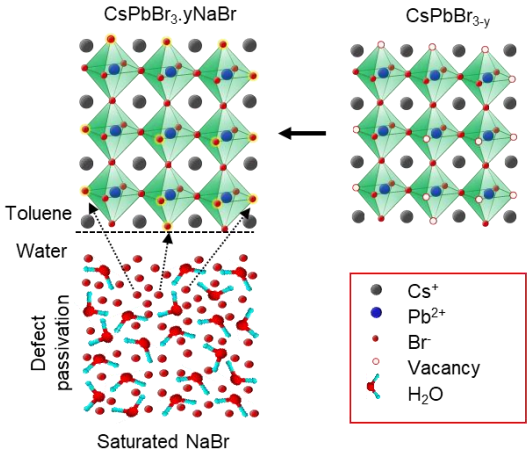

Figure 3.4. Mechanism of halide vacancy filling of $CsPbBr_3$ PNCs using saturated NaBr solution at toluene and water interface.

of water dissolving the perovskite is minimized. Finally, the toluene part is collected, and measured. The anticipated mechanism for vacancy filling involves the migration of bromide ions from the aqueous phase to the toluene phase, where they occupy the vacancies. (Figure 3.4) The higher affinity of the vacancies for bromide ions serves as the driving force for the transfer of the bromine species. Anyway, among these salts, NaBr exhibited the most effective passivation results. I selected NaBr to minimize potential influences from K^+ and Cs^+ ions in terms of surface passivation and the possibility of inducing compositional or phase changes. For example, previous studies have reported the PL enhancement of the $CsPbI_{3-x}Br_x$ PNCs using KBr. However, they observed the formation of a $KBr_{1-x}I_x$ impurity phase due to high amount of K^+ ions present during the surface passivation, which adversely impacted the morphology, structural integrity, and

optical characteristics of the PNCs.[43] Additionally, in our experiments, post-synthesis treatment of $CsPbBr_3$ PNCs with CsBr in aqueous solution resulted in notable changes in

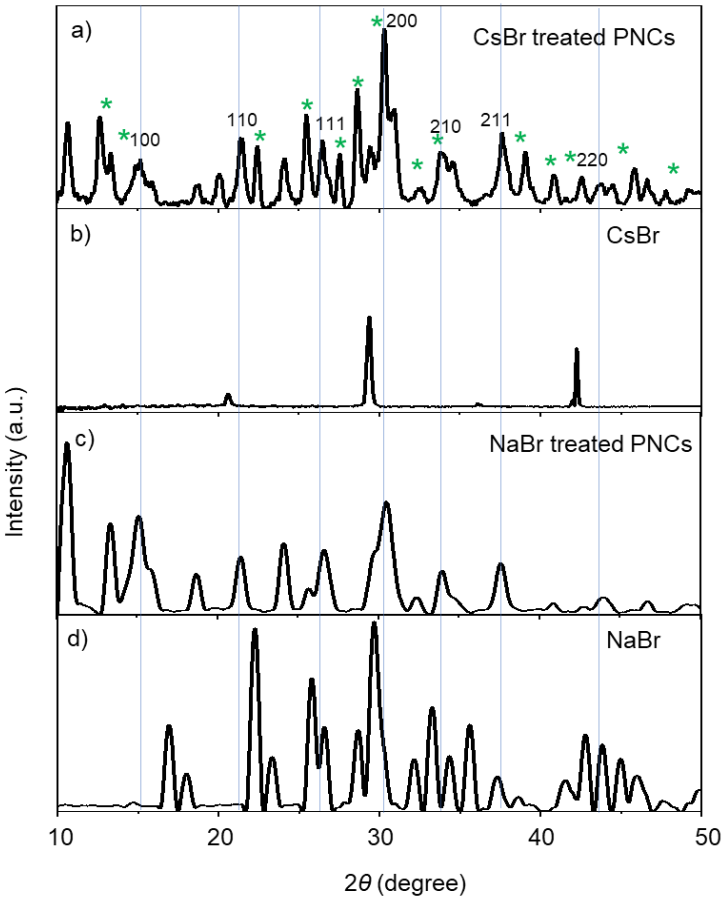

Figure 3.5. XRD pattern $CsPbBr_3$ PNC thin film treated with CsBr (a), CsBr itself (b), $CsPbBr_3$ PNC treated with NaBr (c), and NaBr itself (d). Green stars are the characteristic peaks of double perovskite.

the XRD patterns (Figure 3.5a), suggestive of double perovskite formation (Cs_4PbBr_6).[44] The CsBr XRD is presented in Figure 3.5b. CsBr crystallizes in a cubic structure with the cesium chloride (CsCl) type arrangement, belonging to the $Pm\bar{3}m$ space group. It possesses a structure defined by a basic cubic lattice where each cesium ion is surrounded by eight bromine ions, and vice versa, resulting in a high coordination number of 8:8. However, no notable variations were detected in the XRD patterns following NaBr treatment, indicating stability in the crystal structure (Figure 3.5c). Furthermore, XRD data confirmed the absence of residual NaBr precipitation on the PNC surfaces after NaBr treatment (Figure 3.5d). NaBr adopts a rock-salt (NaCl) type structure, also cubic, but

with the Fm̄3m space group. In this arrangement, each sodium ion is surrounded by six bromine ions in an octahedral coordination, and each bromine ion is similarly coordinated by six sodium ions, forming a 6:6 coordination. Based on the above findings, I concentrated our bromine vacancy passivation studies on NaBr treatment. After post-treating the PNC in toluene with saturated aqueous NaBr solution, STEM-EDX analysis was performed to reassess the atomic composition. The samples of STEM-EDX are prepared by drop casting the defect-passivated PNCs on the STEM grid. The obtained spectra from EDX were analyzed and the ratios of the compounds were obtained. The post-treatment composition was found to be Cs:Pb:Br = 1:1.17:2.98 (Figure 3.6a and 3.6b)

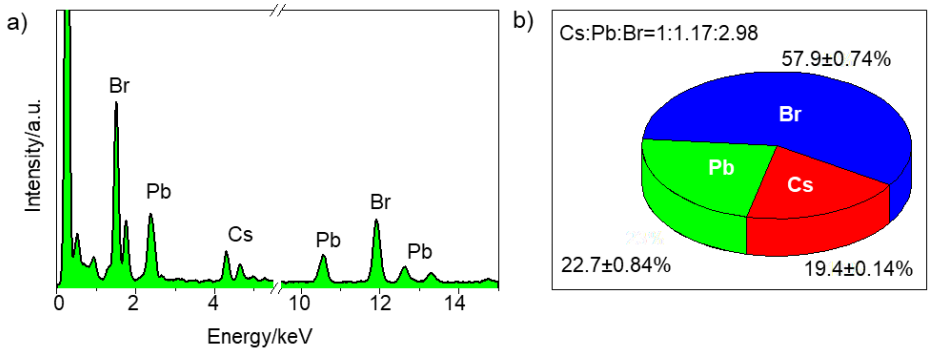

Figure 3.6. a) EDX spectra of $CsPbBr_3$ PNCs following post-treatment with a saturated aqueous NaBr solution. b) Pie chart representation of the elemental composition of NaBr-treated PNCs, including standard deviation values.

closely approximating the standard stoichiometric ratio. These findings indicate the effective filling of anion vacancies within the lattice.

Additionally, the PLQY of the treated PNCs was measured, showing a significant increase to 98 ± 2% within 15 minutes, further supporting the efficacy of the NaBr post-treatment in enhancing material quality and luminescence efficiency. The PL spectra and the PL lifetime prior to and following the vacancy passivation with NaBr are presented in Figure 3.7a and 3.7b, respectively. Although there is a huge change in PL intensity, PL lifetime change from 11.6 ns to 13.8 ns. The PL lifetime is the average time the charge carrier remains excited before recombining. It is defined by the total decay rate-

$$\tau = \frac{1}{k_r + k_{nr}}$$

Where, k_r is the radiative and k_{nr} is the nonradiative decay constate.

Φ can be defined as -

$$\Phi = \frac{k_r}{k_r + k_{nr}}$$

From these 2 equations, the calculated k_r value of as-synthesized PNCs is 4.9×10^7 s^{-1}, whereas the nonradiative rate is 3.7×10^7 s^{-1}. Following the NaBr treatment, k_{nr} is decreased to 1.4×10^6 s^{-1} whereas k_r increased to 7.1×10^7 s^{-1}. This observed enhancement in radiative recombination and reduction in nonradiative pathways further substantiates the passivation of vacancy-related defects. Notably, the 72% increase in Φ (from 57% to 98%) after NaBr treatment is associated with only a 19% increase in the average PL lifetime. The disproportionate increases in Φ and average lifetime imply a redistribution of both radiative and nonradiative recombination rates following NaBr passivation. The

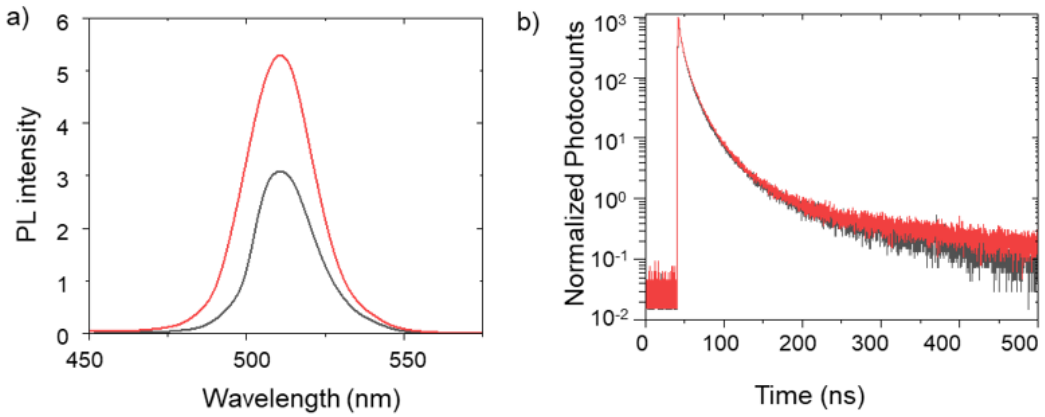

Figure 3.7. PL spectra (a) and PL decay (b) of $CsPbBr_3$ PNCs before (Black) and after (Red) the treatment with the saturated aqueous NaBr solution.

PLQY and carrier lifetime are closely related properties in light-emitting materials, especially in semiconductor nanocrystals. When *kr*≫ *knr*, radiative recombination dominates, resulting in long radiative lifetimes (τ) and high PLQY. The carrier lifetime, in this case, is approximately equal to the radiative lifetime. If *knr* ≫ *kr*, non-radiative recombination dominates, leading to shorter PL lifetimes and lower PLQY, as most carriers recombine non-radiatively. PLQY and carrier lifetime are influenced by the

balance of *kr* and *knr*. For a fixed *kr*, increasing *knr* shortens the carrier lifetime and reduces PLQY.

These radiative and nonradiative rates are also dependent on the sample preparation, experimental condition, and laser power. For example, the carrier density depends on the laser power and absorption characteristics of the material. As the laser power increases, the carrier density (n) rises, influencing recombination dynamics. At low laser power, trap-assisted recombination dominates. *Knr* remains relatively constant, since it depends mainly on the defect density and trap filling. With increasing laser power, more traps are filled, and the trap-assisted *knr* can saturate. At this stage, radiative recombination becomes more significant compared to non-radiative recombination. At high laser power, Auger recombination dominates, and *knr* increases significantly, scaling with n^2or n^3. This leads to a decrease in PLQY and shorter exciton lifetimes due to the increasing non-radiative losses.

3.2.3 Single-particle study

I measured the single particle PL blinking to confirm the successful defect passivation because one of the reasons of blinking is trap. In blinking, individual dots randomly switch between "on" (emitting) and "off" (non-emitting) states. This phenomenon is discovered by researchers M. Nirmal and Louis Brus and their team in CdSe QDs.[45] There are major 2 types of blinking present: type A and type B. Type A bilking is due to the changing discharging of particles whereas, type B blinking is attributed to the trapping and subsequent de-trapping of charge carriers within defect-induced energy states.[16, 46, 47] This blinking behavior provides valuable insight into charge carrier dynamics and their interactions with defect states. I prepared the sample by the drop and drag method. A very dilute solution of both as-synthesized and defect-passivated PNC in toluene was dropped on the cover slip and using a lens cleaning paper the solution was dragged. Then the coverslip was dried properly. I observed the single PNC dots using the EMCCD camera, I noticed that different blinking behaviour is present in our as-synthesized PNC sample (Figure 3.8). In my synthesized PNCs, the observed blinking may be due to the trapping-detrapping and charging-discharging of charge carriers. However, Ahmed *el al.* demonstrated that the trapping of charge carriers in defects is responsible for most of the blinking in $CsPbBr_3$ NCs.[48] They passivated the defects by treating PNCs with

tetrafluoroborate salt. This post-treatment removes most of the nonradiative recombination. Some of the blinking trajectories before NaBr treatment of the as-synthesized $CsPbBr_3$ are represented in Figure 3.8.

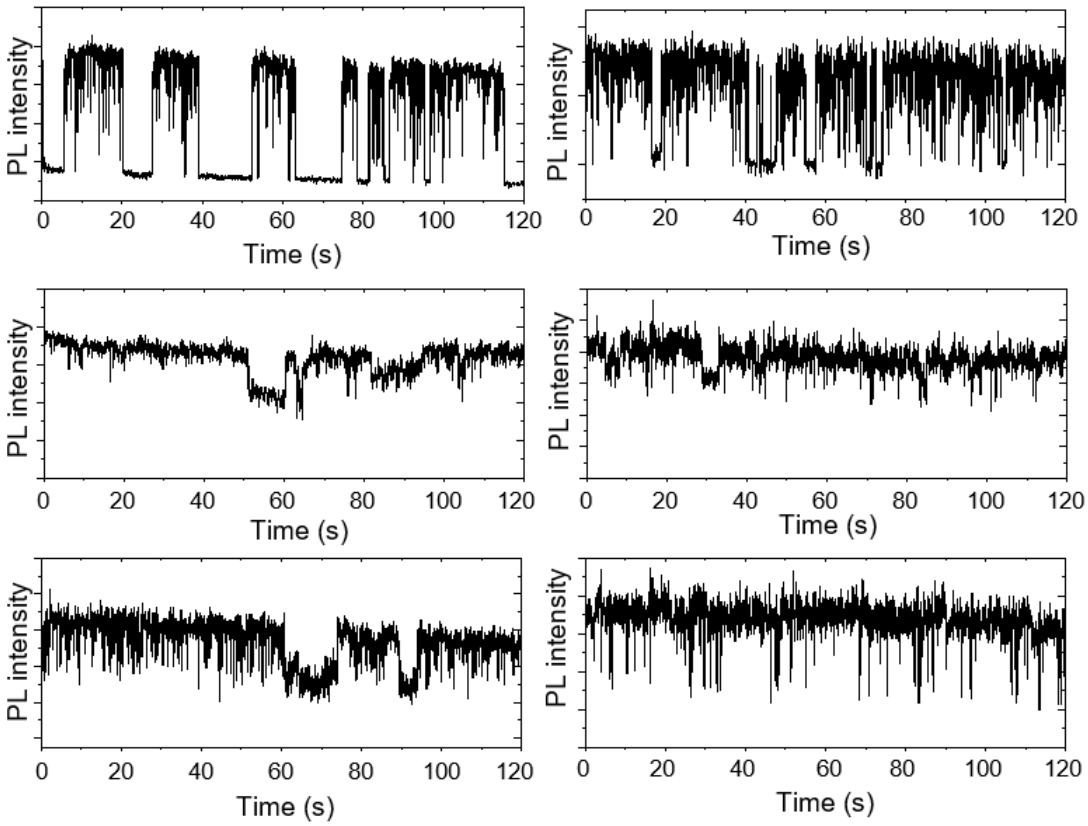

Figure 3.8. PL intensity trajectories of as-synthesized $CsPbBr_3$ PNC.

These trajectories were collected from individual PNCs, which show variation from particle to particle. A small extent of bleaching is present in the PL intensity. This is because the experiments were carried out in the air. Our lab previously reported the decreasing PL emission in the presence of air at single particle level.[49] However, almost all of the single particles observed have a fluctuation of PL intensity. Paul *et al.* also reported the presence of similar blinking properties in $CsPbBr_3$ PNCs. They observed an increase in the charge carrier trapping rate with decreasing PNC size.[50]

The ON- and OFF- probabilities were calculated from the collected trajectories (Figure 3.9). For calculation, a threshold level of PL intensity was determined to distinguish the OFF state from the ON state. The ON probability was fitted with a truncated power law ($P\ (\tau_{on}) = A_0 \tau_{on}^{-m} e^{-\frac{\tau_{on}}{\tau_c}}$) and the OFF was probability follow linear

power law ($P\left(\tau_{off}\right) = A_0\tau_{off}^{m}$), where A_0 is a constant, m is a power law coefficient,

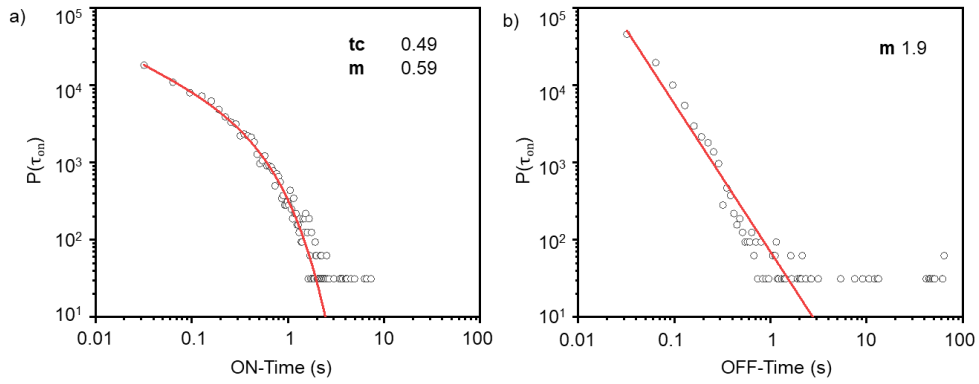

Figure 3.9. The probability distribution of (a) ON- and (b) OFF- times of as-synthesized $CsPbBr_3$ PNC.

and τ_c is truncation time. Both short and long ON and OFF are present in the sample. However, the occurrence of the OFF-event is higher than the ON events.

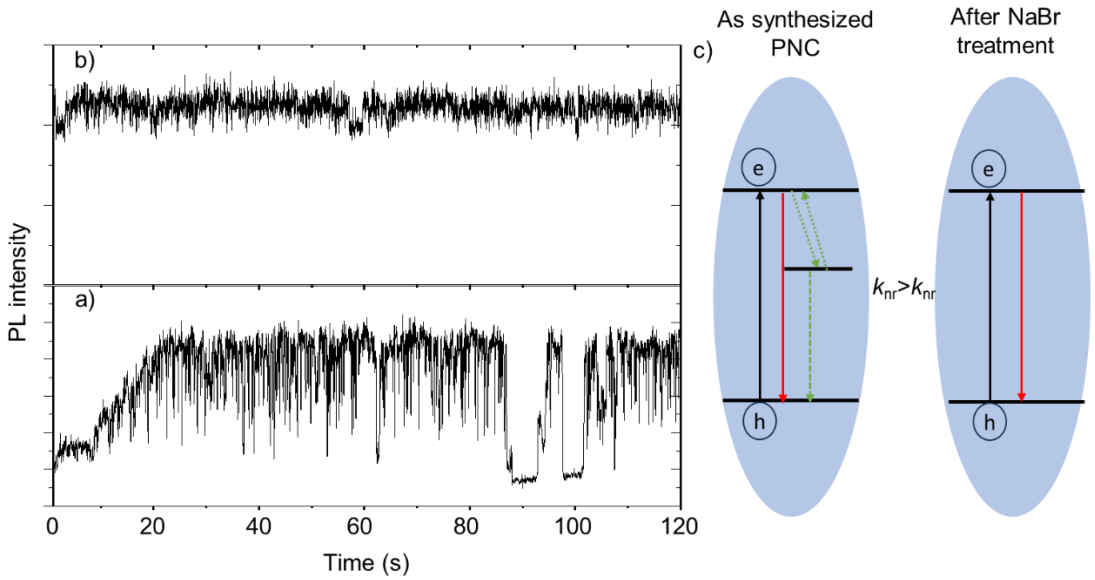

Figure 3.10. (a-b) PL blinking trajectories of $CsPbBr_3$ PNCs after NaBr treatment. (c) The mechanism of blinking suppression.

Similarly, after NaBr treatment, I measured the blinking. I observed PNCs behave differently this time. Some poorly luminescent PNCs show gradual photo-brightening (Figure 3.10a), and other PNCs show suppression of blinking (Figure 3.10b). The blinking that remains in PNC after NaBr treatment can be assigned as a type A blinking

which is because of the auger process. Studies have also indicated that single particle can display simultaneously type-A and type-B blinking patterns.[51-53] However, the suppression of surface defects has been shown to decrease type-B blinking compared to type-A blinking behavior as reported by Takagi *et al.*[53] Therefore, This suppression of blinking and increasing PL indicate successful passivation of halide vacancies by NaBr, resulting in a decrease in k_{nr} of the sample (Figure 3.10c).

3.3 Conclusions

In conclusion, this research highlights the significance of halide vacancy passivation in enhancing the optoelectronic properties of $CsPbBr_3$ PNCs and the broader implications for optoelectronic device stability and performance. Halide vacancies in perovskite structures significantly degrade PLQY and exciton lifetime due to nonradiative recombination pathways. These intrinsic defects act as traps for charge carriers, reducing both luminescence efficiency and long-term stability of devices. By employing NaBr as a passivation agent at the toluene-water interface, I achieved effective bromine vacancy filling, increasing PLQY from 57% to 98%. This enhancement, supported by both ensemble and single-particle PL studies. The results demonstrate reduced nonradiative decay and suppression of blinking behavior which indicate the reduction of trap-related defects. Post-treatment analysis also indicates improved radiative recombination rates and stabilized PNC structure, without introducing detrimental compositional changes. The NaBr passivation method offers a promising approach to achieving highly luminescent, stable PNCs, supporting the development of durable, high-efficiency perovskite-based technologies.

References

(1) Chen, Y.; Yi, H.; Wu, X.; Haroldson, R.; Gartstein, Y.; Rodionov, Y.; Tikhonov, K.; Zakhidov, A.; Zhu, X.-Y.; Podzorov, V. Extended carrier lifetimes and diffusion in hybrid perovskites revealed by Hall effect and photoconductivity measurements. *Nature Communications* **2016**, *7* (1), 12253.

(2) Tang, H.; He, S.; Peng, C. A short progress report on high-efficiency perovskite solar cells. *Nanoscale Research Letters* **2017**, *12*, 1-8.

(3) Kim, J. Y.; Lee, J.-W.; Jung, H. S.; Shin, H.; Park, N.-G. High-efficiency perovskite solar cells. *Chemical Reviews* **2020**, *120* (15), 7867-7918.

(4) Fu, W.; Ricciardulli, A. G.; Akkerman, Q. A.; John, R. A.; Tavakoli, M. M.; Essig, S.; Kovalenko, M. V.; Saliba, M. Stability of perovskite materials and devices. *Materials Today* **2022**, *58*, 275-296.

(5) Park, B. W.; Seok, S. I. Intrinsic instability of inorganic–organic hybrid halide perovskite materials. *Advanced Materials* **2019**, *31* (20), 1805337.

(6) Conings, B.; Drijkoningen, J.; Gauquelin, N.; Babayigit, A.; D'Haen, J.; D'Olieslaeger, L.; Ethirajan, A.; Verbeeck, J.; Manca, J.; Mosconi, E. Intrinsic thermal instability of methylammonium lead trihalide perovskite. *Advanced Energy Materials* **2015**, *5* (15), 1500477.

(7) Yu, J.; Liu, G.; Chen, C.; Li, Y.; Xu, M.; Wang, T.; Zhao, G.; Zhang, L. Perovskite $CsPbBr_3$ crystals: growth and applications. *Journal of Materials Chemistry C* **2020**, *8* (19), 6326-6341.

(8) Yuan, H.; Debroye, E.; Janssen, K.; Naiki, H.; Steuwe, C.; Lu, G.; Moris, M.; Orgiu, E.; Uji-i, H.; De Schryver, F. Degradation of methylammonium lead iodide perovskite structures through light and electron beam driven ion migration. *The Journal of Physical Chemistry Letters* **2016**, *7* (3), 561-566.

(9) Leung, T. L.; Ren, Z.; Syed, A. A.; Grisanti, L.; Djurišić, A. B.; Popović, J. Photoinduced segregation behavior in 2D mixed halide perovskite: effects of light and heat. *ACS Energy Letters* **2022**, *7* (10), 3500-3508.

(10) Shi, H.; Du, M.-H. Shallow halogen vacancies in halide optoelectronic materials. *Physical Review B* **2014**, *90* (17), 174103.

(11) Jin, H.; Debroye, E.; Keshavarz, M.; Scheblykin, I. G.; Roeffaers, M. B.; Hofkens, J.; Steele, J. A. It's a trap! On the nature of localised states and charge trapping in lead halide perovskites. *Materials Horizons* **2020**, *7* (2), 397-410.

(12) Ran, J.; Wang, B.; Wu, Y.; Liu, D.; Mora Perez, C.; Vasenko, A. S.; Prezhdo, O. V. Halide vacancies create no charge traps on lead halide perovskite surfaces but can generate deep traps in the bulk. *The Journal of Physical Chemistry Letters* **2023**, *14* (26), 6028-6036.

(13) Yue, S.; Liu, K.; Xu, R.; Li, M.; Azam, M.; Ren, K.; Liu, J.; Sun, Y.; Wang, Z.; Cao, D. Efficacious engineering on charge extraction for realizing highly efficient perovskite solar cells. *Energy & Environmental Science* **2017**, *10* (12), 2570-2578.

(14) Hu, Y.; Hutter, E. M.; Rieder, P.; Grill, I.; Hanisch, J.; Aygüler, M. F.; Hufnagel, A. G.; Handloser, M.; Bein, T.; Hartschuh, A. Understanding the role of cesium and rubidium additives in perovskite solar cells: trap states, charge transport, and recombination. *Advanced Energy Materials* **2018**, *8* (16), 1703057.

(15) Jiang, H.; Cui, S.; Chen, Y.; Zhong, H. Ion exchange for halide perovskite: From nanocrystal to bulk materials. *Nano Select* **2021**, *2* (11), 2040-2060.

(16) Chouhan, L.; Ito, S.; Thomas, E. M.; Takano, Y.; Ghimire, S.; Miyasaka, H.; Biju, V. Real-time blinking suppression of perovskite quantum dots by halide vacancy filling. *ACS Nano* **2021**, *15* (2), 2831-2838.

(17) Shahjahan, M.; Yuyama, K. I.; Okamoto, T.; Biju, V. Heterojunction perovskite microrods prepared by remote-controlled vacancy filling and halide exchange. *Advanced Materials Technologies* **2021**, *6* (2), 2000934.

(18) Ren, Y.; Chen, J.; Ji, D.; Sun, Y.; Li, C. Improve the quality of $HC(NH_2)_2PbI_xBr_{3-x}$ through iodine vacancy filling for stable mixed perovskite solar cells. *Chemical Engineering Journal* **2020**, *384*, 123273.

(19) Subramaniam, M. R.; Pramod, A. K.; Hevia, S. A.; Batabyal, S. K. Enhanced photoluminescence quantum yield, lifetime, and photodetector responsivity of $CsPbBr_3$ quantum dots via antimony tribromide post-treatment. *The Journal of Physical Chemistry C* **2022**, *126* (3), 1462-1470.

(20) Eperon, G. E.; Habisreutinger, S. N.; Leijtens, T.; Bruijnaers, B. J.; van Franeker, J. J.; DeQuilettes, D. W.; Pathak, S.; Sutton, R. J.; Grancini, G.; Ginger, D. S. The importance of moisture in hybrid lead halide perovskite thin film fabrication. *ACS Nano* **2015**, *9* (9), 9380-9393.

(21) Wu, L.; Hu, H.; Xu, Y.; Jiang, S.; Chen, M.; Zhong, Q.; Yang, D.; Liu, Q.; Zhao, Y.; Sun, B. From nonluminescent Cs_4PbX_6 (X= Cl, Br, I) nanocrystals to highly luminescent $CsPbX_3$ nanocrystals: water-triggered transformation through a CsX-stripping mechanism. *Nano Letters* **2017**, *17* (9), 5799-5804.

(22) Bhatia, H.; Martin, C.; Keshavarz, M.; Dovgaliuk, I.; Schrenker, N. J.; Ottesen, M.; Qiu, W.; Fron, E.; Bremholm, M.; Van de Vondel, J. Deciphering the role of water in promoting the optoelectronic performance of surface-engineered lead halide perovskite nanocrystals. *ACS Applied Materials & Interfaces* **2023**, *15* (5), 7294-7307.

(23) Zhang, X.; Bai, X.; Wu, H.; Zhang, X.; Sun, C.; Zhang, Y.; Zhang, W.; Zheng, W.; Yu, W. W.; Rogach, A. L. Water-assisted size and shape control of $CsPbBr_3$ perovskite nanocrystals. *Angewandte Chemie International Edition* **2018**, *57* (13), 3337-3342.

(24) Liu, Y.; Li, F.; Liu, Q.; Xia, Z. Synergetic effect of postsynthetic water treatment on the enhanced photoluminescence and stability of $CsPbX_3$ (X= Cl, Br, I) perovskite nanocrystals. *Chemistry of Materials* **2018**, *30* (19), 6922-6929.

(25) Trinh, C. T.; Minh, D. N.; Ahn, K. J.; Kang, Y.; Lee, K.-G. Verification of Type-A and Type-B-HC blinking mechanisms of organic–inorganic formamidinium lead halide perovskite quantum dots by FLID measurements. *Scientific Reports* **2020**, *10* (1), 2172.

(26) Ghimire, S.; Khatun, M. F.; Sachith, B. M.; Okamoto, T.; Sobhanan, J.; Subrahmanyam, C.; Biju, V. Highly luminescent and stable halide perovskite nanocrystals by interfacial defect passivation and amphiphilic ligand capping. *ACS Applied Materials & Interfaces* **2023**, *15* (34), 41081-41091.

(27) Chen, X.; Peng, L.; Huang, K.; Shi, Z.; Xie, R.; Yang, W. Non-injection gram-scale synthesis of cesium lead halide perovskite quantum dots with controllable size and composition. *Nano Research* **2016**, *9*, 1994-2006.

(28) Koolyk, M.; Amgar, D.; Aharon, S.; Etgar, L. Kinetics of cesium lead halide perovskite nanoparticle growth; focusing and de-focusing of size distribution. *Nanoscale* **2016**, *8* (12), 6403-6409.

(29) Okamoto, T.; Biju, V. Slipping-free halide perovskite supercrystals from supramolecularly-assembled nanocrystals. *Small* **2023**, *19* (32), 2303496.

(30) Algadi, H.; Mahata, C.; Woo, J.; Lee, M.; Kim, M.; Lee, T. Enhanced photoresponsivity of all-inorganic ($CsPbBr_3$) perovskite nanosheets photodetector with carbon nanodots (CDs). *Electronics* **2019**, *8* (6), 678.

(31) Bhagyalakshmi, S. B.; Ghimire, S.; Takahashi, K.; Yuyama, K. i.; Takano, Y.; Nakamura, T.; Biju, V. Nonradiative energy transfer through distributed bands in piezochemically synthesized cesium and formamidinium lead halide perovskites. *Chemistry–A European Journal* **2020**, *26* (10), 2133-2137.

(32) Hanusch, F. C.; Wiesenmayer, E.; Mankel, E.; Binek, A.; Angloher, P.; Fraunhofer, C.; Giesbrecht, N.; Feckl, J. M.; Jaegermann, W.; Johrendt, D. Efficient planar heterojunction perovskite solar cells based on formamidinium lead bromide. *The Journal of Physical Chemistry Letters* **2014**, *5* (16), 2791-2795.

(33) Ghimire, S.; Chouhan, L.; Takano, Y.; Takahashi, K.; Nakamura, T.; Yuyama, K.-i.; Biju, V. Amplified and multicolor emission from films and interfacial layers of lead halide perovskite nanocrystals. *ACS Energy Letters* **2018**, *4* (1), 133-141.

(34) Song, J.; Li, J.; Li, X.; Xu, L.; Dong, Y.; Zeng, H. Quantum dot light-emitting diodes based on inorganic perovskite cesium lead halides ($CsPbX_3$). *Advanced Materials (Deerfield Beach, Fla.)* **2015**, *27* (44), 7162-7167.

(35) La-Placa, M.-G.; Longo, G.; Babaei, A.; Martínez-Sarti, L.; Sessolo, M.; Bolink, H. J. Photoluminescence quantum yield exceeding 80% in low dimensional perovskite thin-films via passivation control. *Chemical Communications* **2017**, *53* (62), 8707-8710.

(36) Wang, X.; Bai, T.; Meng, X.; Ji, S.; Zhang, R.; Zheng, D.; Yang, B.; Jiang, J.; Han, K.-l.; Liu, F. Filling chlorine vacancy with bromine: a two-step hot-injection approach achieving defect-free hybrid halogen perovskite nanocrystals. *ACS Applied Materials & Interfaces* **2022**, *14* (41), 46857-46865.

(37) Choon, S. L.; Lim, H. N. Impact of Vacancies in Halide Perovskites for Batteries and Supercapacitors. *Materials Today Energy* **2024**, 101577.

(38) Min, J.; Choi, Y.; Kim, D.; Park, T. Beyond imperfections: exploring defects for breakthroughs in perovskite solar cell research. *Advanced Energy Materials* **2024**, *14* (6), 2302659.

(39) Kramer, I. J.; Sargent, E. H. Colloidal quantum dot photovoltaics: a path forward. *ACS Nano* **2011**, *5* (11), 8506-8514.

(40) Fassl, P.; Lami, V.; Bausch, A.; Wang, Z.; Klug, M. T.; Snaith, H. J.; Vaynzof, Y. Fractional deviations in precursor stoichiometry dictate the properties, performance and stability of perovskite photovoltaic devices. *Energy & Environmental Science* **2018**, *11* (12), 3380-3391.

(41) Liu, F.; Zhang, Y.; Ding, C.; Kobayashi, S.; Izuishi, T.; Nakazawa, N.; Toyoda, T.; Ohta, T.; Hayase, S.; Minemoto, T. Highly luminescent phase-stable $CsPbI_3$ perovskite quantum dots achieving near 100% absolute photoluminescence quantum yield. *ACS Nano* **2017**, *11* (10), 10373-10383.

(42) Ye, J.; Byranvand, M. M.; Martínez, C. O.; Hoye, R. L.; Saliba, M.; Polavarapu, L. Defect passivation in lead-halide perovskite nanocrystals and thin films: toward efficient LEDs and solar cells. *Angewandte Chemie* **2021**, *133* (40), 21804-21828.

(43) Yang, J.-N.; Song, Y.; Yao, J.-S.; Wang, K.-H.; Wang, J.-J.; Zhu, B.-S.; Yao, M.-M.; Rahman, S. U.; Lan, Y.-F.; Fan, F.-J. Potassium bromide surface passivation on $CsPbI_{3-x}Br_x$ nanocrystals for efficient and stable pure red perovskite light-emitting diodes. *Journal of the American Chemical Society* **2020**, *142* (6), 2956-2967.

(44) Li, Y.; Shao, W.; Chen, L.; Wang, J.; Nie, J.; Zhang, H.; Zhang, S.; Gao, R.; Ouyang, X.; Ouyang, X. Lead-halide Cs_4PbBr_6 single crystals for high-sensitivity radiation detection. *NPG Asia Materials* **2021**, *13* (1), 40.

(45) Nirmal, M.; Dabbousi, B. O.; Bawendi, M. G.; Macklin, J.; Trautman, J.; Harris, T.; Brus, L. E. Fluorescence intermittency in single cadmium selenide nanocrystals. *Nature* **1996**, *383* (6603), 802-804.

(46) Efros, A. L.; Nesbitt, D. J. Origin and control of blinking in quantum dots. *Nature Nanotechnology* **2016**, *11* (8), 661-671.

(47) Kim, T.; Jung, S. I.; Ham, S.; Chung, H.; Kim, D. Elucidation of photoluminescence blinking mechanism and multiexciton dynamics in hybrid organic–inorganic perovskite quantum dots. *Small* **2019**, *15* (33), 1900355.

(48) Ahmed, T.; Seth, S.; Samanta, A. Mechanistic investigation of the defect activity contributing to the photoluminescence blinking of $CsPbBr_3$ perovskite nanocrystals. *ACS Nano* **2019**, *13* (11), 13537-13544.

(49) Chouhan, L.; Ghimire, S.; Biju, V. Blinking beats bleaching: the control of superoxide generation by photo-ionized perovskite nanocrystals. *Angewandte Chemie International Edition* **2019**, *58* (15), 4875-4879.

(50) Paul, S.; Kishore, G.; Samanta, A. Photoluminescence blinking of quantum confined $CsPbBr_3$ perovskite nanocrystals: Influence of size. *The Journal of Physical Chemistry C* **2023**, *127* (21), 10207-10214.

(51) Galland, C.; Ghosh, Y.; Steinbrück, A.; Sykora, M.; Hollingsworth, J. A.; Klimov, V. I.; Htoon, H. Two types of luminescence blinking revealed by spectroelectrochemistry of single quantum dots. *Nature* **2011**, *479* (7372), 203-207.

(52) Yuan, G.; Gómez, D. E.; Kirkwood, N.; Boldt, K.; Mulvaney, P. Two mechanisms determine quantum dot blinking. *ACS Nano* **2018**, *12* (4), 3397-3405.

(53) Takagi, T.; Omagari, S.; Vacha, M. Suppression of blinking in single $CsPbBr_3$ perovskite nanocrystals through surface ligand exchange. *Physical Chemistry Chemical Physics* **2023**, *25* (28), 19004-19012.

Chapter 4

Temperature-controlled exciton recombination in halide perovskite assemblies

Abstract

Efficient exciton/carrier migration is fundamental for optimizing charge separation, transport, and extraction/recombination processes in solar cells and LEDs. If migration is hindered, excitons may recombine prematurely. In bulk halide perovskites (HPs), carrier lifetimes are significantly high due to strong dielectric screening, which reduces exciton binding energy and enhances carrier mobility and diffusion. These properties make HPs highly promising for optoelectronic applications. However, a large amount of precursor is necessary to prepare bulk perovskite, making them costly. The carriers also need to travel a long path to arrive at the charge transport layer, which increases the chance of radiative and nonradiative recombination. Also, energy loss is caused by photon recycling. Therefore, thin films are necessary which can be easily prepared by PNC assembly formation. Closely packed PNC film provides a less confined structure where excitons can move freely and convert to free carriers with less chance of recombination. In this chapter, I demonstrated exciton diffusion control in $FAPbBr_3$ PQDs by forming assemblies in polymer microenvironments. I also modulated the exciton/carrier recombination dynamics within the assemblies using heat-induced structural changes. A mixture of PQDs and polybutadiene in toluene was drop-casted on the glass cover slip. Polymer shrinkage during drying of the solvent in PQD-polymer film helps to assemble the PQDs which increases exciton lifetime compared to isolated PQDs. This effect is mainly due to the reduction in quantum confinement, caused by enhanced interparticle interactions that increase dielectric screening. As a result, exciton and carrier diffusion within the film is improved. On the other hand, heat-induced polymer expansion increases the particle-to-particle distance between PQDs, which consequently reduces exciton diffusion as well as exciton lifetime. Notably, this structural alteration is partially reversible upon cooling. These tunable properties of PQD assemblies have promising applications in the development of stimuli-responsive switchable optoelectronic devices.

4.1 Introduction

HPs have attracted considerable attention in the last decade as a highly efficient material for lighting and power harvesting technologies.[1-3] The photophysical properties of perovskite materials, including exciton/carrier lifetime, are influenced by several intrinsic and extrinsic factors such as particle size, bandgap, composition, and external environmental conditions.[4-6] Extended carrier/exciton lifetime is necessary for increasing the efficiency of optoelectronic devices.[7, 8] The assembled structure within a film has a much larger exciton lifetime compared to PNCs/PQDs because of the decreased quantum confinement. The assemblies have better mechanical strength, electronic coupling, charge-carrier transport, and stability, compared to isolated PNCs. Moreover, the assembly formation can tune the bandgap[9], emission color[10], morphology, and exciton lifetime[11].

I investigated the defect passivation of $CsPbBr_3$ PNCs using different halide sources in Chapter 3. My initial goal in Chapter 4 was to explore exciton migration and the modulation of carrier recombination under external stimuli in a $CsPbBr_3$ PNC film. However, after preparing a compact film using defect-passivated $CsPbBr_3$ PNCs, I found that exciton/carrier migration was insufficient for the intended study. Therefore, I decided to use $FAPbBr_3$ PQDs instead. Rehman *et al.* reported that $FAPbBr_3$ film exhibits charge-carrier diffusion lengths extending beyond 1 μm, making that a more suitable choice for this investigation.[12] There is a large PL maximal and exciton lifetime shift between the isolated and the self-assembled $FAPbBr_3$ PQDs reported.[10] Previous work in our lab demonstrated ligand-assisted assembly formation of $CsPbBr_3$[13] and $FAPbBr_3$[10] PQDs. $CsPbBr_3$ PNC assemblies showed greater stability against the external stimuli whereas the excitonic recombination of $FAPbBr_3$ PQD assemblies can be tuned under mechanical force. This difference in stability is another reason for selecting $FAPbBr_3$ for this study.

The tunable optoelectronic properties and easy synthesis make perovskites potential for developing next-generation stimuli-responsive devices. [14-17] For example, Zhang *et al.* demonstrated the fabrication of a thermochromic smart window using $CH_3NH_3PbI_3$ perovskite, which modulates luminous transmittance in response to temperature fluctuations.[15] Similarly, Huang *et al.* observed that the PL properties of $CsPb(Cl/Br)_3$ NCs pattern exhibit switchable behavior. The PL is deactivated upon fs

laser irradiation and reactivated through subsequent low-temperature thermal treatment.[18] However, understanding reversible optical property changes achieved by the controlled assembly and disassembling of PNCs using heat is essential for advancing stimuli-responsive device functionality.

A polymer matrix can act as a framework to facilitate the controlled assembly and disassembly of photo-responsive nanomaterials for stimuli-responsive devices. Williams *et al*. demonstrated the self-assembling of silica nanoparticles using polymer into a superlattice which shows switchable properties upon mechanical deformation.[19] Sussman *et al.* fabricated polymer opals by manipulating the core and shell which is transparent at room temperature and undergoes heat-induced color change.[20] Jurewicz *et al.* demonstrated evaporation-driven self-assembly of graphene within a polymer matrix, resulting in switchable optical properties in response to mechanical force or temperature variations.[21] The polymer in the perovskite field is mainly used to enhance stability.[22-25] Some research reported that external stimuli-dependent PL properties change in HP-polymer composites. For instance, Gong *et al.* demonstrated that mechanical stretching in a polymer composite could enhance PL intensity for $CsPbBr_3$ PQDs[26], while Bade *et al.* designed a perovskite LED composed of $MAPbBr_3$ and poly(ethylene oxide) that exhibits stretchability and the ability to withstand significant deformation[27]. In spite of these advancements in HP–polymer composites, the excitonic/carrier recombination processes in HP assemblies within a polymer matrix under stimuli-responsive conditions remain largely unexplored.

In this chapter, I modulated excitonic recombination by making and breaking the $FAPbBr_3$ PQDs assemblies within polybutadiene (PBD) polymer through the application of external heat. PBD is elastic, transparent, and has a very low glass transition temperature (T_g < 210 K). This is why it is chosen as the matrix for PQD assembly formation. The self-assembly of PQDs within the film is facilitated by both solvent evaporation and polymer shrinkage during drying. The as-synthesized small size (ca. 5 nm) PQDs show blue emission at ca. 441 nm which is shifted to ca. 532 nm after self-assembling in PBD. The exciton/carrier lifetime changes from 1.3 ns to 345 nm after assembly formation. Heat-induced expansion of polymers helps partial dissociation of

assembly with a slightly blue-shifted emission peak (from 532 to 530 nm) and a new peak generation at 495 nm. Conversely, cooling the film promotes reassembly formation.

4.2 Results and discussions

4.2.1 PL characteristics of defect-passivated $CsPbBr_3$ PNC films

Excitons are generated upon light absorption by HPs. Efficient exciton migration or diffusion is essential for transporting these excitons to interfaces where they can dissociate into free charges and be collected by the charge transport layer. This migration helps in effective charge collection, reducing recombination losses and increasing device efficiency.

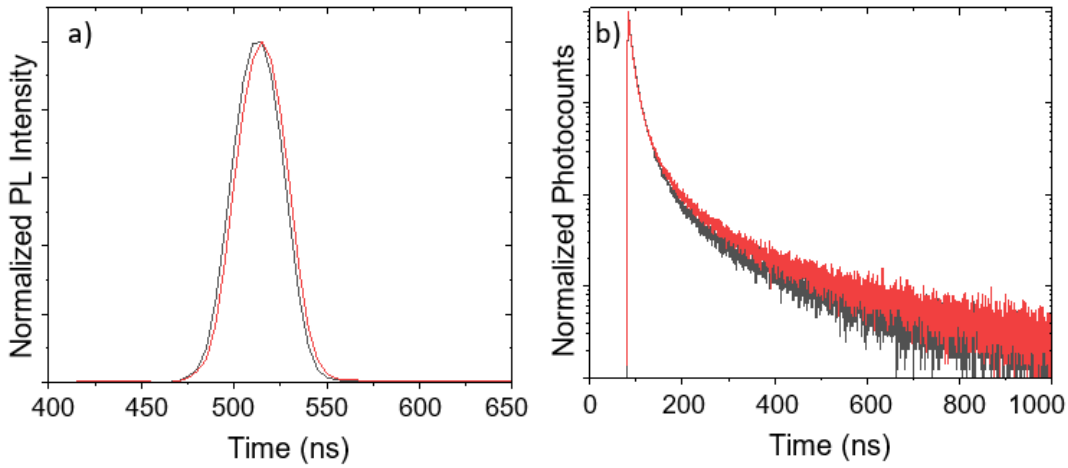

Figure 4.1. PL spectra (a) and PL decay (b) of as-synthesized (black) and NaBr-treated (Red) $CsPbBr_3$ PNC film.

To examine the exciton migration pathways in closely packed $CsPbBr_3$ PNCs film, I centrifuged as-synthesized and defect-passivated $CsPbBr_3$ PNCs at 14,000 rpm for 15 minutes. Then, I collected the precipitate, redissolved it in a minimal amount of toluene, and prepared a film by drop-casting. After fully drying the films, PL spectra and PL lifetime were measured. The PL spectra exhibited a peak around 515 nm for both films, indicating comparable film thickness (Figure 4.1a). However, this spectral shift is minimal when compared to the PL spectra of the isolated PNCs (510 nm). The exciton lifetime of the as-synthesized and NaBr-treated PNC film was 32.5 and 40.6 ns, respectively. The small increase in carrier lifetime upon NaBr treatment suggests a limited impact on exciton lifetime in the film state upon defect passivation. Jiang *et al.* reported

the maximum PL lifetime of a $CsPbBr_3$ PNC film is 44 ns after passivating both surfaces of the film using different polymers.[28] Their perovskite layer thickness was 112 nm. Another article reported the excitonic lifetime of 12.5 ns in $CsPbBr_3$ where the number of perovskite layers is 4.[29] In contrast, Okamoto *et al.* reported the maximum PL lifetime of $CsPbBr_3$ PNC film is >175 ns with film thickness 1.2 μm.[13] However, this higher film thickness is suboptimal for optoelectronic applications. Du *et al.* reported that the performance of HP solar cells started to decrease at 1 sun illumination when the perovskite layer thickened beyond 750 nm.[30] Although an increase in thickness increases light absorption, the exciton has to travel a long path before being extracted.

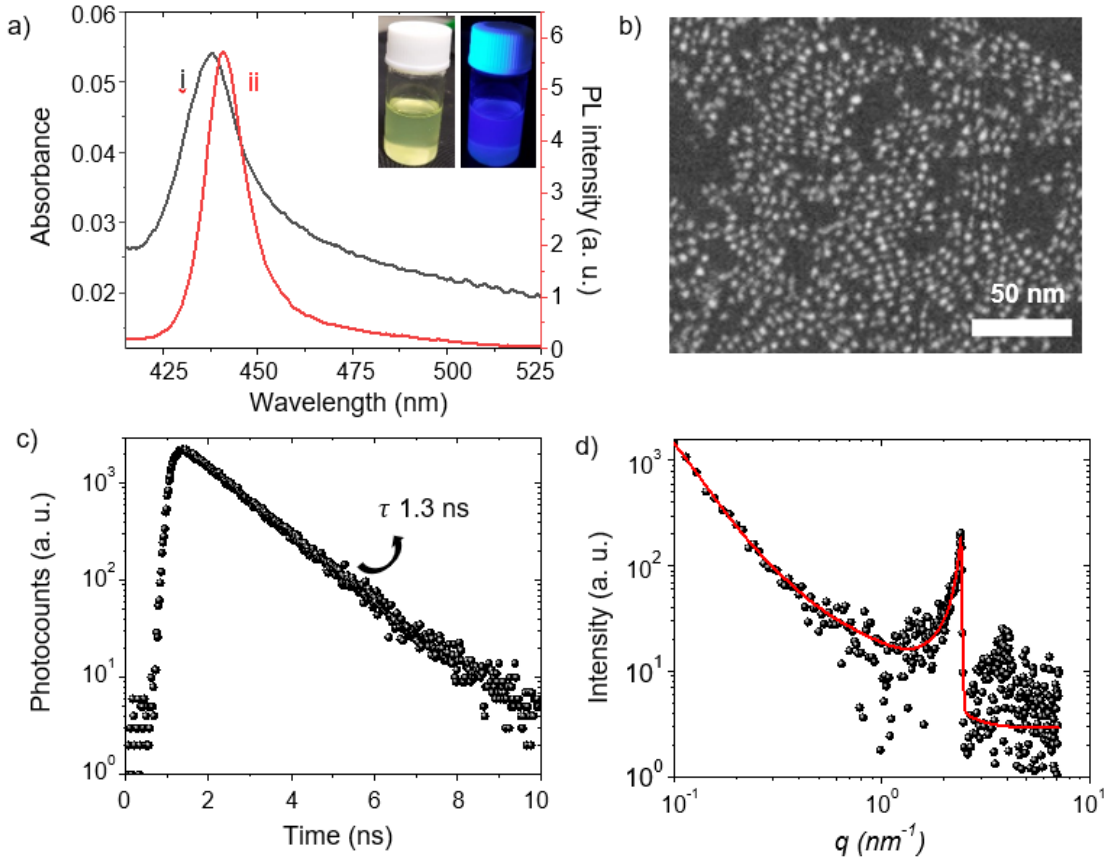

Figure 4.2. Characterization of $FAPbBr_3$ PQDs. Absorption (i) and PL spectra (ii) of the PQDs solution (a). Inset: Images of the PQD colloidal solutions in toluene under daylight and 365 nm UV light. A STEM image of the as-synthesized PQDs (b). PL decay curve of the as-synthesized PQD colloidal solution in toluene (c). SAXS pattern of the as-synthesized PQD film (d).

Therefore, there is a high chance of recombination. Anyway, these reported lifetimes are much shorter than other perovskite film lifetimes.[10, 31] To get longer exciton diffusion length, $FAPbBr_3$ was selected over $CsPbBr_3$ for subsequent experiments in this chapter.

4.2.2 Synthesis and characterization of $FAPbBr_3$ PQDs

$FAPbBr_3$ PQDs were synthesized using a modified hot injection method.[32] Here, oleic acid and n-octylammonium bromide in 1-octadecene were used as a ligand solution, and FABr and $PbBr_2$ in dry DMF were used as precursor a solution. The precursor solution was injected into the ligand solution at 80℃ temperature. The detailed synthesis process is discussed in Chapter 2. This process yielded $FAPbBr_3$ PQDs with a light-yellow color that emits blue light under 365 nm UV excitation (Figure 4.2a inset). The prepared sample exhibits a pronounced excitonic absorption peak at 437 nm and a PL peak at approximately 441 nm attributed to the formation of PQDs (Figure 4.2a). These spectral features indicate strong quantum confinement effects and high exciton binding energy, typically observed in low-dimensional LHPs.[10, 13, 33, 34]

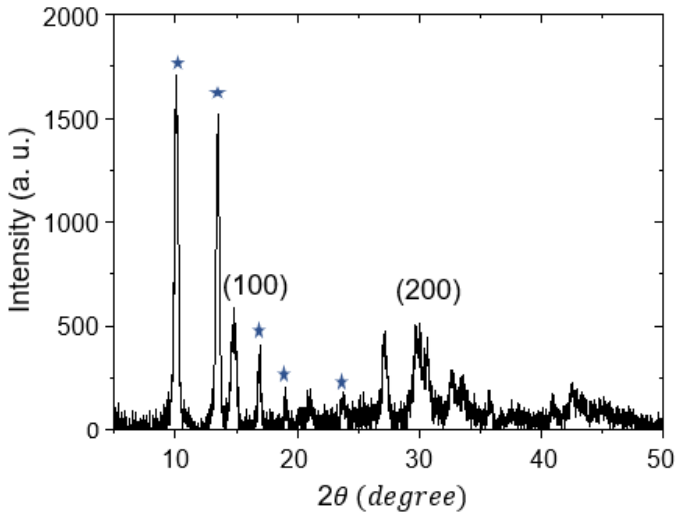

Figure 4.3. XRD of the as-synthesized $FAPbBr_3$ PQD films.

To understand the size, shape, and morphology of the $FAPbBr_3$ PQDs, I performed the STEM. STEM sample was prepared by dispersing a very dilute solution of PQDs in toluene onto a copper grid, followed by overnight drying. As shown in Figure 4.2b, the PQDs are spherical, with an average size of around 5 nm in diameter. The excitonic lifetime was determined through femtosecond (fs) time-resolved single-photon counting

techniques. A 405 nm 150 fs laser pulse was used to excite the PQDs dispersed in toluene. The obtained decay is fitted mono-exponentially. A very short PL lifetime of 1.3 ns is obtained from the as-prepared PQD colloidal solution (Figure 3.4c), that is quite comparable with the lifetimes reported for lead halide PQDs.[10, 35]

SAXS (Figure 4.2d) and XRD (Figure 4.3) analyses were also conducted to confirm the structure of the $FAPbBr_3$ PQDs. Cu Kα (λ = 0.15406 nm) was used as an X-ray source in both procedures. SAXS sample was prepared by drop casting PQDs on Kapton film, whereas the XRD sample was prepared by depositing PQDs on the slide glass. SAXS helps to understand the interparticle distance and dispersity of the PQDs. A sharper peak at 2.4 nm^{-1} indicates a more regular ordering film. The calculated interparticle distance from equation 2.4 is 2.6 nm. The XRD analysis of the $FAPbBr_3$ PQD film reveals diffraction peaks corresponding to the (100) and (200) crystal planes. The other peaks at 10°, 13.5°, and 16.6° are assigned to low dimensional $FAPbBr_3$, as reported by Yuan *et al.* (Figure 4.3).[36] They also revealed that with the increase of dimensionality, these peaks disappear.[36] Qu *et al.* observed that when the size of PQDs is very small, some new diffraction peaks are generated because of the availability of only a few unit cells and the replacement of some FA cation with the ligand.[37]

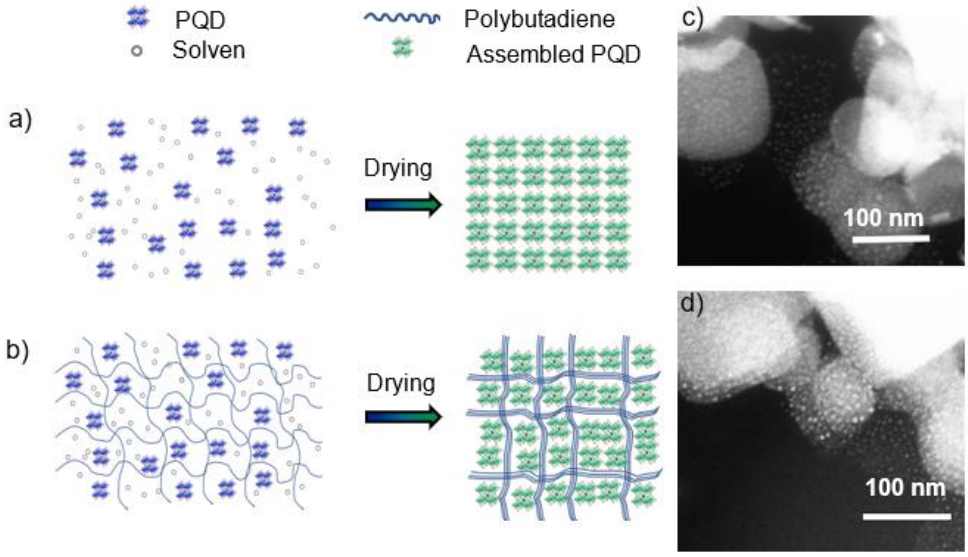

Figure 4.4. Assembly formation within $FAPbBr_3$ PQD-only (a) and PQD-PBD (b) film. (c,d) STEM images of PQD-PBD film.

4.2.3 Optoelectronic properties of $FAPbBr_3$ PQDs and PQD-PBD films

To investigate exciton/carrier migration dynamics, I prepared $FAPbBr_3$ PQD-only and PQD-PBD film using the drop-casting method. A 10 mg/mL solution of PQDs in toluene was used to prepare the PQD-only film. On the other hand, PQD-PBD film was prepared by mixing 10 mg/mL $FAPbBr_3$ PQDs and 25 mg/mL PBD. Both were dissolved in toluene. Therefore, the resulting concentration of PBD was 12.5 mg/mL. A 5 µL sample from this mixture was taken and deposited onto a glass coverslip. During drying when the solvent evaporates, the PQDs are assembled regularly or irregularly in the case of PQD-only film (Figure 4.4a). Sometimes, PQDs formed a close-packed structure which our lab

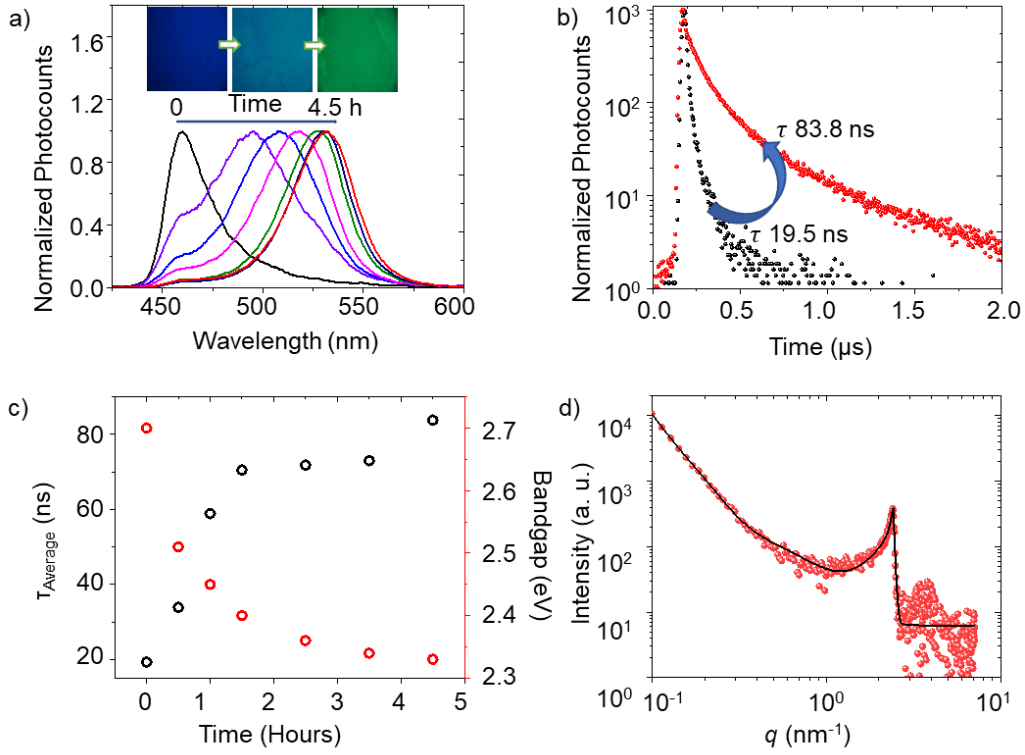

Figure 4.5. (a) PL spectral change observed during the drying process of a PQD–PBD film. Inset: PL images (1.2 mm × 1.2 mm) captured at various stages of drying. (b) PL decay profiles of the PQD–PBD film recorded at (i) the initial stage (0 h) and (ii) after 4.5 h of drying, with excitation at λex = 405 nm. (c) Temporal plots showing PL lifetimes and optical bandgap values of the PQD–PBD film during the drying process. (d) SAXS pattern of the PQD–PBD film.

(Figure 4.4a) previously observed.[10] However, in PQD-PBD film, the polymer chains rearrange and pack more closely together during drying, reducing volume and causing shrinkage. This property helps PQDs come close and assemble in a film (Figure 4.4b).

The STEM images of the thin PQD-PBD film confirm the polymer-induced assembly formation (Figure 4.4c and 4.4d). It is obvious from the STEM images that the small-size PQDs come closer to each other and form a multilayered assembly. The PL color change, PL spectra, and carrier lifetime were measured using the fs laser system to understand the assembly formation in PQD-PBD film. The film's emission color shifted from blue to green accompanied by a redshift in PL from approximately 460 nm to 532 nm over time (Figure 4.5a). Normally, HP platelets, nanowires, and QDs exhibit pronounced quantum confinement effect, leading to absorption and emission bands that are shifted towards shorter wavelengths (blue-shifted) unlike red-shifted emission in large lattices like large PNCs, superlattices, and microcrystals.[38-41]

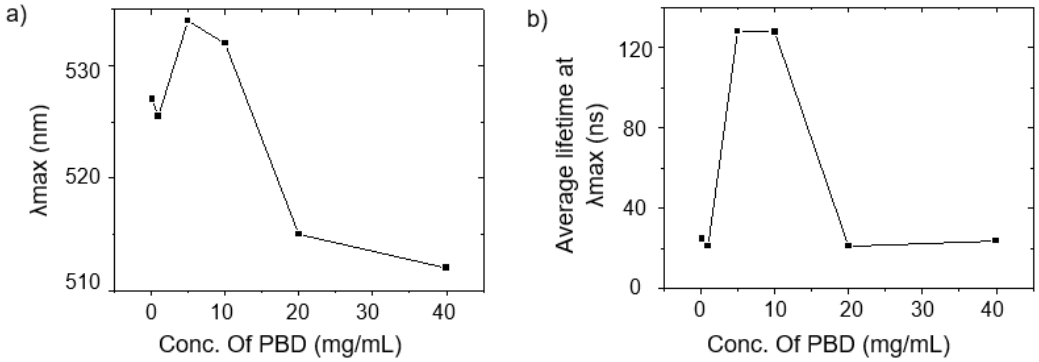

Figure 4.6. Concentration-dependent λmax (a), and average PL lifetime (b) of PQD-PBD film after assembly formation.

Similarly, when such low dimensional HPs self-assemble, the degree of dielectric screening increases which modifies excitonic properties including spectral redshift, miniband formation, and increases in the PL lifetimes.[42] The exciton lifetime of the mixture is increased from 1.3 ns (isolated PQDs) to 19.5 ns (concentrated PQD-PBD mixture) and ultimately 83.8 ns (PQD-PBD film) with time (Figure 4.2c and 4.5b). This redshift and increase in PL lifetime are because of the increased exciton/carrier diffusion and strong dielectric screening.[10, 13, 40, 43] The time-dependent PL lifetime and bandgap change during assembly formation of PQB-PBD film is present in Figure 4.5c. When

particles PQDs are close together, the spatial overlap of electronic wavefunctions increases. This can lead to the broadening of energy levels and, consequently, a narrowing of the bandgap in the assembled structure. In contrast, the carrier lifetime increases over time because, in the assembled structure, the reduction in the quantum confinement effect allows excitons to dissociate into free carriers. The SAXS of the PQD-PBD was also measured, which gives a peak (Figure 4.5d) in the same position as the PQD-only film (Figure 4.2d). The interparticle distance in both films is the same because it is determined by the ligands.

To investigate the PBD concentration-dependent assembly formation rate of PQDs, I monitored the spectral shift of the PQD-PBD film at varying PBD concentrations, as shown in Figure 4.6a. Measurements were taken immediately following film drying using the fs laser system. At very low PBD concentrations (0.2 mg/mL), PQDs spread well along the glass surface, resulting in a larger surface area. This limits effective PBD-mediated assembly, causing some areas to contain isolated PQDs, while others show strong aggregation due to insufficient PBD between them. At moderate PBD concentrations (5-10 mg/mL), dielectric screening is enhanced. However, at higher PBD concentrations, the abundance of PBD between individual PQDs reduces dielectric screening because PBD is a material with low dielectric properties. This is confirmed by a blue shift in emission maxima as well as a shorter PL lifetime (Figure 4.6b).

4.2.4 Temperature-dependent exciton recombination in films

Temperature-dependent PL properties were investigated in both PQD-only and PQD-PBD films to understand the assembly formation mechanism and the influence of temperature on exciton recombination. The films were heated using a micro warm plate KM-1(KITAZATO). The PL spectra and PL decay were recorded at different temperatures using the fs laser system ($\lambda_{ex} = 405\ nm$). Initially, at room temperature (296 K), the assembled PQD-PBD film shows a strong PL peak at 544 nm (Figure 4.7a). The temperature of the film was increased up to 323 K. At 323 K, a shoulder band at 495 nm is generated and the main PL peak at 544 nm undergoes a 14 nm blue shift (Figure 4.7a). on the other hand, the carrier lifetime decreases from 345 ns to 74 ns with increasing temperature (Figure 4.7b). The average PL lifetime of the photons within 440 to 515 nm

is 31 ns and 515 to 570 nm is 76.5 ns. The 31 ns photon represents the isolated PQD formation in PQD-PBD film.

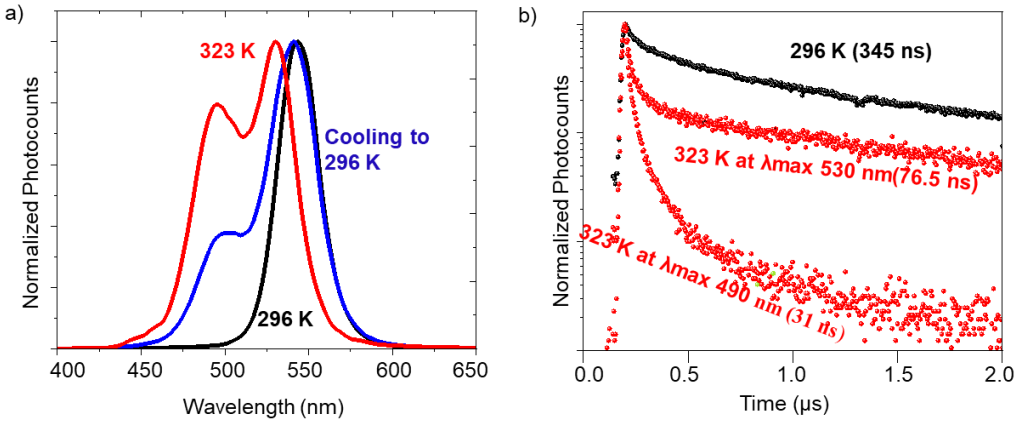

Figure 4.7. (a) PL spectra and (b) PL decays of a dried PQD–PBD film at different temperatures (λex = 405 nm).

In contrast, the spectrum of PQD-only film does not change much when the temperature is increased from 296 to 323 K (Figure 4.8a). I also mechanically dissociated the PQD-only film which shows a large blue shift (Figure 4.8b) of PL spectra. This large blue shift is comparable with the PQD-PBD film blue shift (new peak) at high temperature. Since the PQD-PBD film has a large change compared to other PQD-only films by thermal stimuli, this blue shift of PQD-PBD film can be assigned as the increased interparticle distance due to polymer expansion at high temperature. Consequently, this phenomenon decreases electronic coupling, weakens dielectric screening, and increases the quantum confinements. This observed blue shift in PL for PQD-PBD film opposes the Varshni model. Varshni established a relation of change in semiconductor bandgap with temperature, representing the red shift in semiconductors under thermal influence.[44] Wang *et al.* previously noted a temperature-dependent blue shift in $FAPbBr_3$ PNC films ($\Delta\lambda \sim 7$ nm from 280 K to 320 K), attributed to optical phonon scattering,[45] while Yang *et al.* also demonstrated this effect for $FAPbBr_3$ PNCs, with shifts occurring between 90 K to 350 K due to phase transitions and 290K to 320K due to thermal expansion.[46] Other studies on HP with different cations, such as $MAPbBr_3$ and $CsPbBr_3$, reported smaller blue shifts because of thermal lattice expansion and electron-phonon interactions.[47, 48]

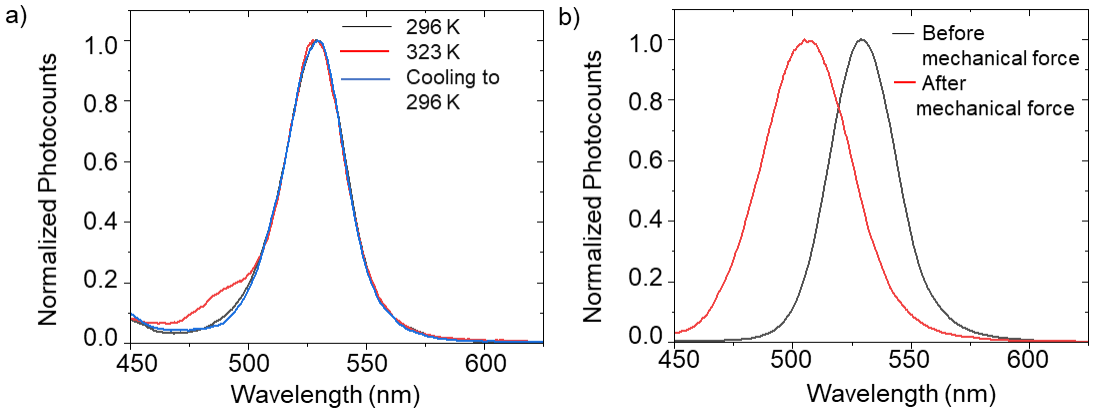

Figure 4.8. a) PL spectra of the PQD-only film at different temperatures. b) PL spectra of PQD-only film before and after applying mechanical forces.

In our study, the small blue shift in the main PL peak (544 to 530 nm) can be explained by temperature-dependent exciton-phonon interactions. However, the more significant 39 nm blue shift as the shoulder band, accompanied by a shorter PL lifetime, indicates that the thermal expansion of the polymer matrix partially disrupts the PQD assemblies. This swelling of the polymer increases the inter-particle distance and weakens dielectric screening. The persistence of green emission at higher temperatures indicates residual assemblies or fused PQDs. I did not increase the temperature further due to concerns regarding potential thermal PL quenching and phase transition. There is no phase transition in $FAPbBr_3$ between 296 K and 323 K. Therefore, these changes are not due to a temperature-induced phase change.[49]

To verify whether PQD assembly formation and dissociation were reversible, I cooled the PQD-PBD film. Cooling the film back to 296 K from 323 K shifts causes the main PL peak to shift from 530 nm to 544 nm, accompanied by a decrease in the intensity of the shoulder band (Figure 4.7a). PL lifetime increasing from 74 to 128 ns (Figure 4.7b). This redshift in PL upon cooling suggests the decrease in electron-phonon coupling in PQD-PBD film. At higher temperatures, the lattice atoms vibrate more intensely, leading to stronger phonon interactions. These vibrations can scatter excitons and electrons, increasing the coupling between them. When the temperature decreases, the amplitude of lattice vibrations reduces, resulting in weaker electron-phonon interactions. Strong electron-phonon coupling at high temperatures leads to spectral broadening and potential

blue-shifted contributions from higher-energy states or phonon-assisted transitions. When coupling diminishes at lower temperatures, such contributions are suppressed, and the PL spectrum shifts towards longer wavelengths dominated by the lower-energy excitonic recombination. Additionally, the reduction in intensity of the new peak and increased PL lifetime suggest PQD reassembly as the polymer matrix contracts. However, complete elimination of the new peak and full restoration of PL lifetime were not achieved, likely due to polymer chains partially obstructing the reassembly of thermally separated PQDs.

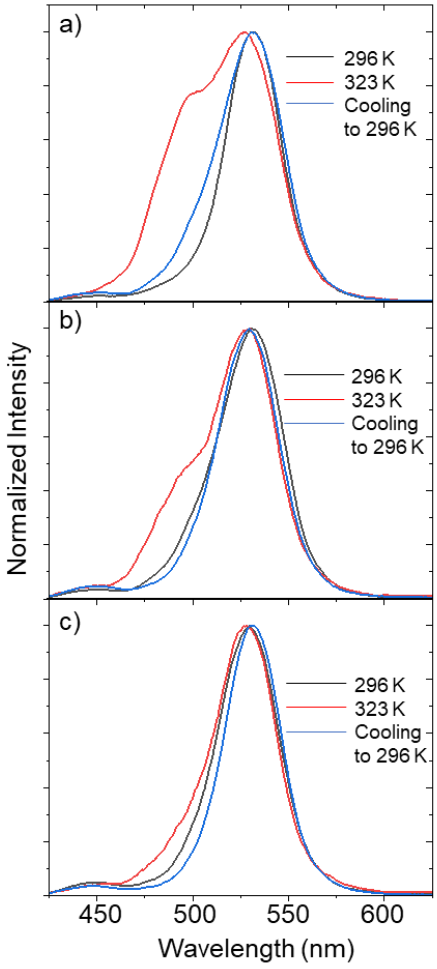

Figure 4.9. Reversibility of temperature-induced spectral changes in the PQD–PBD film across multiple cycles: (a) 1st cycle, (b) 2nd cycle, and (c) 3rd cycle.

This heating and cooling cycle was carried out multiple times to find out the efficiency of this process (Figure 4.9). The results demonstrated that while the spectral changes are reversible several times, the degree of reversibility depends on the ratio of strongly and weekly assembled PQDs. Strongly assembled PQDs, bound more tightly within the

polymer matrix, are more likely to maintain their configuration during thermal

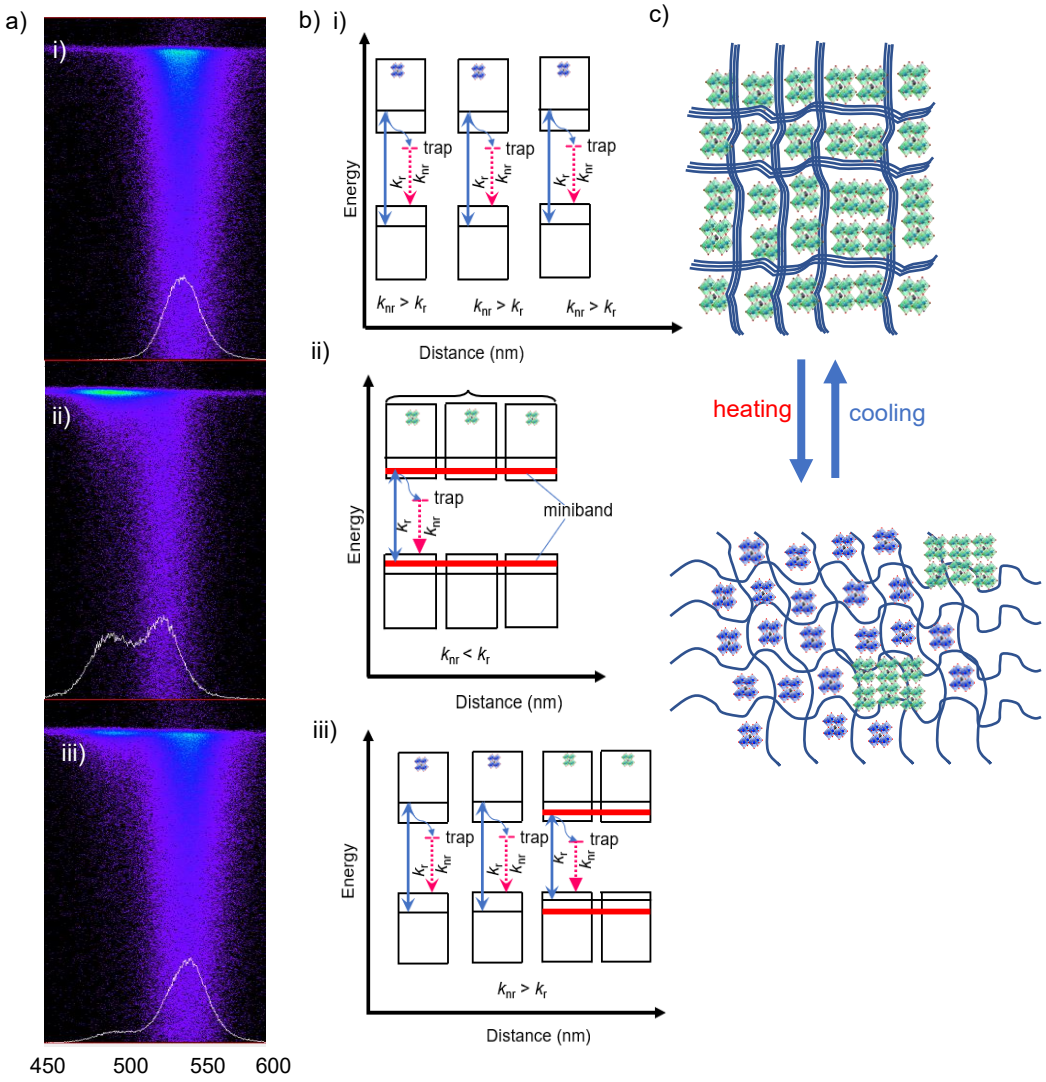

Figure 4.10. (a) Streak camera images of the PQD–PBD film captured at (i) 296 K before heating, (ii) 323 K during heating, and (iii) 296 K after completing the heating and cooling cycle. (b) Schematic representation of energy states, photoexcitation, and relaxation processes in the PQD–PBD film: (i) before assembly formation, (ii) after assembly formation, (iii) after heating, and (ii) after cooling. The diagrams include key parameters such as the nonradiative recombination rate (k_{nr}) and the radiative recombination rate (k_r). (c) Schematic representation of the structural change of PQD–PBD film during the heating and cooling process.

cycling. In contrast, weakly assembled PQDs are more susceptible to external stimuli, leading to deviations in the optical properties.

Temperature fluctuations during these cycles induce thermal expansion and contraction within the PQD–PBD film, generating strain or stress. These strain-induced effects can alter the band structure, leading to changes in excitonic energy levels and optical transitions. While returning the film to its initial temperature reduces the strain, complete reversibility may not occur due to residual stress or structural rearrangements in the material. Additionally, during the annealing process at elevated temperatures, some PQDs may interact more strongly with one another, potentially forming aggregated complexes or clusters. These interactions can alter the local electronic and optical environments of the PQDs, further affecting the reversibility of their spectral behavior.

Finally, I correlated the changes in the structural and optoelectronic properties of the PQD–PBD film during the heating and cooling cycle with the exciton and charge carrier recombination dynamics (Figure 4.10). These correlations provide insights into how thermal effects influence both the physical arrangement of PQDs and their optical behavior. During the formation of PQD assemblies, a redshift in PL emission is observed (Figure 4.10a). This redshift is attributed to the decrease in inter-PQD distances, which enhances the electronic wavefunction overlap between neighboring QDs. Such overlap facilitates the formation of minibands, as described in previous studies of QD superlattices.[50] These minibands allow for extended excitonic states and lower the energy of the emission, manifesting as the observed redshift (Figure 4.10b(ii)).

Additionally, the increased PL lifetime during assembly formation can be linked to a reduction in the surface trap density of the PQDs. Surface traps often act as nonradiative recombination centers, quenching PL and shortening lifetimes.[51] The decreased trap density, combined with enhanced exciton dielectric screening due to the closer proximity of PQDs, results in reduced nonradiative recombination rates. This environment also favors the dissociation of excitons into free carriers, as indicated by the extended PL lifetime reported in similar perovskite systems.[10] In contrast, when the PQD–PBD film is heated, the polymer matrix expands, disrupting the PQD assemblies and increasing the inter-dot distance (Figure 4.10c). This disruption weakens the inter-PQD interactions, diminishing wavefunction overlap and thereby reversing the miniband formation. As a result, the PL emission shifts to higher energies (blue-shifted PL), consistent with the emission from more isolated PQDs. The shorter PL lifetime observed during heating

further supports the notion of weakened PQD interactions. The increased distance between PQDs exposes more surface traps and reduces dielectric screening, leading to a higher rate of nonradiative recombination. However, the incomplete recovery of the spectral features and PL lifetime upon cooling suggests that a fraction of the PQDs remain spatially separated, likely due to the intercalation of polymer chains between them.

4.3 Conclusions

In this chapter, I demonstrated that the exciton migration and recombination in perovskite films can be effectively controlled through the self-assembly formation and dissociation of $FAPbBr_3$ PQDs within PBD polymer matrix. During the drying process, the shrinkage of the polymer matrix brings PQDs into closer proximity, facilitating the formation of organized assemblies. This assembly enhances exciton lifetime by reducing nonradiative recombination and promoting exciton diffusion across the PQD network. It also through increases the dielectric screening. In contrast, thermal stimuli disrupt this organization as polymer expansion during heating separates the PQDs, reducing inter-dot interactions. This separation decreases exciton migration efficiency, as evidenced by the emergence of a new peak at shorter wavelengths in the PL spectrum and a significant reduction in PL lifetime. Although this process exhibits partial reversibility upon cooling, complete recovery of the excitonic properties is hindered by the incomplete reassembly of PQDs, likely due to residual polymer matrix effects. These findings highlight the potential of perovskite-polymer composites as tunable materials for optoelectronic applications, where external stimuli such as temperature can dynamically alter their optical and electronic properties. This controllability paves the way for designing advanced, switchable devices.

References

(1) Kumar, S.; Sharma, V.; Kumari, N.; Kaur, G. A.; Saha, A.; Thakur, S.; Shandilya, M. Recent advances in perovskite materials: exploring multifaceted properties for energy harvesting applications. *Ionics* **2024**, *30* (9), 5159-5188.

(2) Qamar, M. Z.; Khalid, Z.; Shahid, R.; Tsoi, W. C.; Mishra, Y. K.; Kyaw, A. K. K.; Saeed, M. A. Advancement in indoor energy harvesting through flexible perovskite photovoltaics for self-powered IoT applications. *Nano Energy* **2024**, *129*, 109994.

(3) Mondal, S.; Paul, T.; Maiti, S.; Das, B. K.; Chattopadhyay, K. K. Human motion interactive mechanical energy harvester based on all inorganic perovskite-PVDF. *Nano Energy* **2020**, *74*, 104870.

(4) Liu, G.; Kong, L.; Gong, J.; Yang, W.; Mao, H. K.; Hu, Q.; Liu, Z.; Schaller, R. D.; Zhang, D.; Xu, T. Pressure-induced bandgap optimization in lead-based perovskites with prolonged carrier lifetime and ambient retainability. *Advanced Functional Materials* **2017**, *27* (3), 1604208.

(5) Jang, D. M.; Park, K.; Kim, D. H.; Park, J.; Shojaei, F.; Kang, H. S.; Ahn, J.-P.; Lee, J. W.; Song, J. K. Reversible halide exchange reaction of organometal trihalide perovskite colloidal nanocrystals for full-range band gap tuning. *Nano Letters* **2015**, *15* (8), 5191-5199.

(6) Zhou, Q.; Wang, B.; Meng, R.; Zhou, J.; Xie, S.; Zhang, X.; Wang, J.; Yue, S.; Qin, B.; Zhou, H. Understanding temperature-dependent charge extraction and trapping in perovskite solar cells. *Advanced Functional Materials* **2020**, *30* (22), 2000550.

(7) Chen, Y.; Yi, H.; Wu, X.; Haroldson, R.; Gartstein, Y.; Rodionov, Y.; Tikhonov, K.; Zakhidov, A.; Zhu, X.-Y.; Podzorov, V. Extended carrier lifetimes and diffusion in hybrid perovskites revealed by Hall effect and photoconductivity measurements. *Nature Communications* **2016**, *7* (1), 12253.

(8) Yang, X.; Fu, Y.; Su, R.; Zheng, Y.; Zhang, Y.; Yang, W.; Yu, M.; Chen, P.; Wang, Y.; Wu, J. Superior carrier lifetimes exceeding 6 μs in polycrystalline halide perovskites. *Advanced Materials* **2020**, *32* (39), 2002585.

(9) Filip, M. R.; Eperon, G. E.; Snaith, H. J.; Giustino, F. Steric engineering of metal-halide perovskites with tunable optical band gaps. *Nature Communications* **2014**, *5* (1), 1-9.

(10) Zhang, Z.; Ghimire, S.; Okamoto, T.; Sachith, B. M.; Sobhanan, J.; Subrahmanyam, C.; Biju, V. Mechano-optical modulation of excitons and carrier recombination in self-assembled halide perovskite quantum dots. *ACS Nano* **2022**, *16* (1), 160-168.

(11) Yang, Z.; Peng, S.; Lin, F.; Wang, P.; Xing, G.; Yu, L. Self-assembly behavior of metal halide perovskite nanocrystals. *Chinese Journal of Chemistry* **2022**, *40* (18), 2239-2248.

(12) Rehman, W.; Milot, R. L.; Eperon, G. E.; Wehrenfennig, C.; Boland, J. L.; Snaith, H. J.; Johnston, M. B.; Herz, L. M. Charge-carrier dynamics and mobilities in

formamidinium lead mixed-halide perovskites. *Advanced Materials* **2015**, *27* (48), 7938-7944.

(13) Okamoto, T.; Biju, V. Slipping-free halide perovskite supercrystals from supramolecularly-assembled nanocrystals. *Small* **2023**, *19* (32), 2303496.

(14) Wheeler, L. M.; Moore, D. T.; Ihly, R.; Stanton, N. J.; Miller, E. M.; Tenent, R. C.; Blackburn, J. L.; Neale, N. R. Switchable photovoltaic windows enabled by reversible photothermal complex dissociation from methylammonium lead iodide. *Nature Communications* **2017**, *8* (1), 1722.

(15) Zhang, Y.; Tso, C.; Iñigo, J. S.; Liu, S.; Miyazaki, H.; Chao, C. Y.; Yu, K. M. Perovskite thermochromic smart window: Advanced optical properties and low transition temperature. *Applied Energy* **2019**, *254*, 113690.

(16) Liu, S.; Du, Y. W.; Tso, C. Y.; Lee, H. H.; Cheng, R.; Feng, S. P.; Yu, K. M. Thermochromic smart windows: Organic hybrid perovskite ($MAPbI_{3-x}Cl_x$) for thermochromic smart window with strong optical regulation ability, low transition temperature, and narrow hysteresis width (Adv. Funct. Mater. 26/2021). *Advanced Functional Materials* **2021**, *31* (26), 2170186.

(17) Zhumekenov, A. A.; Saidaminov, M. I.; Mohammed, O. F.; Bakr, O. M. Stimuli-responsive switchable halide perovskites: Taking advantage of instability. *Joule* **2021**, *5* (8), 2027-2046.

(18) Huang, X.; Guo, Q.; Kang, S.; Ouyang, T.; Chen, Q.; Liu, X.; Xia, Z.; Yang, Z.; Zhang, Q.; Qiu, J. Three-dimensional laser-assisted patterning of blue-emissive metal halide perovskite nanocrystals inside a glass with switchable photoluminescence. *ACS Nano* **2020**, *14* (3), 3150-3158.

(19) Williams, G. A.; Ishige, R.; Cromwell, O. R.; Chung, J.; Takahara, A.; Guan, Z. Mechanically robust and self-healable superlattice nanocomposites by self-assembly of single-component "Sticky" polymer-grafted nanoparticles. *Advanced Materials (Deerfield Beach, Fla.)* **2015**, *27* (26), 3934-3941.

(20) Sussman, J.; Snoswell, D.; Kontogeorgos, A.; Baumberg, J. J.; Spahn, P. Thermochromic polymer opals. *Applied Physics Letters* **2009**, *95* (17).

(21) Jurewicz, I.; King, A. A.; Shanker, R.; Large, M. J.; Smith, R. J.; Maspero, R.; Ogilvie, S. P.; Scheerder, J.; Han, J.; Backes, C. Mechanochromic and thermochromic sensors based on graphene infused polymer opals. *Advanced Functional Materials* **2020**, *30* (31), 2002473.

(22) Han, T.-H.; Lee, J.-W.; Choi, C.; Tan, S.; Lee, C.; Zhao, Y.; Dai, Z.; De Marco, N.; Lee, S.-J.; Bae, S.-H. Perovskite-polymer composite cross-linker approach for highly-stable and efficient perovskite solar cells. *Nature Communications* **2019**, *10* (1), 520.

(23) Jiang, J.; Wang, Q.; Jin, Z.; Zhang, X.; Lei, J.; Bin, H.; Zhang, Z. G.; Li, Y.; Liu, S. Polymer doping for high-efficiency perovskite solar cells with improved moisture stability. *Advanced Energy Materials* **2018**, *8* (3), 1701757.

(24) Raja, S. N.; Bekenstein, Y.; Koc, M. A.; Fischer, S.; Zhang, D.; Lin, L.; Ritchie, R. O.; Yang, P.; Alivisatos, A. P. Encapsulation of perovskite nanocrystals into macroscale polymer matrices: enhanced stability and polarization. *ACS Applied Materials & Interfaces* **2016**, *8* (51), 35523-35533.

(25) Xin, Y.; Zhao, H.; Zhang, J. Highly stable and luminescent perovskite–polymer composites from a convenient and universal strategy. *ACS Applied Materials & Interfaces* **2018**, *10* (5), 4971-4980.

(26) Gong, Y.; Shen, J.; Zhu, Y.; Yang, X.; Zhang, L.; Li, C. Stretch induced photoluminescence enhanced perovskite quantum dot polymer composites. *Journal of Materials Chemistry C* **2020**, *8* (4), 1413-1420.

(27) Bade, S. G. R.; Shan, X.; Hoang, P. T.; Li, J.; Geske, T.; Cai, L.; Pei, Q.; Wang, C.; Yu, Z. Stretchable light-emitting diodes with organometal-halide-perovskite–polymer composite emitters. *Advanced Materials* **2017**, *29* (23), 1607053.

(28) Jiang, L.; Fang, Z.; Lou, H.; Lin, C.; Chen, Z.; Li, J.; He, H.; Ye, Z. Achieving long carrier lifetime and high optical gain in all-inorganic $CsPbBr_3$ perovskite films via top and bottom surface modification. *Physical Chemistry Chemical Physics* **2019**, *21* (39), 21996-22001.

(29) Wang, R.; Jia, Y.-L.; Ding, L.; He, Z.; Dong, Y.; Ma, X.-J.; Zhang, Y.; Zhou, D.-Y.; Zhu, Z.-X.; Xiong, Z.-H. Efficient halide perovskite light-emitting diodes with emissive layer consisted of multilayer coatings. *Journal of Applied Physics* **2019**, *126* (16).

(30) Du, T.; Xu, W.; Xu, S.; Ratnasingham, S. R.; Lin, C.-T.; Kim, J.; Briscoe, J.; McLachlan, M. A.; Durrant, J. R. Light-intensity and thickness dependent efficiency of planar perovskite solar cells: charge recombination versus extraction. *Journal of Materials Chemistry C* **2020**, *8* (36), 12648-12655.

(31) Zhang, Y.; Liang, Y.; Wang, Y.; Guo, F.; Sun, L.; Xu, D. Planar $FAPbBr_3$ solar cells with power conversion efficiency above 10%. *ACS Energy Letters* **2018**, *3* (8), 1808-1814.

(32) Khatun, M. F.; Okamoto, T.; Biju, V. Self-assembled halide perovskite quantum dots in polymer thin films showing temperature-controlled exciton recombination. *Chemical Communications* **2023**, *59* (93), 13831-13834.

(33) Gélvez-Rueda, M. C.; Fridriksson, M. B.; Dubey, R. K.; Jager, W. F.; Van der Stam, W.; Grozema, F. C. Overcoming the exciton binding energy in two-dimensional perovskite nanoplatelets by attachment of conjugated organic chromophores. *Nature Communications* **2020**, *11* (1), 1901.

(34) Tao, W.; Zhou, Q.; Zhu, H. Dynamic polaronic screening for anomalous exciton spin relaxation in two-dimensional lead halide perovskites. *Science Advances* **2020**, *6* (47), eabb7132.

(35) Park, S.; Cho, H.; Choi, W.; Zou, H.; Jeon, D. Y. Correlation of near-unity quantum yields with photogenerated excitons in X-type ligand passivated $CsPbBr_3$ perovskite quantum dots. *Nanoscale Advances* **2019**, *1* (8), 2828-2834.

(36) Yuan, Z.; Shu, Y.; Xin, Y.; Ma, B. Highly luminescent nanoscale quasi-2D layered lead bromide perovskites with tunable emissions. *Chemical Communications* **2016**, *52* (20), 3887-3890.

(37) Qu, R.; Gao, M.; Li, H.; Qi, X.; Liu, C.; Zhao, W.; Yan, J.; Zhang, Z. Hydrobromic acid-assisted size control of formamidinium lead bromide perovskite quantum dots at room temperature. *Optical Materials* **2021**, *113*, 110776.

(38) Zhang, F.; Yang, B.; Zheng, K.; Yang, S.; Li, Y.; Deng, W.; He, R. Formamidinium lead bromide ($FAPbBr_3$) perovskite microcrystals for sensitive and fast photodetectors. *Nano-Micro Letters* **2018**, *10*, 1-8.

(39) Tang, X.; Khurana, M.; Rossi, D.; Luo, L.; Akimov, A. V.; Son, D. H. Exciton photoluminescence of strongly quantum-confined formamidinium lead bromide ($FAPbBr_3$) quantum dots. *The Journal of Physical Chemistry C* **2022**, *126* (43), 18366-18373.

(40) Sachith, B. M.; Okamoto, T.; Ghimire, S.; Umeyama, T.; Takano, Y.; Imahori, H.; Biju, V. Long-range interfacial charge carrier trapping in halide perovskite-C_{60} and halide perovskite-TiO_2 donor–acceptor films. *The Journal of Physical Chemistry Letters* **2021**, *12* (35), 8644-8651.

(41) Liu, Y.; Siron, M.; Lu, D.; Yang, J.; Dos Reis, R.; Cui, F.; Gao, M.; Lai, M.; Lin, J.; Kong, Q. Self-assembly of two-dimensional perovskite nanosheet building blocks into ordered Ruddlesden–Popper perovskite phase. *Journal of the American Chemical Society* **2019**, *141* (33), 13028-13032.

(42) Bi, C.; Wang, S.; Kershaw, S. V.; Zheng, K.; Pullerits, T.; Gaponenko, S.; Tian, J.; Rogach, A. L. Spontaneous self-assembly of cesium lead halide perovskite nanoplatelets into cuboid crystals with high intensity blue emission. *Advanced Science* **2019**, *6* (13), 1900462.

(43) Ghimire, S.; Takahashi, K.; Takano, Y.; Nakamura, T.; Biju, V. Photon recycling by energy transfer in piezochemically synthesized and close-packed methylammonium lead halide perovskites. *The Journal of Physical Chemistry C* **2019**, *123* (45), 27752-27758.

(44) Varshni, Y. P. Temperature dependence of the energy gap in semiconductors. *Physica* **1967**, *34* (1), 149-154.

(45) Wang, X.; Wang, Q.; Chai, Z.; Wu, W. The thermal stability of $FAPbBr_3$ nanocrystals from temperature-dependent photoluminescence and first-principles calculations. *RSC Advances* **2020**, *10* (72), 44373-44381.

(46) Yang, L.; Wei, K.; Xu, Z.; Li, F.; Chen, R.; Zheng, X.; Cheng, X.; Jiang, T. Nonlinear absorption and temperature-dependent fluorescence of perovskite $FAPbBr_3$ nanocrystal. *Optics Letters* **2017**, *43* (1), 122-125.

(47) Woo, H. C.; Choi, J. W.; Shin, J.; Chin, S.-H.; Ann, M. H.; Lee, C.-L. Temperature-dependent photoluminescence of $CH_3NH_3PbBr_3$ perovskite quantum dots and bulk counterparts. *The Journal of Physical Chemistry Letters* **2018**, *9* (14), 4066-4074.

(48) Li, J.; Yuan, X.; Jing, P.; Li, J.; Wei, M.; Hua, J.; Zhao, J.; Tian, L. Temperature-dependent photoluminescence of inorganic perovskite nanocrystal films. *RSC Advances* **2016**, *6* (82), 78311-78316.

(49) Mannino, G.; Deretzis, I.; Smecca, E.; La Magna, A.; Alberti, A.; Ceratti, D.; Cahen, D. Temperature-dependent optical band gap in $CsPbBr_3$, $MAPbBr_3$, and $FAPbBr_3$ single crystals. *The Journal of Physical Chemistry Letters* **2020**, *11* (7), 2490-2496.

(50) Imran, A.; Jiang, J.; Eric, D.; Zahid, M. N.; Yousaf, M.; Shah, Z. Optical properties of InAs/GaAs quantum dot superlattice structures. *Results in Physics* **2018**, *9*, 297-302.

(51) Merdasa, A.; Tian, Y.; Camacho, R.; Dobrovolsky, A.; Debroye, E.; Unger, E. L.; Hofkens, J.; Sundstrom, V.; Scheblykin, I. G. "Supertrap" at work: extremely efficient nonradiative recombination channels in $MAPbI_3$ perovskites revealed by luminescence super-resolution imaging and spectroscopy. *ACS Nano* **2017**, *11* (6), 5391-5404.

Chapter 5

Carrier extraction at the perovskite carbon nanotube interfaces

Abstract

In halide perovskite (HP) solar cells (PSCs), sunlight generates electron-hole pairs (charge carriers) within the perovskite layer. These charge carriers must be extracted quickly to minimize recombination losses and ensure efficient power generation. Band-edge electron extraction is a fundamental process in solar cells, causing intra-band relaxation or internal conversion-assisted energy loss in the form of heat. Therefore, extraction of hot carriers (HCs) is crucial for improving solar cell power conversion efficiency (PCE). The HC extraction can be accomplished by modulating their relaxation dynamics using an acceptor. The kinetics of carrier relaxation in these types of donor-acceptor hybrid systems remain an active area of investigation and debate, with essentially no ideal solution for HC extraction at the HP electron transport layer interface. In this chapter, I used multiwall carbon nanotubes (MWCNTs) as a carrier extractor and transporter for as-synthesized $CsPbBr_3$ PNCs. To produce an intimate interface between $CsPbBr_3$ PNCs and MWCNTs, I first functionalized the MWCNT with phenylamine (MWCNT-NH_2). The PNC-MWCNT conjugates were prepared by post-mixing of PNCs with functionalized MWCNT or following the in situ hot injection method. MWCNTs are anchored with a sub-monolayer of PNCs in the post-mixing method, whereas the in situ method yields MWCNTs coated with dense PNC layers. The PL lifetime of the conjugates was measured to investigate the excited-state carrier dynamics. A reduction in PL lifetime observed in both post-mixing and in situ synthesized conjugates compared to individual PNC dots and PNC films, respectively, suggests charge or energy transfer occurring at the interface within the conjugates. To further elucidate the dynamics of photogenerated charge carriers, transient absorption (TA) spectroscopy was performed. TA result shows the slow intra-band relaxation of HCs in PNC-MWCNT conjugates (320 fs) compared to PNC-only (250 fs), showing HC transfer. It also reveals the predominance of nonradiative Auger recombination (AR) in PNC-only sample because of the high carrier density at the band edge which is suppressed in PNC-MWCNT conjugates due to HCs transfer occurring before relaxation to the band edge. Moreover, the shortening of the slowest component in bleach recovery kineties for the PNC-MWCNT conjugates compared to PNC-only shows band-edge electron or energy transfer. These conjugates have significant potential for fabricating devices with enhanced efficiency.

5.1 Introduction

HPs are semiconducting materials, that hold significant potential in meeting the energy demands of a modern, sustainable society due to their exceptional optoelectronic properties and versatility.[1, 2] While they are best known for their application in solar cells, they are also used in LEDs, lasers, and various other optoelectronic devices.[3] Their unique photophysical characteristics, including high absorption coefficients, long carrier diffusion lengths, and tunable bandgaps, make them ideal for these applications.[4, 5] Upon absorbing sunlight, the HP layer in solar cells generates electron-hole pairs.[6] These photogenerated electrons are captured by the electron transport layer (ETL) and holes are captured by the hole transport layer (HTL) before recombination.[6] The efficiency of a particular solar cell depends on the successful extraction of these photogenerated charge carriers. Several photophysical processes including radiative carrier recombination, nonradiative AR, and charge carrier trapping in defects compete with efficient carrier harvesting.[7-9] Various approaches such as surface passivation, bandgap engineering, ligand engineering, and doping are employed to address these issues.[10-12] These approaches are primarily used to enhance stability, optimize band alignment, and improve surface properties to reduce recombination at the material's surface. However, such treatments can sometimes act as insulators (e.g., polymer encapsulation), hindering charge transport and ultimately reducing device efficiency. This approach doesn't offer comprehensive performance enhancement, especially in devices where charge generation, separation, and transport are central to performance. Therefore, along with decreasing recombination loss, incorporating materials that efficiently extract and transport carriers to the charge transport layer is advantageous.

Band edge carrier extraction using an acceptor molecule is widely investigated in LHPs. However. Although band-edge carrier extraction increases the PCE of PSCs, it relies on carriers cooling to the band edges before extraction, leading to significant energy loss through thermalization. HC extraction offers significant advantages over conventional band-edge carrier extraction. Here carriers are captured by the acceptor before they thermalize to the band edges, preserving their excess kinetic energy. HC extraction is crucial for overcoming the theoretical limit of solar cell efficiency.[13-15] In perovskites, HCs are generated when the material is excited with energy greater than its bandgap.[15] Upon thermalization, HCs lose energy to return band edge mainly by emitting longitudinal-optical phonons, which are high-energy lattice vibrations.[15, 16] This thermalization process is one of the loss mechanisms of PSCs.[14] To overcome this problem understanding the HC dynamic as well as combining

perovskite with a material having fast charge extraction and transport capability is a promising approach.

There are various carrier acceptors reported in the literature.[17, 18] When a perovskite binds with these acceptor molecules, the hybrid donor-acceptor systems exhibit synergistic effects by fine-tuning physical, chemical, and electronic properties. Our lab investigated the photoinduced charge transfer between HPs and different acceptors including TCNQ, TCNB, and fullerene.[19, 20] On the other hand, Nagal *et al.* investigated the HC kinetics in a $CsPbBr_3$/ZnO heterojunction. Their results revealed suppressed excitonic recombination and enhanced carrier transfer at the interface, which consequently increased the photodetector's responsivity.[21] Maity *et al.* reported charge carrier dynamics in the perovskite-organic molecular composite. They claimed both electron and hole transfer at $CsPbBr_3$ PQDs and 4,5-dibromofluorescein complex.[22] Jesús Jiménez-López *et al.* reported the use of C60 to improve the HC extraction and collection.[23] Combining HPs with carbon nanotubes (CNTs) can be one of the choices for increasing carrier lifetime because CNTs have exceptional charge carrier properties. Moreover, CNT has high mechanical strength, which enables it to serve as a template for HPs and enhance the overall stability of the system. Several research articles have demonstrated that the incorporation of CNT enhances charge transfer efficiency. For example, Nian Cheng *et al.* demonstrated that MWCNT on $CH_3NH_3PbI_3$ PNCs function as a carrier transport highway, facilitating hole movement between PNCs and thereby, extending carrier lifetime. As a result, the PCE increased by approximately 15% compared to solar cells without MWCNTs.[24] In contrast, Dan Li *et al.* reported the introduction of amino-functionalized carbon nanotubes (CNT-NH_2) as crystal growth templates. They claimed that NH_2-CNT successfully passivates the defects and adjusts the energy band alignment, creating a faster carrier transport route that accelerates the extraction and transfer of electrons.[25] For further increasing device performance in HP-CNT composite, understanding the HC lifetime and hot-carrier deactivation mechanism is crucial, which remains a topic of controversy. Extensive research is needed to unravel this mystery.

In this study, I investigated the HC extraction from PNCs. HC lifetime is very short and HC transfer occurs in femto- to pico-second level.[26, 27] Therefore, I selected MWCNT as HC acceptor and transport mediators due to their exceptional charge transport properties. MWCNT functionalized with terminal phenylamine group used as a template for binding with $CsPbBr_3$ PNCs. Post-mixing and in situ hot injection methods were used to prepare these conjugates.

The strong interaction between the -NH_2 groups and the PNCs ensures a robust attachment of MWCNTs to the PNCs which opens a route for carrier transfer from PNC to MWCNT. A reduction in carrier lifetime in PNC-MWCNT conjugates compared with PNC-only samples confirms the decrease in radiative recombination, which indicates the carrier or energy transfer at the interface. Furthermore, TA spectroscopy reveals that in the presence of MWCNTs, HC relaxation to the band edge is suppressed which favors the transition of HCs from PNC to MWCNT. This transition reduces intra-band non-radiative AR which is predominant in the absence of MWCNT.

5.2 Results and discussions

5.2.1 Characterization of functionalized MWCNTs

The commercial MWCNT was functionalized through a two-step reaction process. Initially, the MWCNTs were treated with 4-nitrobenzenediazonium tetrafluoroborate at approximately 150°C. At this elevated temperature, the diazonium salt undergoes thermal decomposition to generate highly reactive nitrobenzene free radicals. These free radicals readily interact with the MWCNT surface, forming covalent bonds. Subsequently, the nitro functional groups introduced onto the MWCNT surface were reduced to amino groups by reacting with sodium borohydride ($NaBH_4$) in dimethyl sulfoxide (DMSO). As a result, the final functional group covalently attached to the MWCNT surface was phenylamine. The amino group is chosen as a terminal functional group since it can strongly bind to PNCs.[28] The reaction scheme and detailed synthesis procedure are shown in Chapter 2.

The STEM of MWCNT-NH_2 was measure to confirm the structural integrity of nanotubes after reaction at high temperature. The STEM sample was prepared by drop casting a dilute solution of MWCNT-NH_2 in acetone onto a STEM grid, followed by drying overnight. Figure 5.1a shows the STEM image of MWCNT-NH_2. To confirm the successful functionalization of MWCNT, X-ray Photoelectron Spectroscopy (XPS), Raman Spectroscopy, and Fourier Transform Infrared Spectroscopy (FTIR) were measured. The surface chemical composition of pristine MWCNT and MWCNT-NH_2 were investigated using XPS. In the carbon region, both samples exhibit a peak at 284.1 eV, corresponding to graphitic sp^2-hybridized carbon (Figures 5.1b and 5.1c).[29, 30] In addition to this peak, the MWCNT-NH_2 sample displayed another peak at 285.5 eV which originated from a defect site on the nanotube, indicating sp^3 hybridization[29, 30] (Figure 5.1c). The predominance of the 285.5 eV peak in MWCNT-NH_2 confirms successful functionalization. This is because pristine MWCNTs are predominantly composed of sp^2-

hybridized carbon atoms, which form the conjugated π-electron system responsible for their exceptional electrical, mechanical, and optical properties. Functionalization typically involves covalent bonding between the nanotube's carbon atoms and external chemical groups. This covalent bonding requires some sp^2-hybridized carbons in the nanotube's hexagonal lattice to transition to sp^3 hybridization, breaking the conjugated π system locally. The peak at 291.3 eV corresponds to the π-π* transition, as previously reported.[29, 31] In the nitrogen region, a distinct N1s peak (399.6 eV)[32] is observed exclusively in the MWCNT-NH_2 sample, while it was absent in the non-functionalized MWCNT (Figure 5.1d) confirming the presence of N in a functionalized nanotube. Ramanathan *et al.* reported that the N1s peak for terminal primary amine-functionalized CNT appears approximately in that binding energy region.[33] Both non-functionalized and functionalized samples display an O1s peak centered at 533 eV (Figure 5.1e and 5.1f), which is reported to be unintentionally incorporated into the CNT during purification or upon exposure to environmental oxidants.[34] The increase in O1s peak intensity in the MWCNT after functionalization can be attributed to the more surface oxidation or introduction of some oxygen-containing functional groups to the surface.

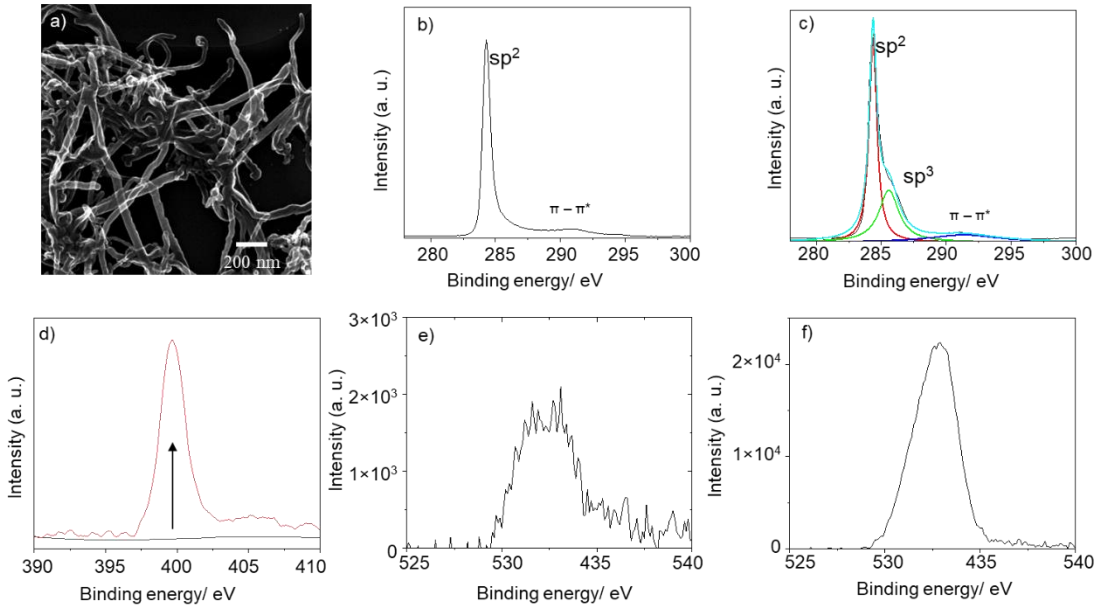

Figure 5.1. STEM image of MWCNT-NH_2 (a). XPS spectra of carbon region (C1s) for the (b) MWCNT, (c) MWCNT-NH_2, nitrogen region (N1s) for the (black) MWCNT and (Red) MWCNT-NH_2 (d), and oxygen region (O1s) for the MWCNT (e) and MWCNT-NH_2 (f).

Raman spectroscopy is also a powerful tool for characterizing MWCNT which can provide information about their structural properties, defect density, and functionalization

status. Samples are prepared by drop casting the concentrated MWCNT and MWCNT-NH_2 in acetone on the glass cover slip followed by vacuum drying. Raman spectra of pristine MWCNT and MWCNT-NH_2 are presented in Figure 5.2a in a range 500-3500 cm^{-1}. The 2 main peaks arise from first-order scattering mode: D peak at 1338.7 cm^{-1} and the G peak at 1569 cm^{-1}. The G peak arises from the in-plane stretching vibration of sp^2-bonded carbon atoms from MWCNT carbon sheet, whereas the D peak is a disorder-induced feature that arises from the in-plane breathing vibration of sp^2 carbon rings, activated by the presence of defects.[35] The G and D bands are associated with the E_{2g} and A_{1g} phonon mode at the Brillouin zone respectively.[36] The intensity ratio of the D to G peak (I_D/I_G) serves as a useful indicator to understand the degree of defects introduced to the MWCNT upon chemical processing.[32] The increased ratio of I_D/I_G, in the case of MWCNT-NH_2 (0.73) compared with MWCNT (0.53) provides strong evidence of successful functionalization of carbon nanotube. The conversion of sp^2 hybridized carbons to sp^3 hybridization due to functionalization creates a three-dimensional bonding geometry, introducing defects or distortions in the planar or tubular sp^2 lattice. This phenomenon is responsible for the increase in the intensity of D peak.

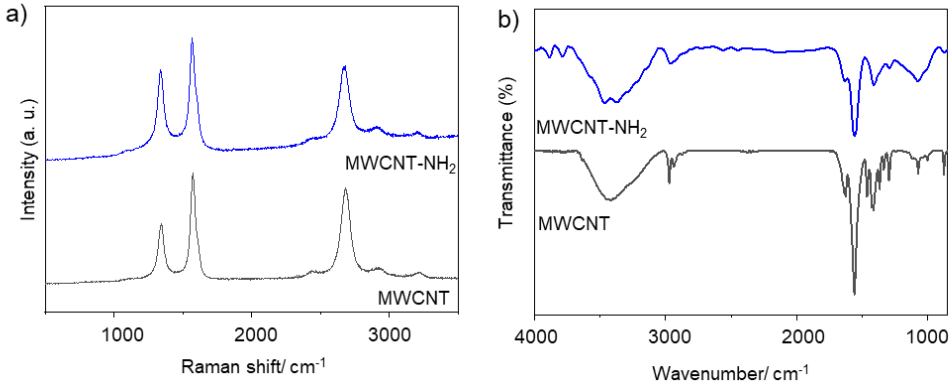

Figure 5.2. Raman (a) and FTIR (b) spectra of MWCNT and MWCNT-NH_2.

To investigate the exact functional group on the modified MWCNTs, I performed the FTIR, which is presented in Figure 5.2b. The strong board peak between 3000-3700 cm^{-1} in the MWCNT is assigned for the O-H stretching. This peak is commonly associated with hydroxyl groups, which can originate from carbonyl groups or adsorbed water. As previously discussed, the O-H peak observed in the MWCNT may result from the oxidation of the nanotubes during the manufacturer's purification process, which often involves exposure to oxidative environments.[37] In contrast, MWCNT with phenylamine functional groups, shows a new peak in the same region (3000–3700 cm^{-1}), which is attributed to the N-H stretching

vibration of primary amines. This distinct peak is indicative of the successful attachment of phenylamino groups to the nanotube surface. A similar splitting and peak pattern have been reported by Chen *et al.* and Chinh *et al.* in the presence of -NH_2 groups.[32, 38] Additionally, the peak between 2973 cm^{-1} corresponds to C-H stretching.[39] Another prominent feature is the peak around 1627 cm^{-1}, which is associated with the C=C stretching vibration, indicative of the presence of the conjugated carbon-carbon bonds that are characteristic of the CNT structure.[39] Peak at 1560 cm^{-1} is for the cylindrical graphene sheet.[40] All the above characterization results confirm the successful functionalization of MWCNT surface.

5.2.2 MWCNT-PNC conjugate formation

$CsPbBr_3$ PNCs were used for MWCNT-PNC conjugate formation. PNCs were synthesized following the previously reported hot injection method,[41] where oleic acid and hexadecyl anime are used as ligands. The synthesis procedure is explained in chapter 2. Figure 3.1a shows the absorption and PL spectra of the as-synthesized $CsPbBr_3$ PNCs. The absorption and emission peaks in toluene are observed at 501 nm and 510 nm, respectively. These light-yellow PNCs emit green light (Figure 3.1inset) when excited under 365 nm UV light. The synthesized PNCs are cubic and the size is approximately 7.12±0.96 nm (Figure 3.1b and Figure 3.1c) which is similar as previously reported.[41] I prepared the PNC-MWCNT conjugates by two processes.

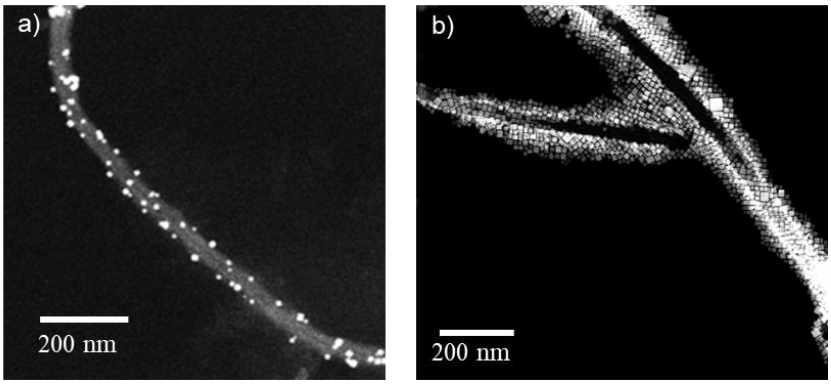

Figure 5.3. STEM image of the conjugates prepared by post-mixing method (a), and following in situ hot injection synthesis procedure (b).

The first involves post-mixing the as-synthesized PNCs with MWCNT-$NH_3^+Br^-$ in a toluene THF mixture (9:1). In this process, THF is used to decrease the aggregation of MWCNT-$NH_3^+Br^-$ in toluene. MWCNT-NH_2 is converted to MWCNT-$NH3^+Br^-$ (detail process is presented in Chapter 2) before adding PNC in the post-mixing conjugate formation method to stabilize the heterogeneous system. This can also act as an extra bromide source.[42] Yan *et al.* reported that ammonium salts can more effectively coordinate with both surface

cations and anions of PNCs compared to amine ligands, while also aiding in the passivation of surface defects.[43] Similarly, Kazes *et al.* report the strong binding of ammonium with perovskite surface compared to carboxylate ligand by occupying the Cs^+ position. [44] After two days the nanotubes are collected by centrifugation and redispersed in the same ratio of solvents.

Another process of MWCNT-PNC conjugate formation is the hot injection method where MWCNT-NH_2 was used as a ligand along with oleic acid and hexadecyl amine (details provided in chapter 2). In this process, the hot Cs-precursor was injected into the Pb precursor containing functionalized MWCNT. A similar hot injection method for the growth of PNCs on the nanotube surface was reported by Lee *et al.* recently.[45] Their study demonstrated that the surface of the CNTs can effectively serve as a nucleation center for the crystallization and growth of PNCs, providing a template that promotes uniform crystal formation. In our work, I employed a similar hot injection technique, with modifications, such as temperature, precursor concentrations, and solvent composition. The amino groups (-NH_2) on the nanotube surface are expected to play a critical role in facilitating nucleation by providing anchoring sites for the PNC precursors, thereby enhancing their local concentration and promoting crystal growth. The conjugation by post-mixing and in situ synthesis schemes are illustrated in Figures 2.4 and 2.5, respectively.

The conjugation formation is confirmed by STEM imaging, which is presented in Figures 5.3a and 5.3b. Almost no size change of PNC was observed after mixing with functionalized MWCNT. On the other hand, the size of in situ synthesized conjugates is 8.69 ± 1.34 nm, slightly larger than the PNC-only sample. The increase in PNC size with MWCNT is previously reported by Lee *et al*.[45] They reported variations in particle shape and size depending on the injection temperature. At an injection temperature of 170°C, the cubic PNC size increases from 14.6 to 21 nm in the presence of MWCNT.[45] In our case, the PNC size increase is minor compared to their PNC size increase. This can be attributed to the functionalization of our MWCNTs with terminal -NH_2 groups, which facilitates further binding to the PNC surface and likely inhibits crystal growth. A submonolayer of PNC around the carbon nanotube is achieved in the post-mixing method (Figure 5.3a) by mixing very diluted PNC with functionalized MWCNT. However, multilayer PNCs are formed around the CNT (Figure 5.3b) in the case of in situ prepared conjugates which is similar to the previous report.[45] This multilayer formation can be attributed to dipole-dipole interactions between the PNCs, which promote their self-assembly into layered structures around CNT.[46]

5.2.3 Optoelectronic properties of the conjugates

The absorption and PL spectra of the post-mixing and in situ prepared conjugates were investigated to understand the effect of MWCNT on the optical properties of PNC which are presented in Figure 5.4a and Figure 5.4b respectively. These spectra were measured in toluene. The excitation wavelength was 365 nm. The excitonic absorption peaks are observed at 502 nm and 505 nm, while the PL peaks are observed at 511 nm and 513.5 nm for the post-mixing and in situ synthesized samples, respectively. No significant shift in the absorption and PL peak positions for the post-mixing sample are observed when compared to the PNC-only sample, indicating no change in the band structure. However, the redshift in both absorption and PL peaks in the in situ prepared conjugate, compared to the PNC-only sample, is attributed to the formation of a multilayer of PNC around the MWCNT. The inset of Figure 5.4b shows images of the in situ prepared conjugates under daylight and 365 nm UV excitation. The daylight image of in situ synthesized conjugates is greenish compared to the PNC-only sample.

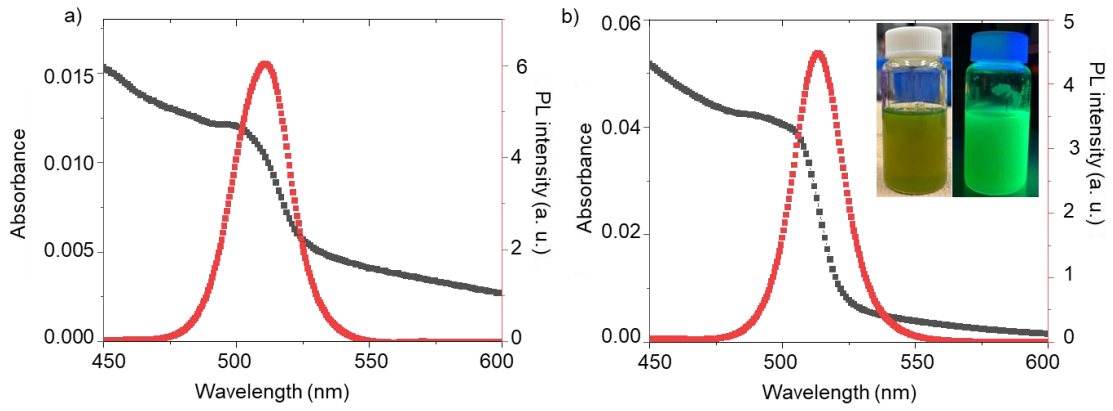

Figure 5.4. Absorption (black) and PL (red) spectra of conjugates synthesized by post-mixing (a) and in-situ (b) procedure. Inset: Images of the in-situ synthesized conjugates under the room light and 365 nm UV light.

I also measured the PL lifetime of post-mixing and in situ synthesized conjugate films at several positions (Figures 5.5a) using a picosecond (ps) time-resolved photoluminescence (TRPL) measurement system. The average PL lifetime is 4±1.8 ns and 5.66±1.7 ns for post-mixing and in situ synthesized conjugate respectively. An intimate interface formation has led to the possibility of carrier transfer at the interface of the conjugates. Therefore, to compare the conjugate's PL lifetime with the PNC-only sample, I measured the single PNC dot and PNC film PL lifetime (Figure 5.5a). These measurements can provide deeper insights into the conjugate system's exciton and carrier recombination dynamics. The single PNC dots (Figure

5.5b) are prepared by the drop and drag of the dilute $CsPbBr_3$ PNCs in toluene on the glass cover slip. The single PNC dot distribution was confirmed by observing the sample through an EMCCD camera. Conjugates and film samples are prepared by drop casting the PNC-MWCNT and concentrated PNC on the glass cover slip respectively. The film (11.66±1.6 ns) has the longest lifetime because of the long-range diffusion of free carriers. In the PNC film, carriers can move freely across interconnected nanocrystals or grains, reducing the likelihood of non-radiative recombination and extending the lifetime. The PL lifetime of the single PNC (3.86±0.78 ns) is reduced compared to the film due to carrier confinement. The confinement restricts carrier mobility and increases the probability of radiative or non-radiative recombination within the PNC, thus reducing the lifetime.

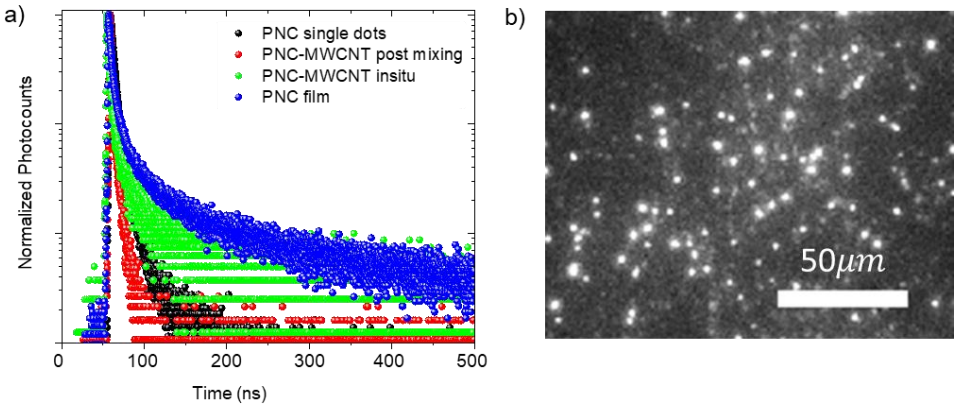

Figure 5.5. (a) PL decay curves for the PNC single dot, PNC film, and PNC-MWCNT conjugates prepared via post-mixing and in situ hot injection methods. (b) EMCCD image showing the single-particle distribution of the $CsPbBr_3$ PNCs.

As shown in the STEM image (Figure 5.3a), the conjugate prepared by post-mixing has separate single PNC dots on the MWCNT surface. Therefore, it is comparable to the PNC-single dots in Figure 5.5b. Similarly, in situ prepared conjugate is comparable to the PNC film because of the PNC multilayer formation on the MWCNT. Therefore, the decrease in the PL lifetime of the post-mixing and in situ prepared conjugates compared to the PNC-single dot and PNC film respectively, indicates the possibility of interfacial energy or carrier transfer in the conjugates system.

5.2.4 Chanrge carrier dynamics at the MWCNT-PNC interface

To further analyze whether this PL lifetime change is due to charge transfer or energy transfer, and to gain a detailed understanding of the excited-state carrier dynamics, I performed TA spectroscopy measurements on PNC-only sample and PNC-MWCNT conjugate. Since in-situ

hot injection synthesis gives more attachment of PNCs to MWCNTs compared to the post-mixing synthesis method, I chose this sample for TA measurement. Dried samples are used for this measurement. The TA was carried out by exiting the sample using a 400 nm (3.1 eV) femtosecond (fs) laser pulse, and a white light continuum monitored the photoexcited charge carrier kinetics.

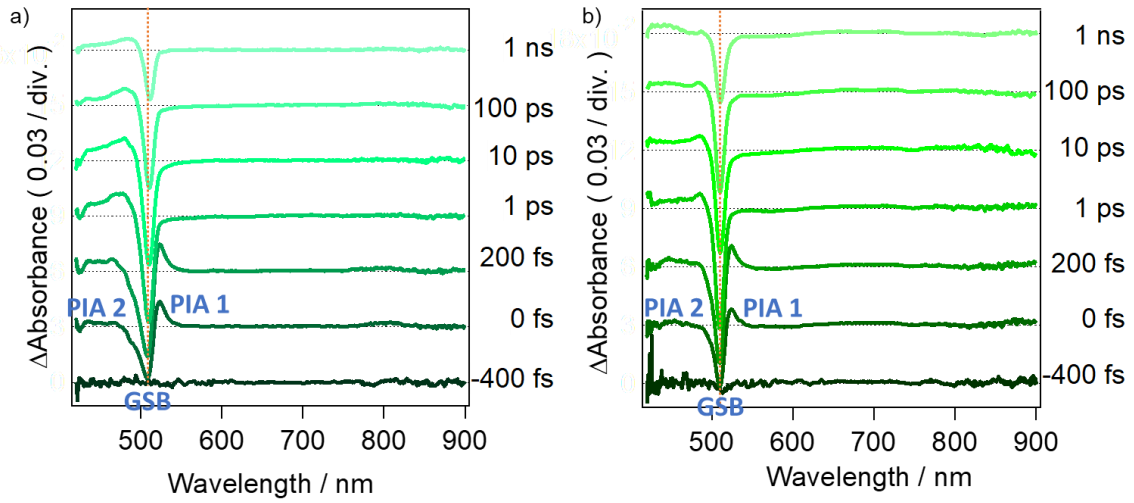

Figure 5.6. Transient absorption spectra of $CsPbBr_3$ PNC-only sample (a), and PNC-MWCNT conjugates (b) prepared by the in-situ hot injection method.

The TA spectra of the PNC-only and PNC-MWCNT are presented in Figure 5.6a and 5.6b, respectively. Three characteristic peaks appeared in the TA spectra. A negative ground-state bleach (GSB) peak at 510 nm appears because of the depletion of the ground-state electrons and a state-filling effect.[47] A lower energy short-lived photoinduced absorption (PAI 1) peak at around 530 nm appears due to the bandgap renormalization. This originated because of the relaxation of HCs. They populate lower-energy states near the band edges, which are now renormalized (shifted to lower energies).[48] Finally, a higher energy long-lived photoinduced absorption (PIA 2) peak appears due to the excitons re-excitation from the band edge to high energy states, which led to the formation of HCs.[21] The contribution of stimulated emission to the GSB peak cannot be denied.[49] A slight redshift in the GSB (Figure 5.6a) of the PNC-only sample at longer time delays suggests a biexciton-mediated Stark effect.[50 51] This phenomenon occurs due to the interaction between excitons within the PNCs. When a biexciton state forms, the mutual Coulomb interactions between the two excitons introduce an additional electric field within the PNC, which alters the energy landscape. The biexciton binding energy is typically larger, which lowers the energy of the emission from this state, causing a red shift compared to the single exciton emission. There is no such red shift in the GSB peak of the

PNC-MWCNT (Figure 5.6b) conjugate. This absence can be attributed to HC transfer, which suppresses carrier relaxation at the band edge and prevents the formation of band-edge biexcitons. The GSB peak broadening (Figure 5.6a and 5.6b) of the PNC-only sample at a lower time delay in comparison with PNC-MWCNT also supports the biexciton formation.[52]

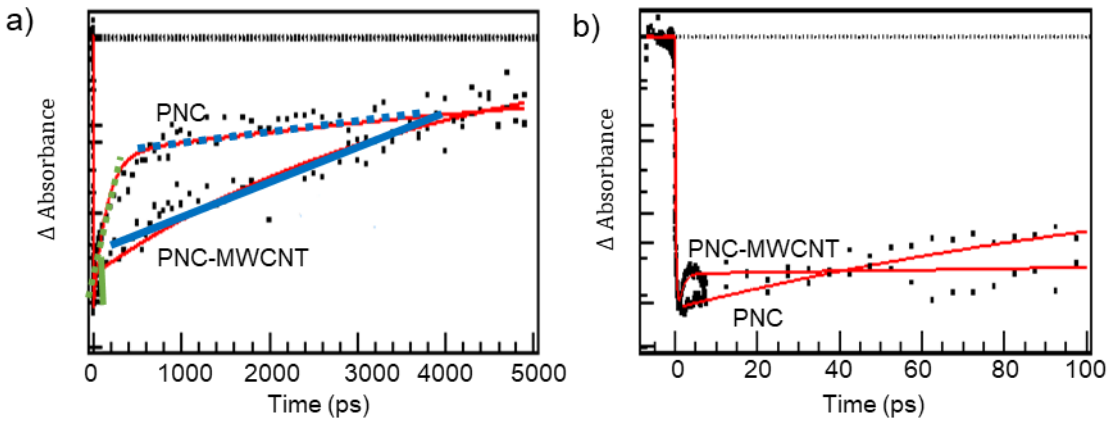

Figure 5.7. GSB recovery kinetics of $CsPbBr_3$ PNC-only sample and PNC-MWCNT conjugates (a). GSB recovery kinetics of samples at early time delays (b).

The time-dependent carrier dynamics for both samples were investigated by analyzing GSB recovery kinetics (Figure 5.7a). The bleach kinetics at 510 nm were fitted tri-exponentially. For the PNC-only sample, the calculated time constants are τ_1 = 250 fs (40%), τ_2 = 150 ps (34%), and τ_3 = 9.8 ns (26%). In contrast, for the PNC-MWCNT heterostructures, the time constants are τ_1 = 320 fs (38.5%), τ_2 = 1.0 ps (17.3%), and τ_3 = 3.7 ns (44.2%) (Table 5.1).

Table 5.1. Time constant of GSB recovery kinetics of PNC-only and PNC-MWCNT conjugate samples.

	τ_1	τ_2	τ_3
PNC-only	250 fs (40%)	150 ps (34%)	9.8 ns (26%)
PNC-MWCNT conjugates	320 fs (38.5%)	1.0 ps (17.3%)	3.7 ns (44.2%)

Since the sample was excited with energy higher than the bandgap, HC production is expected. Therefore, τ_1 is assigned for HCs relaxation to the band edge, which is responsible for the decay of short-lived low energy PIA1.[49] The presence of MWCNT decreases the hot electron-phonon coupling and increases the HC lifetime. The slow cooling of the HC in the case of conjugate favors the HC transfer,[53] because rapid carrier relaxation results in less availability of HCs at higher energy states. Therefore, within 320 fs the HCs are transferred

from the PNC to MWCNT. Biexciton formation at the band edge is confirmed from the TA spectra of the PNC-only sample. The biexcitons in PNCs can decay through multiple pathways. These include the generation of positive and negative trions, single exciton emission, and bright biexciton emission (Figure 5.8).

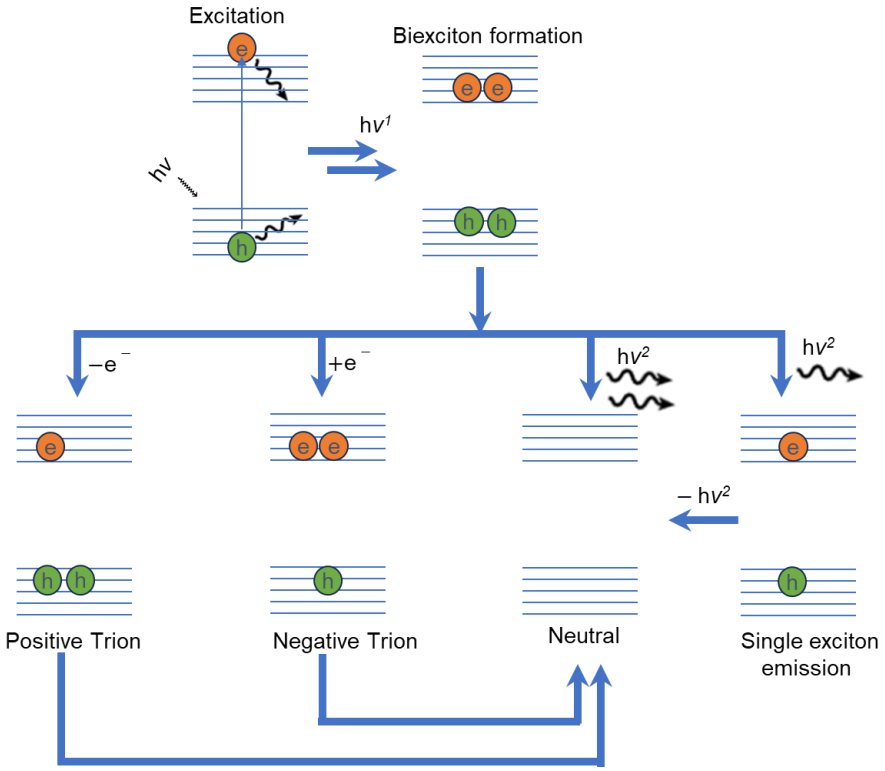

Figure 5.8. Possible events occurring after photoexcitation of the PNC-only sample are as follows: Upon excitation, HCs are generated. After that, multiple charge carriers relax to the band edge. From this state, they can return to a neutral state through several processes, including the formation of positive and negative trions, bright biexciton emission, and single exciton emission.

The τ_2 (green in Figure 5.7a) corresponds to non-radiative recombination processes.[54] In our PNC-only sample biexciton mediated nonradiative recombinations mainly contribute to the τ2. Under high pump fluence (increased carrier density in the excited state) and in a strongly confined system (7.12 nm), the charged particles' columbic interactions increase, opening a new decay pathway AR.[55] [56] It is well known that the time needed for the Auger process in the case of $CsPbBr_3$ PNC is several 10s to 100 picoseconds,[57] [55] which is comparable with the value 150 ps, guiding me to assign τ_2 as biexciton-mediated Auger process in case of PNC-only sample[58]. In contrast, the 150 ps component is absent in the PNC-MWCNT sample, indicating that the Auger process is suppressed in the conjugates due to HC transfer, which

further prevents biexciton formation at the band edge. Therefore, I can conclude that the Auger process is predominantly active in the PNC-only sample, not in the PNC-MWCNT conjugates.

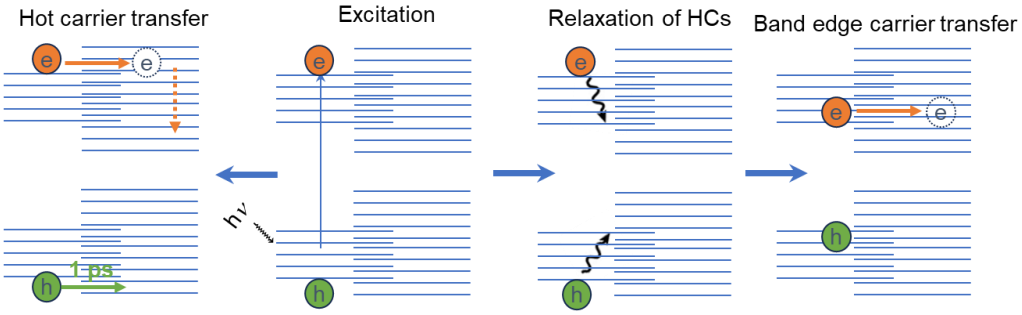

Figure 5.9. Possible event happening after photoexcitation of PNC -MWCNT sample. Upon excitation, a fraction of hot electrons transfers to the MWCNT, while others relax to the band edge. The band-edge electrons are subsequently transferred to the MWCNT. Meanwhile, a portion of the hot holes left behind is neutralized by electrons from the MWCNT.

The reason is that in conjugates, HCs are transferred from the PNC to MWCNT before relaxing to the band edge and initiating the Auger process. Anyway, the τ_2 value for the conjugates is significantly lower (1 ps) compared to the PNC-only sample, and its contribution is halved (Table 5.1). This rapid recovery indicates that a small fraction of the depleted electrons quickly return to the ground state of the PNC. This quick recovery may be due to the hot hole transfer from PNC to the MWCNT. The generation of a hot electron leaves behind a hot hole (high energy hole). Due to the hot hole's strong tendency to recombine with an electron, it can drive non-equilibrium dynamics at the interface, which makes it possible to transfer from PNC to MWCNT (Figure 5.9). Consequently, electrons from MWCNT come to the PNC. The contribution of this quick recovery is very small because it depends on the concentration and affinity of the hot hole. The hot hole interaction with lattice phonon and relaxation to the band edge is responsible for hampering this quick recovery process. Maity *et al.* reported a similar phenomenon that the fastest recovery (1.25 ps) at an early time scale is for hole transfer.[22] Actually, this type of hot hole neutralization could happen with or without hot electron transfer. Therefore, the 1ps component (hot hole quenching) in the case of the conjugates can be contributed by both processes.

The longest lifetime (τ_3) can be attributed to radiative or non-radiative band edge recombination in the case of only PNC-sample, and non-radiative back electron transfer for the conjugates. [59] [60] In Figure 5.7a (blue), it is observed that the rate of recovery in the presence of MWCNT is quick (3.7 ns), compared to PNC-only (9.8 ns). Therefore, there is a chance of

band edge electron or energy transfer for the conjugates. However, most of the reported data suggested the electron transfer between the perovskite and CNT.[61 62] The average recovery time decrease in the case of conjugates demonstrates the alternative way (via MWCNT) overall accelerates the ground state recovery of PNCs, which is similar to some of the reports, where a carrier transfer helps quick recovery.[22, 59, 63] In contrast, Nagal *et al.* reported a delayed recovery of bleach at the interface between perovskite and graphitic carbon nitride nanosheet. This is due to the large nanosheet provides weak confinement and suppresses AR, consequently delaying the back electron transfer.[54] In our conjugate system, although the MWCNT is large enough, the band gap is considerably negligible because of the multiple layers of the nanotube, which increase the density of states. It acts as a conductor where electrons can freely move. Direct electron transfer from MWCNT to PNC could be responsible for decreasing τ_3 and ultimately the overall recovery time.

5.3. Conclusions

HPs exhibit promising optoelectronic properties that are ideal for advanced optoelectronic applications. However, the efficiency of perovskite-based devices is constrained by challenges such as carrier radiative recombination and nonradiative losses. Integrating CNTs with HPs has emerged as an effective strategy to improve performance by reducing recombination losses, particularly through enhanced charge extraction. In this study, I successfully functionalized the MWCNT surface with phenylamine and prepared PNC-MWCNT conjugates following post-mixing of the $CsPbBr_3$ PNCs and functionalized MWCNT, or in situ hot injection methods where functionalized MWCNT was used as a ligand. The strong interaction between PNC and MWCNT facilitates charge transfer from the PNC to the MWCNT. The MWCNTs contribute to the suppression of HC relaxation and reduce non-radiative AR, leading to enhanced charge transfer at the PNC-MWCNT interface. Conjugates also reduce radiative recombination at the band edge. These findings emphasize the potential of PNC-MWCNT conjugates to improve the carrier dynamics in optoelectronic devices and offer a pathway to develop high-performance, stable perovskite-based systems. These conjugates show potential for the development of highly efficient PSCs.

References

(1) Dong, H.; Ran, C.; Gao, W.; Li, M.; Xia, Y.; Huang, W. Metal halide perovskite for next-generation optoelectronics: progresses and prospects. *ELight* **2023**, *3* (1), 3.

(2) Goel, P.; Sundriyal, S.; Shrivastav, V.; Mishra, S.; Dubal, D. P.; Kim, K.-H.; Deep, A. Perovskite materials as superior and powerful platforms for energy conversion and storage applications. *Nano Energy* **2021**, *80*, 105552.

(3) Sun, J.; Wu, J.; Tong, X.; Lin, F.; Wang, Y.; Wang, Z. M. Organic/inorganic metal halide perovskite optoelectronic devices beyond solar cells. *Advanced Science* **2018**, *5* (5), 1700780.

(4) Ju, D.; Dang, Y.; Zhu, Z.; Liu, H.; Chueh, C.-C.; Li, X.; Wang, L.; Hu, X.; Jen, A. K.-Y.; Tao, X. Tunable band gap and long carrier recombination lifetime of stable mixed $CH_3NH_3Pb_xSn_{1-x}Br_3$ Single Crystals. *Chemistry of Materials* **2018**, *30* (5), 1556-1565.

(5) Wang, Y.; Zhang, Y.; Zhang, P.; Zhang, W. High intrinsic carrier mobility and photon absorption in the perovskite $CH_3NH_3PbI_3$. *Physical Chemistry Chemical Physics* **2015**, *17* (17), 11516-11520.

(6) Zhou, D.; Zhou, T.; Tian, Y.; Zhu, X.; Tu, Y. Perovskite-based solar cells: materials, methods, and future perspectives. *Journal of Nanomaterials* **2018**, *2018* (1), 8148072.

(7) Cheng, J.; Cao, H.; Zhang, S.; Yue, F.; Zhou, Z. Reinforcing built-in electric field to enable efficient carrier extraction for high-performance perovskite solar cells. *Materials Chemistry Frontiers* **2024**.

(8) Li, Y.; Luo, X.; Ding, T.; Lu, X.; Wu, K. Size-and halide-dependent Auger recombination in lead halide perovskite nanocrystals. *Angewandte Chemie* **2020**, *132* (34), 14398-14401.

(9) Luo, D.; Su, R.; Zhang, W.; Gong, Q.; Zhu, R. Minimizing non-radiative recombination losses in perovskite solar cells. *Nature Reviews Materials* **2020**, *5* (1), 44-60.

(10) Bu, T.; Li, J.; Huang, W.; Mao, W.; Zheng, F.; Bi, P.; Hao, X.; Zhong, J.; Cheng, Y.-B.; Huang, F. Surface modification via self-assembling large cations for improved performance and modulated hysteresis of perovskite solar cells. *Journal of Materials Chemistry A* **2019**, *7* (12), 6793-6800.

(11) Ma, K.; Atapattu, H. R.; Zhao, Q.; Gao, Y.; Finkenauer, B. P.; Wang, K.; Chen, K.; Park, S. M.; Coffey, A. H.; Zhu, C. Multifunctional conjugated ligand engineering for stable and efficient perovskite solar cells. *Advanced Materials* **2021**, *33* (32), 2100791.

(12) Begum, R.; Parida, M. R.; Abdelhady, A. L.; Murali, B.; Alyami, N. M.; Ahmed, G. H.; Hedhili, M. N.; Bakr, O. M.; Mohammed, O. F. Engineering interfacial charge transfer in $CsPbBr_3$ perovskite nanocrystals by heterovalent doping. *Journal of the American Chemical Society* **2017**, *139* (2), 731-737.

(13) Kahmann, S.; Loi, M. A. Hot carrier solar cells and the potential of perovskites for breaking the Shockley–Queisser limit. *Journal of Materials Chemistry C* **2019**, *7* (9), 2471-2486.

(14) Wang, K.; Zheng, L.; Hou, Y.; Nozariasbmarz, A.; Poudel, B.; Yoon, J.; Ye, T.; Yang, D.; Pogrebnyakov, A. V.; Gopalan, V. Overcoming Shockley-Queisser limit using halide perovskite platform? *Joule* **2022**, *6* (4), 756-771.

(15) Ahmed, I.; Shi, L.; Pasanen, H.; Vivo, P.; Maity, P.; Hatamvand, M.; Zhan, Y. There is plenty of room at the top: generation of hot charge carriers and their applications in perovskite and other semiconductor-based optoelectronic devices. *Light: Science & Applications* **2021**, *10* (1), 174.

(16) Righetto, M.; Lim, S. S.; Giovanni, D.; Lim, J. W. M.; Zhang, Q.; Ramesh, S.; Tay, Y. K. E.; Sum, T. C. Hot carriers perspective on the nature of traps in perovskites. *Nature Communications* **2020**, *11* (1), 2712.

(17) Zhou, M.; Sarmiento, J. S.; Fei, C.; Wang, H. Charge transfer and diffusion at the perovskite/PCBM interface probed by transient absorption and reflection. *The Journal of Physical Chemistry C* **2019**, *123* (36), 22095-22103.

(18) Guan, Z.; Li, Y.; Man, P.; Tan, H.; Wei, Q.; Liu, J.; Li, M.; Ly, T. H.; Yin, J.; Lee, C. S. Ultrafast electron-transfer via hybrid states at perovskite/fullerene interface. *Advanced Materials* **2024**, 2407406.

(19) Sachith, B. M.; Zhang, Z.; Subramanyam, P.; Subrahmanyam, C.; Furube, A.; Tamai, N.; Okamoto, T.; Misawa, H.; Biju, V. Photoinduced interfacial electron transfer from perovskite quantum dots to molecular acceptors for solar cells. *Nanoscale* **2023**, *15* (17), 7695-7702.

(20) Nair, V. C.; Muthu, C.; Rogach, A. L.; Kohara, R.; Biju, V. Channeling exciton migration into electron transfer in formamidinium lead bromide perovskite nanocrystal/fullerene composites. *Angewandte Chemie* **2017**, *129* (5), 1234-1238.

(21) Nagal, V.; Kumar, V.; Rahman, S.; Kumar, K.; Singh, K.; Kumar, M.; Ahmad, R.; Hafiz, A. K. Insight into hot carrier kinetics of $CsPbBr_3$/ZnO heterostructures for photodetector application. *ACS Applied Optical Materials* **2023**, *1* (3), 779-787.

(22) Maity, P.; Dana, J.; Ghosh, H. N. Multiple charge transfer dynamics in colloidal $CsPbBr_3$ perovskite quantum dots sensitized molecular adsorbate. *The Journal of Physical Chemistry C* **2016**, *120* (32), 18348-18354.

(23) Jiménez-López, J. s.; Puscher, B. M.; Guldi, D. M.; Palomares, E. Improved carrier collection and hot electron extraction across perovskite, C_{60}, and TiO_2 interfaces. *Journal of the American Chemical Society* **2019**, *142* (3), 1236-1246.

(24) Cheng, N.; Liu, P.; Qi, F.; Xiao, Y.; Yu, W.; Yu, Z.; Liu, W.; Guo, S.-S.; Zhao, X.-Z. Multi-walled carbon nanotubes act as charge transport channel to boost the efficiency of hole transport material free perovskite solar cells. *Journal of Power Sources* **2016**, *332*, 24-29.

(25) Li, D.; He, L.; Pang, Z.; Wang, F.; Fan, L.; Liu, X.; Wei, M.; Yang, L. Anchoring grain boundary via aminated carbon nanotubes to achieve efficient and stable perovskite solar cells. *Solar RRL* **2022**, *6* (10), 2200297.

(26) Lin, D.; Ma, L.; Ni, W.; Wang, C.; Zhang, F.; Dong, H.; Gurzadyan, G. G.; Nie, Z. Unveiling hot carrier relaxation and carrier transport mechanisms in quasi-two-dimensional layered perovskites. *Journal of Materials Chemistry A* **2020**, *8* (47), 25402-25410.

(27) Nadinov, I.; Almasabi, K.; Gutiérrez-Arzaluz, L.; Thomas, S.; Hasanov, B. E.; Bakr, O. M.; Alshareef, H. N.; Mohammed, O. F. Real-time tracking of hot carrier injection at the interface of $FAPbBr_3$ perovskite using femtosecond mid-IR spectroscopy. *ACS Central Science* **2023**, *10* (1), 43-53.

(28) Feng, W.; Tan, Y.; Yang, M.; Jiang, Y.; Lei, B.-X.; Wang, L.; Wu, W.-Q. Small amines bring big benefits to perovskite-based solar cells and light-emitting diodes. *Chem* **2022**, *8* (2), 351-383.

(29) Moraitis, G.; Špitalský, Z.; Ravani, F.; Siokou, A.; Galiotis, C. Electrochemical oxidation of multi-wall carbon nanotubes. *Carbon* **2011**, *49* (8), 2702-2708.

(30) Estrade-Szwarckopf, H. XPS photoemission in carbonaceous materials: A "defect" peak beside the graphitic asymmetric peak. *Carbon* **2004**, *42* (8-9), 1713-1721.

(31) Varga, M.; Izak, T.; Vretenar, V.; Kozak, H.; Holovsky, J.; Artemenko, A.; Hulman, M.; Skakalova, V.; Lee, D. S.; Kromka, A. Diamond/carbon nanotube composites: Raman, FTIR and XPS spectroscopic studies. *Carbon* **2017**, *111*, 54-61.

(32) Duc Chinh, V.; Speranza, G.; Migliaresi, C.; Van Chuc, N.; Minh Tan, V.; Phuong, N.-T. Synthesis of gold nanoparticles decorated with multiwalled carbon nanotubes (Au-MWCNTs) via cysteaminium chloride functionalization. *Scientific Reports* **2019**, *9* (1), 5667.

(33) Ramanathan, T.; Fisher, F.; Ruoff, R.; Brinson, L. C. Amino-functionalized carbon nanotubes for binding to polymers and biological systems. *Chemistry of Materials* **2005**, *17* (6), 1290-1295.

(34) Wepasnick, K. A.; Smith, B. A.; Bitter, J. L.; Howard Fairbrother, D. Chemical and structural characterization of carbon nanotube surfaces. *Analytical and Bioanalytical Chemistry* **2010**, *396*, 1003-1014.

(35) Botti, S.; Rufoloni, A.; Rindzevicius, T.; Schmidt, M. S. Surface-enhanced Raman spectroscopy characterization of pristine and functionalized carbon nanotubes and graphene. *Raman Spectroscopy* **2018**, *203*.

(36) Ying, Y.; Saini, R. K.; Liang, F.; Sadana, A. K.; Billups, W. Functionalization of carbon nanotubes by free radicals. *Organic Letters* **2003**, *5* (9), 1471-1473.

(37) Azri, F. A.; Sukor, R.; Hajian, R.; Yusof, N. A.; Bakar, F. A.; Selamat, J. Modification strategy of screen-printed carbon electrode with functionalized multi-walled carbon nanotube and chitosan matrix for biosensor development. *Asian Journal of Chemistry* **2017**, *29* (1), 31.

(38) Chen, S.; Ren, D.; Li, B.; Li, K.; Chen, L.; Xu, M.; Liu, X. Benzoxazine containing fluorinated aromatic ether nitrile linkage: preparation, curing kinetics and dielectric properties. *Polymers* **2019**, *11* (6), 1036.

(39) Wang, L.; Qi, T.; Hu, M.; Zhang, S.; Xu, P.; Qi, D.; Wu, S.; Xiao, H. Inhibiting mercury re-emission and enhancing magnesia recovery by cobalt-loaded carbon nanotubes in a novel magnesia desulfurization process. *Environmental Science & Technology* **2017**, *51* (19), 11346-11353.

(40) Dehghani, M. H.; Taher, M. M.; Bajpai, A. K.; Heibati, B.; Tyagi, I.; Asif, M.; Agarwal, S.; Gupta, V. K. Removal of noxious Cr(VI) ions using single-walled carbon nanotubes and multi-walled carbon nanotubes. *Chemical Engineering Journal* **2015**, *279*, 344-352.

(41) Okamoto, T.; Biju, V. Slipping-free halide perovskite supercrystals from supramolecularly-assembled nanocrystals. *Small* **2023**, *19* (32), 2303496.

(42) Li, Y.; Cai, M.; Shen, M.; Cai, Y.; Xie, R.-J. Bidentate aliphatic quaternary ammonium ligand-stabilized $CsPbBr_3$ perovskite nanocrystals with high PLQY (92.3%) and superior stability. *Journal of Materials Chemistry C* **2022**, *10* (21), 8356-8363.

(43) Yan, N.; Yin, H.; Wang, Z.; Yuan, H.; Xin, Y.; Tang, Y. Role of ammonium derivative ligands on optical properties of $CH_3NH_3PbBr_3$ perovskite nanocrystals. *Langmuir* **2019**, *35* (47), 15151-15157.

(44) Kazes, M.; Udayabhaskararao, T.; Dey, S.; Oron, D. Effect of surface ligands in perovskite nanocrystals: extending in and reaching out. *Accounts of Chemical Research* **2021**, *54* (6), 1409-1418.

(45) Lee, J.; Lee, H.; Kim, C.; Nguyen, T. T. T.; Kim, Y.; Jeong, G.; Chang, M.; Yun, C.; Yoon, H. Controlled growth of perovskite nanocrystals on nanotubes via a nanoseeding intermediate stage: toward novel optoelectronic applications. *The Journal of Physical Chemistry Letters* **2023**, *14* (39), 8837-8845.

(46) Jana, A.; Meena, A.; Patil, S. A.; Jo, Y.; Cho, S.; Park, Y.; Sree, V. G.; Kim, H.; Im, H.; Taylor, R. A. Self-assembly of perovskite nanocrystals. *Progress in Materials Science* **2022**, *129*, 100975.

(47) Samanta, S.; Babu, K. J.; Shukla, A.; Kaur, G.; Kaur, A.; Ghosh, H. N. Unveiling the ultrafast electron transfer dynamics in epitaxial dodecahedron $CsPbBr_3$/Au heterostructure. *ChemPhotoChem* **2024**, *8* (4), e202300242.

(48) Price, M. B.; Butkus, J.; Jellicoe, T. C.; Sadhanala, A.; Briane, A.; Halpert, J. E.; Broch, K.; Hodgkiss, J. M.; Friend, R. H.; Deschler, F. Hot-carrier cooling and photoinduced refractive index changes in organic–inorganic lead halide perovskites. *Nature Communications* **2015**, *6* (1), 8420.

(49) Du, L.; An, J.; Katayama, T.; Duan, M.; Shi, X.; Wang, Y.; Furube, A. Photogenerated carrier dynamics of Mn^{2+} doped $CsPbBr_3$ assembled with TiO_2 systems: Effect of Mn doping content. *The Journal of Chemical Physics* **2024**, *160* (16).

(50) Shen, X.; Wang, S.; Geng, C.; Li, L.; Zhao, E.; Sun, J.; Wu, W.; An, L.; Pan, K. Red shift of bleaching signals in femtosecond transient absorption spectra of $CsPbX_3$ (X= Cl/Br, Br, Br/I) nanocrystals induced by the biexciton effect. *The Journal of Physical Chemistry C* **2021**, *125* (9), 5278-5287.

(51) Aneesh, J.; Swarnkar, A.; Kumar Ravi, V.; Sharma, R.; Nag, A.; Adarsh, K. Ultrafast exciton dynamics in colloidal $CsPbBr_3$ perovskite nanocrystals: Biexciton effect and Auger recombination. *The Journal of Physical Chemistry C* **2017**, *121* (8), 4734-4739.

(52) Ashner, M. N.; Shulenberger, K. E.; Krieg, F.; Powers, E. R.; Kovalenko, M. V.; Bawendi, M. G.; Tisdale, W. A. Size-dependent biexciton spectrum in $CsPbBr_3$ perovskite nanocrystals. *ACS Energy Letters* **2019**, *4* (11), 2639-2645.

(53) Li, M.; Fu, J.; Xu, Q.; Sum, T. C. Slow hot-carrier cooling in halide perovskites: prospects for hot-carrier solar cells. *Advanced Materials* **2019**, *31* (47), 1802486.

(54) Nagal, V.; Kumar, V.; Jain, M.; Saini, S. K.; Kumar, M.; Singh, K.; Bhattacharya, S.; Ahmad, R.; Hafiz, A. K. Slow cooling and transfer dynamics of hot excitons in $CsPbBr_3$ perovskite quantum dots/g-CN nanosheet heterostructures: Implications for optoelectronic applications. *ACS Applied Nano Materials* **2023**, *6* (10), 8894-8906.

(55) Klimov, V. I. Spectral and dynamical properties of multiexcitons in semiconductor nanocrystals. *Annual Review of Physical Chemistry* **2007**, *58* (1), 635-673.

(56) Oriel, E. H.; Dirin, D. N.; Shcherbak, K.; Bodnarchuk, M. I.; Kovalenko, M. V.; Chen, L. X.; Schaller, R. D. Intraband cooling and auger recombination in weakly to strongly quantum-

confined $CsPbBr_3$ perovskite nanocrystals. *The Journal of Physical Chemistry Letters* **2024**, *15*, 6062-6068.

(57) Kaniyankandy, S. Evidence of auger heating in hot carrier cooling of $CsPbBr_3$ nanocrystals. *Colloids and Surfaces A: Physicochemical and Engineering Aspects* **2022**, *635*, 128025.

(58) Cui, M.; Qin, C.; Jiang, Y.; Yuan, M.; Xu, L.; Song, D.; Jiang, Y.; Liu, Y. Direct observation of competition between amplified spontaneous emission and Auger recombination in quasi-two-dimensional perovskites. *The Journal of Physical Chemistry Letters* **2020**, *11* (14), 5734-5740.

(59) Roy, S.; Mahato, M. K.; Prasad, E. Electronic effect of substituents on the charge-transfer dynamics at the $CsPbBr_3$ perovskite–small molecule interface. *Physical Chemistry Chemical Physics* **2023**, *25* (5), 4121-4131.

(60) Tvrdy, K.; Frantsuzov, P. A.; Kamat, P. V. Photoinduced electron transfer from semiconductor quantum dots to metal oxide nanoparticles. *Proceedings of the National Academy of Sciences* **2011**, *108* (1), 29-34.

(61) Schulz, P.; Dowgiallo, A.-M.; Yang, M.; Zhu, K.; Blackburn, J. L.; Berry, J. J. Charge transfer dynamics between carbon nanotubes and hybrid organic metal halide perovskite films. *The Journal of Physical Chemistry Letters* **2016**, *7* (3), 418-425.

(62) Bansal, P.; Zhang, X.; Wang, H.; Kar, P.; William, W. Y. Charge transfer between lead halide perovskite nanocrystals and single-walled carbon nanotubes. *Nanoscale Advances* **2020**, *2* (2), 808-813.

(63) Chakkamalayath, J.; Hartland, G. V.; Kamat, P. V. Light induced processes in $CsPbBr_3$–Au hybrid nanocrystals: Electron transfer and expulsion of Au. *The Journal of Physical Chemistry C* **2021**, *125* (32), 17881-17889.

General conclusions

In conclusion, this thesis has comprehensively investigated the mechanisms of exciton migration, recombination, and transfer in LHPs. HPs are recognized for their excellent optoelectronic properties, making them strong candidates for advanced applications in modern technology, including solar cells, LEDs, and lasers. However, the efficiency of devices based on these materials is significantly constrained by challenges such as radiative and nonradiative carrier recombination. In solar cells, for instance, nonradiative losses and radiative recombination at interfaces impede efficient carrier extraction, limiting overall device performance. Conversely, in LEDs and lasers, nonradiative recombination competes with radiative recombination, reducing luminescence efficiency and impairing performance. Nonradiative recombination is typically linked to defects in the HP crystal lattice. On the other hand, radiative recombination in solar cells stems from high exciton binding energy, limited carrier diffusion length, and inefficient interfacial transfer. Although bulk perovskite increases carrier diffusion length, the carriers have to diffuse a long path to reach the carrier transport layer, consequently increasing the chance of radiative and nonradiative recombination loss. To effectively address these issues, this thesis focuses on the preparation of defect-free PNCs to decrease nonradiative recombination, assembled PNC thin films to increase carrier diffusion length, and facilitating rapid carrier extraction at the interface by incorporating an acceptor molecule.

In Chapter 3, I investigated the defect passivation in $CsPbBr_3$ PNCs, with a focus on mitigating halide vacancies that contribute to nonradiative recombination and low PLQY. To address these defects, I tested various bromide salts, including CsBr, NaBr, and KBr, at an aqueous-organic interface. Among these, NaBr exhibited the most significant improvement, increasing the PLQY from 57% to 98%. STEM-EDX analysis revealed an increase in the bromide ratio from 2.64 to 2.98, approaching the ideal stoichiometric ratio for bromide in $CsPbBr_3$. This result highlights an effective strategy for enhancing material stability and optoelectronic performance. Additionally, the extended PL lifetime following halide vacancy passivation indicates a reduction in nonradiative recombination pathways. This defect management approach also suppresses single-particle blinking, indicating the reduced trap states and minimized nonradiative decay pathways.

In Chapter 4, I focused on the assembly formation of $FAPbBr_3$ PQDs assemblies within a polymer matrix to increase the carrier diffusion length. Polybutadiene was used as polymer

which helps to self-assemble PQDs due to solvent evaporation and polymer shrinkage during drying. When the individual PQDs come closer in the assembly their electronic wave function overlaps and a miniband is formed. This assembly formation extends exciton lifetimes by reducing quantum confinement and enhancing dielectric screening. In this chapter, I also investigated how external temperature modulates these assemblies as well as their optoelectronic properties. Polymer expansion at elevated temperatures disrupts the assemblies and increases the inter-QDs distance which is responsible for the blue shifts in PL spectra and decreased exciton lifetimes. Cooling of the assembly at room temperature partially recovers the optoelectronic properties as well as the assemblies.

In Chapter 5, I demonstrated quick carrier extraction from $CsPbBr_3$ PNCs to MWCNT. I functionalized MWCNTs with phenylamine to create PNC-MWCNT conjugates. The PNC can bind with the $-NH_2$ group of the functionalized MWCNT. Post-mixing and in-situ hot injection were used to prepare the conjugates. The strong interaction between PNCs and MWCNTs fosters efficient charge transfer from the PNCs to the MWCNTs. This is proved by the TRPL and TA spectroscopy measurements. The decrease in PL lifetime in conjugates compared to the PNC-only sample indicates the carrier or energy transfer at the interface. TA result reveals a reduction in nonradiative Auger recombination in conjugates indicating the hot electron transfer from PNC to MWCNT. Decreased band-edge radiative or nonradiative recombination in conjugates also indicates the band-edge carrier or energy transfer. These results suggest that MWCNT-decorated with PNCs hold significant promise for advancing the performance of perovskite-based devices.

Overall, the improved quality of PNCs, a controlled carrier diffusion length, and enhanced hot carrier extraction at the interface offer significant potential for advancing LHP-based device performance.

List of publications

1. **Most Farida Khatun,** Takuya Okamoto, Vasudevanpillai Biju**,** "Self-assembled halide perovskite quantum dots in polymer thin films showing temperature-controlled exciton recombination." *Chemical Communications* **2023**, 59 (93), 13831-13834.

2. Sushant Ghimire, **Most Farida Khatun**, Bhagyashree M. Sachith, Takuya Okamoto, Jeladhara Sobhanan, Ch Subrahmanyam, Vasudevanpillai Biju, "Highly Luminescent and Stable Halide Perovskite Nanocrystals by Interfacial Defect Passivation and Amphiphilic Ligand Capping." *ACS Applied Materials & Interfaces* **2023**, 15 (34), 41081-41091.

List of papers presented at conferences

1. Most Farida Khatun, Takuya Okamoto, Vasudevanpillai Biju, "Defect Passivation and Halide Exchange in Hydrophilic and Amphiphilic Ligands-Capped Halide Perovskite Nanocrystals" 10th Hokkaido University Cross-Departmental Symposium, September 6th, 2024, Frate Hall, School of Medicine Centennial Hall, Hokkaido University (Poster).

2. Most Farida Khatun, Takuya Okamoto, Vasudevanpillai Biju, "Defect Passivation and Halide Exchange in Amphiphilic Ligand-Capped $CsPbBr_3$ Perovskite Nanocrystals" 24th RIES-HOKUDAI International Symposium, December 6th – December 7th, 2023, Akira Suzuki Hall, Hokkaido University, Sapporo, Japan (Poster).

3. Most Farida Khatun, Sushant Ghimire, Bhagyashree M. Sachith, Takuya Okamoto, Jeladhara Sobhanan, Ch Subrahmanyam, Vasudevanpillai Biju, "Interfacial defect passivation of amphiphilic ligand-capped halide perovskite nanocrystals, The 14th ISAJ Annual Symposium, November 10th, 2023, Conference Hall (5th floor), CRIS building, Hokkaido University Sapporo, Japan (Poster).

4. Most Farida Khatun, Takuya Okamoto, Vasudevanpillai Biju, "Heat-induced modulating the excitonic properties of halide perovskite assemblies using polymer microenvironments" The 31st International Conference on Photochemistry, July 23rd - July 28th, 2023, Sapporo Park Hotel, Sapporo, Japan (poster).

5. Most Farida Khatun, Vasudevanpillai Biju, Assembly-Assisted Carrier Relaxation in Formamidinium Lead Bromide Quantum Dots. Winter presentation meeting, Chemical Society of Japan, Hokkaido branch, January 24th -January 25th, 2023, Hokkaido University, Japan (Oral).

6. Most Farida Khatun, Takuya Okamoto, Vasudevan Pillai Biju, "Controlling Excitonic Recombination in Halide Perovskite Assemblies using Polymer Microenvironment", 23rd RIES-HOKUDAI International Symposium December 5th- December 6th, 2022, Suzuki Akira Hall Hokkaido University, Sapporo, Japan (Poster).